



Norwegian University of
Science and Technology

FIB/SEM Characterization of Paper Materials

Erik Dobloug Roede

Nanotechnology

Submission date: June 2016

Supervisor: Øyvind Weiby Gregersen, IKP

Co-supervisor: Vegar Ottesen, IKP

Norwegian University of Science and Technology
Department of Chemical Engineering

Abstract

3D microscopy is of interest for structural characterization of paper materials to study the use of cellulose nanofibrils as a paper additive. Focused ion beam (FIB) tomography is a promising microscopy technique for this application, combining scanning electron microscopy (SEM) with serial sectioning by ion beam, potentially with nanoscale resolution.

In this work, FIB tomography is demonstrated for paper samples, showing that the technique is applicable to this class of materials. Volume reconstructions with voxel resolution down to $13 \times 13 \times 15 \text{ nm}^3$ for volumes of up to approximately $10 \times 10 \times 2 \text{ }\mu\text{m}^3$ are obtained. The latter is limited by the acquisition time, and can therefore be extended.

A working protocol is developed, from sample preparation and image acquisition to processing and volume reconstruction. The method is discussed in comparison to established 3D methods for paper materials, and suggestions are made for improving the resolution and increasing the volume.

Sammendrag

3D-mikroskopi er en lovende metode for strukturkarakterisering av papirmaterialer for å undersøke bruk av cellulose-nanofibriller som tilsats. Fokusert ionestråle (FIB)-tomografi er en mikroskopiteknikk som virker lovende til dette formålet. Metoden kombinerer sveipelektronmikroskopi (SEM) og kutting av tverrsnitt med ionestråle, potensielt med oppløsning på nanoskala.

I denne rapporten blir FIB-tomografi utført for papirprøver som demonstrasjon på at teknikken kan anvendes for denne typen materialer. Volumrekonstruksjoner med vokseloppløsning ned til $13 \times 13 \times 15 \text{ nm}^3$ for volumer opp til omtrent $10 \times 10 \times 2 \text{ }\mu\text{m}^3$ er oppnådd. Volumet er begrenset av opptakstiden, og kan derfor utvides.

En fungerende metode er utviklet, fra prøvepreparering og mikroskopi til bildeprosessering og volumrekonstruksjon. Metoden diskuteres i forhold til anvendte 3D-metoder for papirmaterialer, og forbedringer foreslås for å oppnå bedre oppløsning og større volum.

Preface

This work is submitted in fulfillment of the requirements for the degree M.Sc. in Nanotechnology from NTNU. The work was performed at the Department of Chemical Engineering at NTNU with Professor Øyvind Weiby Gregersen as supervisor. Experiments were performed at NTNU NanoLab and laboratories of the Department of Chemical Engineering at NTNU.

Acknowledgments

I would first of all like to thank my supervisor, Professor Øyvind Weiby Gregersen for his guidance through this year. My sincerest gratitude goes to my co-supervisor Vegar Ottesen, for invaluable assistance and encouragement. I am further grateful to Jonathan Torstensen, Kristin Syverud and Muhammad Bilal Khan Niazi for their input and comments, as well as my fellow master student Henrik Riis for valuable discussions. I would also like to thank Per Olav Johnsen at PFI for sharing his expertise on electron microscopy and sample preparation.

Further, I thank the engineers and staff at NTNU NanoLab, for enabling me to use such a fascinating instrument. In particular, Ken Roger Ervik and Aleksander Mosberg for sharing their insight and experience with FIB. I would also like to thank Professor Pawel Sikorski at NTNU for his ideas on sample preparation. My gratitude also goes to Nan E. Tostrup Skogaker at St. Olav hospital for her help with sample preparation.

Contents

1	Introduction	3
2	Theory	5
2.1	Cellulose, Paper and CNF	5
2.1.1	Cellulose	5
2.1.2	Paper	5
2.1.3	Nanocellulose	6
2.2	Scanning Electron Microscopy	7
2.2.1	Electron Column	8
2.2.2	Electron-Sample Interactions	13
2.2.3	Detectors	16
2.2.4	Contrast Mechanisms	20
2.2.5	Sample Charging	21
2.2.6	Low Voltage SEM	24
2.3	FIB	24
2.3.1	Instrument	25
2.3.2	Ion Column	25
2.3.3	Ion-Sample Interactions	25
2.4	3D Methods	28
2.4.1	FIB Tomography	28
2.5	Monte Carlo Simulation	30
2.6	Image Processing	31
3	Materials and Methods	33
3.1	Monte Carlo Simulations	33
3.2	Instruments	33
3.3	Sample Preparation	35
3.3.1	Sample Preparation for FIB	35
3.4	FIB-SEM Experiments	36
3.4.1	Imaging Parameters	37
3.4.2	FIB Tomography	37
3.5	Image Processing	39
3.5.1	Preprocessing	39
3.5.2	Segmentation	39
3.5.3	Reconstruction	40

4	Results	41
4.1	Monte Carlo Simulations	41
4.2	Sample Preparation	45
4.3	FIB/SEM	49
4.3.1	FIB Tomography	57
5	Discussion	69
5.1	Monte Carlo Simulations	69
5.2	FIB/SEM	69
6	Conclusion	83
6.1	Further Work	84

1

Introduction

The purpose of this work is to find a suitable method for high resolution focused ion beam (FIB) tomography of paper materials in order to study the effect of cellulose nanofibrils (CNF) as a paper additive. This includes finding suitable sample preparation techniques, instrument parameters and post-processing routines.

New cellulose materials with nanoscale dimensions, nanocelluloses, with novel properties show promise for many and varied applications. In the 1983 paper reporting the discovery of CNF, Turbak *et al.* [64] suggest its use in foodstuffs, cosmetics, medicinal products and paper production. Among nanomaterials, nanocellulose is particularly interesting because it is made from abundant and renewable raw materials. It can be manufactured in bulk and is biodegradable. It therefore has potential for application on an industrial scale. CNF shows promise as a paper additive, though the precise interactions with other paper components are not known.

The development and use of any material require suitable characterization techniques. For the use of CNF in paper materials, three dimensional imaging is of interest because paper has a rich three-dimensional structure that is decisive for the material properties. 3D techniques have therefore been used to study paper materials, among them X-ray tomography and serial sectioning microscopy. These techniques have allowed characterization of the structure, but with resolution insufficient to see CNF. Serial sectioning techniques using transmission electron microscope (TEM) are possible with superior spatial resolution, but very limited analysis volume.

FIB tomography, *in-situ* serial sectioning with an ion beam and imaging with scanning electron microscope (SEM), is a 3D microscopy technique that may fill this niche. Since its development in 2004 [33], FIB tomography has become an established technique for materials science. The use of FIB for biology and biological materials is a more recent development that has received much attention [32].

While SEM is used for image acquisition, FIB tomography places stricter demands on the sample preparation and treatment than SEM alone. The sample must necessarily be imaged without a conductive coating, and must be stable for a long period of time. Establishing sample preparation protocols and imaging parameters are therefore investigated and discussed in some detail. Monte

Carlo simulations are performed to support the experimental work. Use of the method is discussed in comparison to other 3D microscopy techniques.

2

Theory

2.1 Cellulose, Paper and CNF

2.1.1 Cellulose

Cellulose is a biopolymer synthesized by a range of organisms. It consists of D-glucose monomers linked through $\beta(1-4)$ glucosidic bonds [47]. The degree of polymerization depends on the source [6], but is approximately 10^4 for natural cellulose [45]. The molecular structure is shown in Figure 1. Intra-chain hydrogen bonds between monomers give the molecule a linear ribbon shape [47]. The exposed hydroxyl groups makes cellulose a hydrophilic molecule, able to form inter-chain hydrogen bonds.

Cellulose fibers are the cell walls of plant cells. These are in turn made up of a hierarchy of smaller structures. Above the molecular level, the smallest unit is the elementary fibril, a linear arrangement of cellulose chains with a diameter of 3.5 nm [46]. Structurally, elementary fibrils are composed of both crystalline and amorphous regions. Elementary fibrils combine to form microfibrils, with diameters around 10-30 nm depending on the source [6, 40].

Together with lignin and hemicelluloses, cellulose microfibrils combine to form the anatomical structures of the plant cell wall.

2.1.2 Paper

A brief description of the structure, composition and production is given here. An overview can be found in [2].

Paper is a material composed primarily of interconnected cellulose fibers. It is made by dehydration of pulp, a suspension of fibers and fiber fragments (fines).

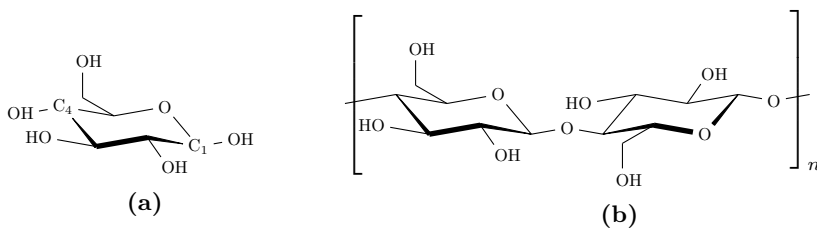


Figure 1: Molecular structure of a) D-glucose, b) repeating unit of cellulose.

As water is removed, interfiber hydrogen bonds are formed, forming a network of fibers.

Pulp is made by decomposing a lignocellulosic material (primarily wood) into fibers by mechanical and/or chemical processing. A range of processes exist, with different effects on the product and yield. In brief, mechanical pulping methods separate the wood fibers, but does not remove any components of the wood. Lignin is therefore still present in the pulp. Chemical pulping methods dissolve lignin.

The combination of ingredients is termed the furnish. Together with the pulp, a range of additives can be used to tune the composition and performance of the paper. The major structural additive is filler, mineral or clay particles added *e.g.* in order to improve the optical properties of the paper (whiteness and opacity). Addition of filler typically interferes with the bonding between fibers, and thus reduces the strength of the paper.

Various chemicals can be added to the furnish for other purposes, such as retention aids added to fix filler particles and dyes for coloring.

2.1.3 Nanocellulose

Nanocelluloses denote a range of cellulosic materials with nanoscale dimensions. Following the classification of Klemm *et al.* [41], three main types exist:

- Cellulose nanofibrils (CNF)
- Cellulose nanocrystals (CNC)
- Bacterial nanocellulose (BNC)

CNC is the result of selectively dissolving the amorphous regions of microfibrils, liberating the crystallites as nanoparticles. Bacterial nanocellulose (BNC) is nanostructured cellulose synthesized by microorganisms.

Cellulose Nanofibrils

CNF, also called microfibrillated cellulose (MFC) or nanofibrillated cellulose (NFC) [41] was discovered in 1983 by Turbak *et al.* [64]. The term refers to the product of delaminating cellulose fibers into individual or bundled microfibrils [45]. A range of preparation methods for CNF have been developed. An overview is given by Lavoine [45], but in general they consist of a mechanical treatment. This may be preceded by a chemical or enzymatic pretreatment to aid in delamination. Mechanical treatments include:

- Homogenization - passing the pulp through a valve at high pressure
- Grinding
- Cryocrushing - crushing of pulp frozen with liquid nitrogen

Pretreatments are intended to ease the fibrillation and reduce the energy consumption of CNF production. Of note is TEMPO-mediated oxidation, modifying the cellulose by introduction of aldehyde and carboxylate groups. Repulsion between the charged groups promotes separation of the microfibrils.

Different size ranges are reported for CNF. A review by Lavoine *et al.* reports a diameter range of 20-60 nm [45], while Klemm *et al.* give a range of 15-20 nm [41]. In a 2011 review, Chinga-Carrasco reports that CNF prepared by homogenization is inhomogeneous, containing a variety of cellulose structures: fibrils, fines and fibers [9].

CNF as Paper Additive

CNF has been studied as a paper additive. In a 2014 review, Brodin *et al.* reported that CNF shows promise as a strength enhancer, and suggest two mechanisms: first, CNF fills pores and bridges separate fibers, thus increasing the bonded area. Secondly, CNF may form a coating on fiber surfaces, aiding in establishing interfiber connections during drying [5].

The interactions between CNF and ground calcium carbonate (GCC) filler particles have been studied by Hii, *et al.*, showing that fibrils coat the particles and contribute to bonding [27]. A 2015 paper by He, *et al.*, studies use of calcium carbonate-CNF aggregates as filler in paper. This addition strategy improved retention of filler in the paper compared to addition of CNF to the furnish [25].

A study by Korhonen and Laine of the effect of different CNF qualities on the filler flocculation and retention notes that the mechanism by which CNF contribute to bonding between filler particles is in question [43].

2.2 Scanning Electron Microscopy

The SEM is a versatile microscope, allowing observation with magnifications from the nanometre to the millimetre scale. SEM can be used for a wide range of samples, from metals to biological. It is usually used for studying the topography or composition of the sample surface.

The SEM works by scanning a focused beam of electrons over the sample surface. The incident electrons interact with the sample and emit electrons, which are picked up by a detector and taken as the signal. As the electron beam is raster scanned across the sample, the signal strength from each scanned spot is taken as the intensity in a corresponding grid of pixels. Decreasing the distance between scanned spots increases the magnification.

The beam is formed by emission of electrons from a source, which are accelerated by an applied voltage V_0 . The beam electrons therefore have a kinetic energy of $E_0 = eV_0$, typically given in keV. As the beam consists of charged particles, the flux can be described by the beam current I_B , *i.e.* the number of electrons hitting the sample per unit of time. Passing through a series of magnetic lenses, the beam is focused into an electron probe, *i.e.* a spot at the sample surface. The

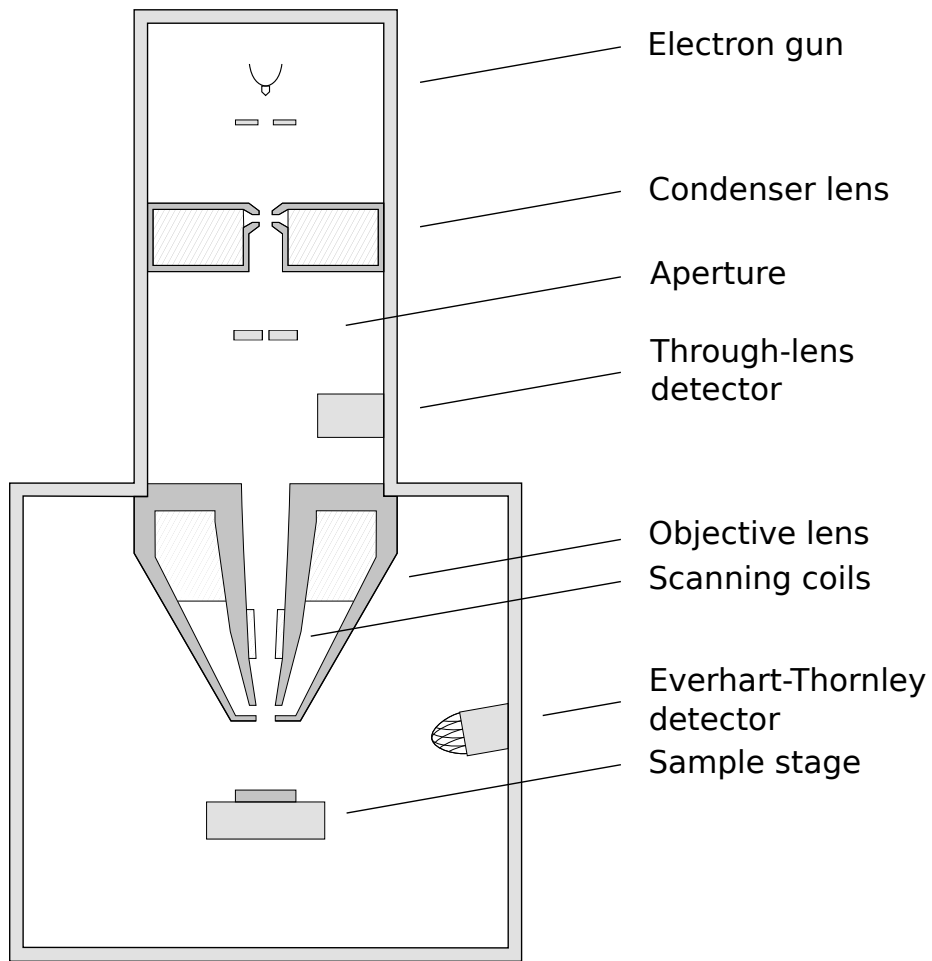


Figure 2: Schematic illustration of a SEM. Other configurations of lenses and detectors are possible.

diameter d of this spot is critical for the resolution achieved. When scanning, the beam is kept at each spot for a fixed time interval, called the dwell time τ .

2.2.1 Electron Column

The SEM consist of a vacuum chamber holding the sample on a stage, the electron column generating and focusing the beam, and one or more detectors. Figure 2 shows a schematic illustration of the SEM and components.

For mechanical movement of the sample, the stage is moved by actuators. Typically, a SEM stage has three translational axes and may have two rotational (rotation around and tilt with respect to the beam axis). For small adjustments and scanning, the beam is deflected by a scanning lens assembly.

Electron Source

The first step to forming an electron beam is emission of electrons from an electron source in the top of the column. Different types of sources exist, but all are generally composed of a cathode mounted above an annular extractor anode. Electrons are emitted at the cathode, and accelerated toward the anode. The electrons passing through the anode aperture form the beam.

The cathode-vacuum interface creates a junction and an energy barrier to emission, illustrated in Figure 3. The different electron sources overcome this barrier through different means. The simplest form of cathode is a heated tungsten filament, which releases electrons by thermionic emission. Upon heating of the filament, the electrons are given sufficient energy to overcome the energy barrier. However, this also gives the emitted electrons a large variation in kinetic energy [16], the effect of which is discussed in Section 2.2.1.

In a field emission gun (FEG), the cathode is usually a tungsten rod tapered to a very sharp point. The small radius causes a high electric field near the tip. Electrons are emitted by cold field emission, a process in which the electric fields cause the energy bands to bend, and for sufficient field strength, the energy barrier becomes thin enough for electrons to tunnel through to the vacuum. Operated at low temperature, the FEG gives little variation in the emitted electron energy compared to a filament source. The apparent source size is smaller, and the brightness higher [16]. For these reasons, FEGs allow better resolution than filament sources.

Electron Optics

The beam from the electron source passes through a series of magnetic lenses to form and focus the beam. Figure 2 shows the main components of the column. The lenses are axially symmetric coils around the beam path, contained in iron casings with precise gaps (polepieces) to concentrate the field lines in the column [16]. Electrons passing through the lens are deflected by the Lorentz force, giving them a converging, spiraling trajectory. The speed of electrons are conserved in a magnetic field, and hence the kinetic energy remains E_0 .

A simplified beam path is illustrated in Figure 4, where α is the beam convergence angle. The diverging beam from the electron source enters the condenser lens, which gathers the beam to a crossover. An aperture excludes part of the beam, *i.e.* all electron trajectories with an angle $\alpha > \alpha_i - \alpha_a$ to the optical axis in the figure. The strength of the condenser lens determines the position of the crossover and in turn the beam current I_B . A stronger condenser lens with a shorter focal length makes the electron probe diameter smaller, but excludes a larger portion of the beam, thus reducing the beam current [28].

The final lens is the objective lens, which focuses the beam into a final spot at the sample surface. The distance from the objective lens to the sample is called the working distance (WD). By varying the strength of the objective lens, the beam can be focused even if the WD is changed. Decreasing WD gives smaller d , and increases the beam divergence α [28].

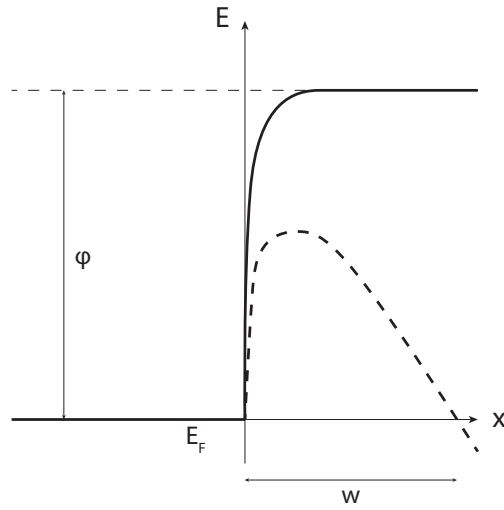


Figure 3: Energy diagram of cathode-vacuum junction. E_F is the Fermi level of the cathode, ϕ is the work function. The solid line shows the case for a thermionic emission source, where an electron supplied with a thermal energy ϕ can escape to the vacuum. The dotted line shows a field emission source. In an electric field, the energy level slopes. For a sufficient field, the barrier width w becomes small enough for electrons to tunnel to the vacuum. Illustration adapted from [16]

In addition to the condenser and objective lens, the beam passes through scanning coils, which deflect the beam in order to scan it across the sample surface. Due to small imperfections in the lenses, the beam is also subject to astigmatism, *i.e.* a deviation from cylindrical symmetry causing the beam to have an elliptical, rather than circular, cross section. The beam passes through manually controlled stigmator coils to correct for this [16].

For high resolution imaging, some SEMs can be operated in immersion mode, in which the sample is placed within the magnetic field of the objective lens, with very short WD. This increases resolution, but requires a detector within the electron column [16].

Beam Diameter

The beam is focused to a small spot on the sample surface, called the electron probe. This diameter d of the probe is decisive for the resolution achieved in SEM. The size of the probe is, as mentioned above, determined by the convergence angle α , the beam current I_B and the source brightness β . It can be calculated as [53]:

$$d_0^2 = \frac{4I_b}{\pi^2\beta\alpha^2}. \quad (2.1)$$

The electron beam is further broadened by optical aberrations. Interference between electrons in the lenses gives a widening due to diffraction, giving a diameter limit of approximately:

$$d_d = 0.6\frac{\lambda}{\alpha},$$

with α the convergence angle of the beam [1]. Further, the beam width is limited by chromatic aberration, *i.e.* that electrons of different energy have different focal lengths in the lens. The electron source is not monochromatic, generating electrons in a range $E_0 + \Delta E$. This gives a beam diameter limit of:

$$d_c = \frac{\Delta E}{E_0}C_c\alpha,$$

with C_c the coefficient of chromatic aberration [1]. Finally, the lenses are subject to spherical aberration, the focal length of the lens changing with the distance from the optical axis. This gives a limit:

$$d_s = \frac{1}{2}C_s\alpha^3,$$

with C_s the coefficient of spherical aberration [1]. Taken together, the final spot size d is approximated as [1][53]:

$$\begin{aligned} d^2 &= d_0^2 + d_d^2 + d_c^2 + d_s^2 \\ &= \frac{4I_b}{\pi^2\beta\alpha^2} + 0.6^2 \left(\frac{\lambda}{\alpha}\right)^2 + \left(\frac{\Delta E}{E_0}\right)^2 C_c^2\alpha^2 + \left(\frac{1}{2}\right)^2 C_s^2\alpha^6. \end{aligned} \quad (2.2)$$

The coefficients C_c and C_s have units of length and are approximately equal to the working distance [1].

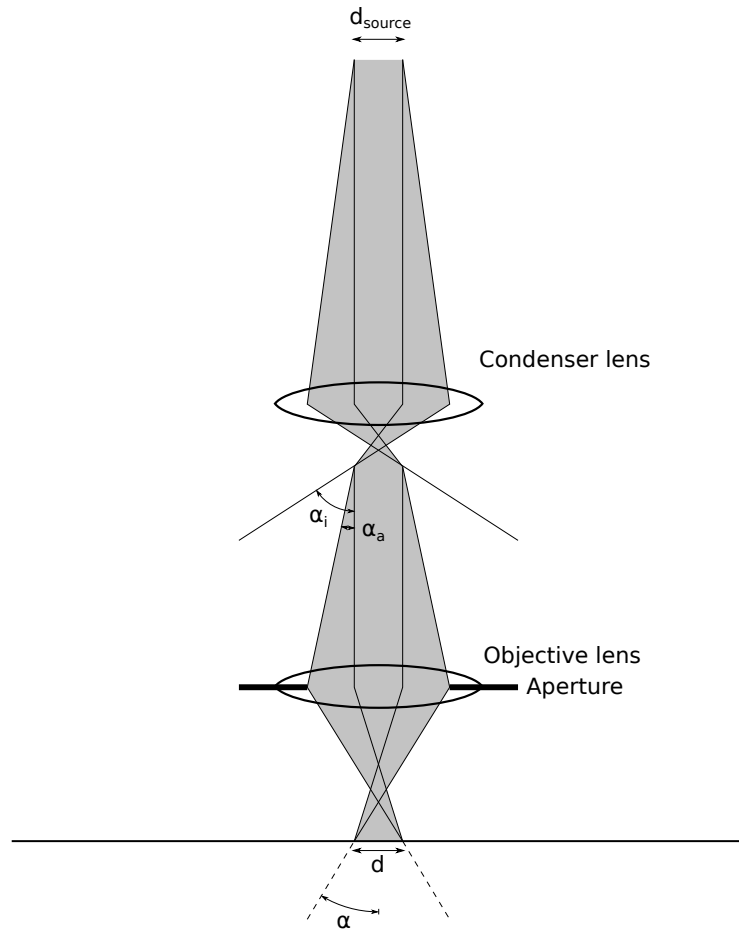


Figure 4: Beam path in the SEM. The apparent source size d_{source} is projected to a final diameter of d with beam convergence angle α . The aperture excludes the angle $\alpha_i - \alpha_a$ from the beam. Illustration adapted from [28]

Equation 2.1 suggests that d_0 can be made arbitrarily small while still maintaining any current simply by increasing α . However, including the aberration terms in Equation 2.2 demonstrates why this is not the case, as increasing α will at some point increase the diameter of the probe because of aberrations. Thus, a compromise must be found between the probe diameter d (and hence the resolution) and the beam current I_B (which determines the signal-to-noise ratio (SNR), discussed in 2.2.3) [1].

For thermionic emission SEMs, d_0 and d_s dominate Equation 2.2 for high energy E_0 (over 10 keV), d_0 and d_c at low energy. For FEG-SEMs, d_d and d_c dominate [53].

Equation 2.2 does not hold well for low E_0 . Chromatic aberration (which scales as $1/E_0$) becomes significant. This causes a broadening of the beam, and also a change in the beam profile [38], electrons off of the optical axis forming a skirt around the centre [23]. In addition to chromatic aberration, this is caused by electrons interacting at the beam crossovers, repelling each other and defocusing the beam. This is known as the Boersch effect, and scales with I_B and inversely with E_0 .

2.2.2 Electron-Sample Interactions

As incident primary electrons strike the surface, a range of interactions with the sample can take place. These cause particles to be emitted from the sample, among them backscattered electrons, secondary electrons, Auger electrons and characteristic and continuum x-rays. These may be detected individually or simultaneously, giving rise to a range of related characterization techniques.

For SEM, only the emitted electrons are of interest. Electrons emitted from the sample are divided into two types: backscattered electrons (BSE) and secondary electrons (SE), commonly associated with elastic interactions with sample nuclei and inelastic interactions with sample electrons, respectively. These physical processes are discussed in more detail, and some relevant equations are given in order to discuss how the signal changes with material and instrument parameters.

Elastic Scattering

Electrons moving through a material interact elastically with the sample nuclei through Coulomb attraction between the negative electrons and the positive nuclei. Because the mass of the electron is insignificant compared to that of the nucleus, the energy transfer to the nucleus is negligible. The electron is therefore scattered almost without energy loss, *i.e.* its direction of travel is altered, but not its speed.

An electron may undergo multiple scattering events, giving a complex trajectory through the material. A fraction of the incident electrons will receive a trajectory out of the material, and are thereby emitted from the sample. Such electrons are termed BSE. The number of BSE emitted is quantified by the backscattering coefficient η , defined as the number of backscattered electrons

per incident electron. This must necessarily be a number between 0 and 1.

The backscattering coefficient is a function of the target material, E_0 and the geometry. The dependence of η on the atomic number Z of the material is of particular importance, as it provides the physical basis for compositional contrast in SEM, discussed in 2.2.4. For $E_0 > 10$ keV, η is approximately independent of E_0 [38] and increases monotonically with Z . It can be approximated as [53]:

$$\eta = -0.0254 + 0.016Z - 1.86 \times 10^{-4}Z^2 + 8.3 \times 10^{-7}Z^3. \quad (2.3)$$

For compounds, Z is the sum of the component atomic numbers weighted with the mass fraction of each element. For lower values of E_0 , η generally increases for low- Z materials, and decreases for high- Z materials [38]. Below 1 keV, η varies strongly with E_0 and Z , and $\eta(Z)$ is not monotonic [53].

Inelastic Scattering

Incident electrons interact inelastically with the sample electrons, transferring energy to the latter through a variety of mechanisms, among them [53]:

- Inter- and intraband transitions
- Plasmon excitation in the surface or bulk
- Electron-electron scattering
- Ionization of electrons from the inner shell of the atom

These interactions with electrons in the sample atoms are delocalized, and may occur some distance away from the sample atoms [53]. In the Bethe approximation, a series of inelastic scattering events, each with some associated energy loss, is considered a continuous deceleration process of the primary electron. A primary electron that enters the sample will therefore, unless it is elastically scattered out of the material, gradually come to rest and be absorbed. The mean energy E_m of a primary electron is then a function $E_m(s)$ of the path length s . The rate of change in E_m is termed the stopping power S and may be approximated as [53]:

$$S = \left| \frac{dE_m}{ds} \right| = \frac{2\pi e^4 N_A \rho Z}{(4\pi \epsilon_0 A E)} \ln(1.166E/J), \quad (2.4)$$

with N_A the Avogadro constant, ρ the density and A the atomic weight and J the mean ionization potential of the target material. The range of electrons in the material may be calculated from the stopping power. The mean path length R of electrons as function of E_0 is given by [53]:

$$R = \int_0^{E_0} \frac{1}{-S} dE.$$

Electrons in the sample that receive sufficient energy from a scattering event can be excited from the valence band and move through the material. These are termed SE, and diffuse through the material, undergoing scattering events of their own. Thus, SE may escape the material, or cause the emission of further

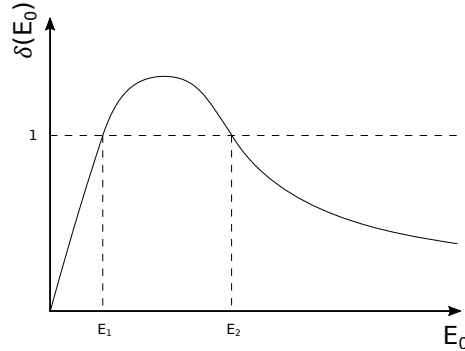


Figure 5: SE yield $\delta(E_0)$ for a typical material. δ increases for low E_0 , reaching a maximum before decreasing for increasing E_0 . At the two energies E_1 and E_2 , $\delta = 1$. Illustration adapted from [16].

SE. A single primary electron can therefore generate a cascade of secondary electrons, and many secondaries may escape per incident primary. Each inelastic scattering event transfers only a small amount of energy, and the initial kinetic energy of generated SE is therefore low, as is their range in the material.

The generated SE are quantified by the SE yield δ , defined as the number of emitted SE per incident electron. δ corresponds to the backscatter coefficient η , but as each primary electron can cause multiple SE to be emitted, δ can be bigger than 1. The energy distribution of generated SE is reported to be independent of beam parameters[1], and hence the SE escape distance is independent of E_0 .

The yield δ is a function of material and beam parameters, and a typical $\delta(E_0)$ for a material is illustrated in Figure 5. There exists a maximum for some E_0 , above which increasing the energy lowers the yield. The reason is that higher-energy primary electron (PE) undergo fewer scattering events within the SE escape distance. For energies below the maximum, δ is limited by the number of SE generated. Low energy PE can generate few SE, and so increasing the energy increases the yield, until a maximum is reached as the former effect becomes dominating [16].

Interaction Volume and Electron Signal

The trajectories of electrons through the material can be regarded as random walks, with elastic scattering events causing changes in direction, and inelastic scattering causing a continuous energy loss. This energy loss limits the length of trajectories, and means electrons are typically found within an *interaction volume* near the sample surface. The interaction volume, illustrated in Figure 7, is a useful concept to discuss the region of the sample contributing to the signal. Because electrons diffuse laterally through the material, the returning signal will originate from a region larger than the beam diameter. This imposes a limit on the resolution in SEM, because at some point it will be impossible to distinguish features even if the beam is made smaller.

The size and shape of the interaction volume varies with the density and atomic weight of the sample as well as the incident electron energy. Higher energy allows electrons to penetrate further into the material, while increased atomic weight of the sample increases the effect of elastic scattering[28].

A typical energy spectrum of all electrons emitted from the sample is shown in Figure 6. By convention, electrons with energy below 50 eV are taken to be secondary electrons[16]. Because SE are generated with low kinetic energy, their mean free path in the material is low. Therefore, only SE generated near the sample surface may escape, and the SE signal originates from a small volume. However, BSE scattered toward the sample surface may cause the generation of SE within the escape distance. These are termed SE2 (see Figure 7), and originate from a larger area. Further, BSE emitted from the sample may strike parts of the SEM chamber and cause the emission of SE, then called SE3 [16].

Electrons with higher energy are taken to be BSE. The BSE spectrum, which then covers the range from 50 eV to E_0 , has characteristic peaks for Auger electron emission, losses due to plasmon resonance, and a peak for elastically reflected electrons with energy close to E_0 . BSE can escape from approximately half the interaction volume [16], as an electron reflected at the halfway point will have just sufficient energy to escape.

X-rays penetrate most materials easily, and may therefore escape from essentially the whole interaction volume. X-ray methods like energy-dispersive X-ray spectroscopy (EDS/EDX) therefore have lower resolution than SEM.

SE and BSE may be distinguished in the instrument due to the difference in energy. Typically, SE imaging gives higher resolution than BSE due to the difference in contributing volume. SE and BSE carry different information about the sample and are subject to different contrast mechanisms, discussed in Section 2.2.4.

2.2.3 Detectors

The electrons emitted from the sample must be collected by a detector, generating a current proportional to the number of electron hits, which can in turn be interpreted as intensity of a pixel in the image. Different detectors may be

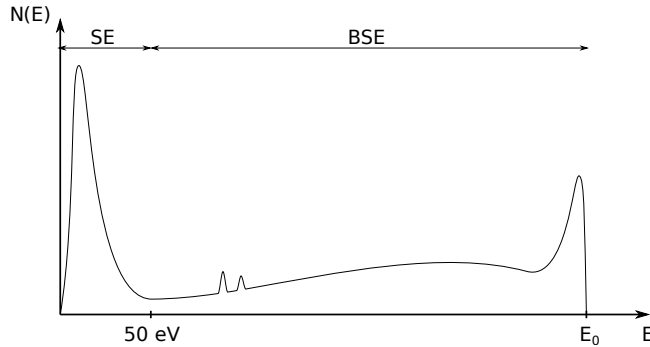


Figure 6: Emitted electron energy spectrum $N(E)$ (schematic). Electron with energy below 50 eV are taken to be SE, higher energy electrons BSE. The spectrum has peaks for Auger electrons and plasmon losses. The BSE spectrum has a peak near E_0 for elastically reflected electrons. Illustration adapted from [53].

employed to enhance different signals.

The signal strength S per incident electron can be expressed as a function of the material response (δ or η) and a detector efficiency ϵ . For BSE imaging [23]

$$S_{BSE} = \eta \epsilon_{BSE},$$

where ϵ_{BSE} is then a measure of the total quantum efficiency of the detector to BSE, *i.e.* the number of electrons detected per electron emitted. This total efficiency includes both geometric effects and the response efficiency of the detector. For some detectors, the response is sensitive to the energy distribution of BSE, and can therefore vary with η [23].

Both the electron generation at the source and emission from the sample are essentially random processes, and so is therefore also the signal strength from each spot scanned. Thus, there is always noise in the SEM signal, even if the emission probabilities δ/η and detection efficiency are constant. This noise is seen in the image as variations in the pixel intensity. It degrades the image quality and obscures the desired contrast. While noise is unavoidable, the best image quality can be obtained by maximizing the SNR [1]. Noise can be quantified by taking the histogram of the intensities from a region. It is then a distribution around some peak value, representing the signal. The standard deviation of the distribution is then a measure of the noise.

According to D. Joy, the theoretical SNR of the BSE signal (ignoring the detector efficiency) can be estimated as [1]

$$\text{SNR}_{theory} = \sqrt{6I_B\tau\eta}. \quad (2.5)$$

The SNR obtained in practice (SNR_{exp}) can be estimated from BSE images by a procedure described by Joy [1], and is related to the above theoretical SNR through the detector quantum efficiency (DQE) as:

$$\text{SNR}_{exp}^2 = (\text{DQE}) \text{SNR}_{theory}^2. \quad (2.6)$$

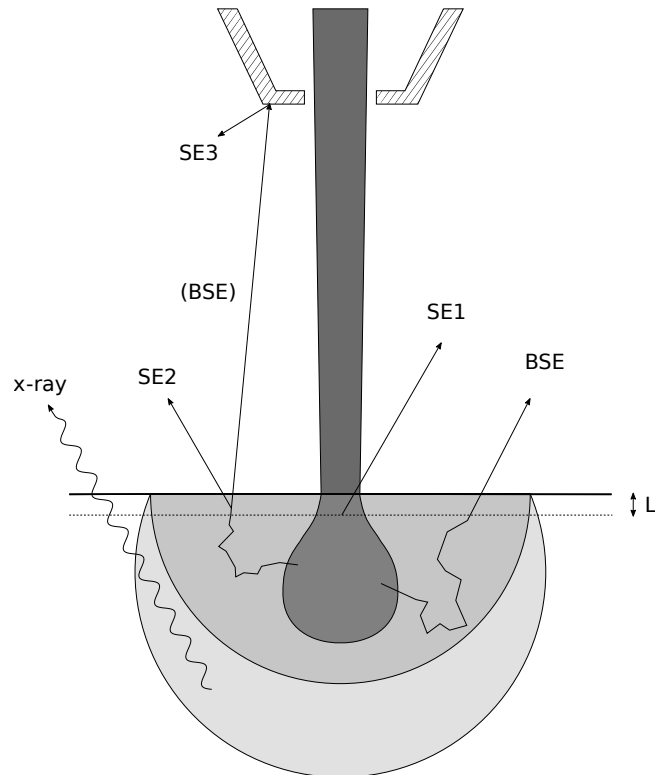


Figure 7: Interaction volume. The outer circle denotes the penetration depth of an electron. The dashed line indicates the SE escape depth L . The medium dark area is the volume from which BSE can escape. SE1 are generated by PE. SE2 are generated by BSE reaching the SE escape depth. SE3 are generated by BSE escaping the sample and hitting the chamber. Note that the SE1 signal comes only from a small volume. The BSE signal comes from a volume up to approximately half the penetration depth. Generated X-rays can escape from the whole interaction volume. Illustration adapted from [53].

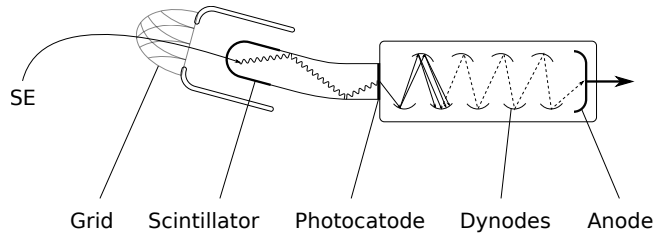


Figure 8: Everhart-Thornley detector. SE are attracted to the collector grid, hit the scintillator and generate photons. These follow the light guide to a photocathode, generating photoelectrons. These are attracted to a series of biased dynodes, each impact generating several SE. The final electron signal is collected by the anode. Illustration adapted from [53].

An approximation of relation between the experimental SNR and the imaging parameters is derived by Goldstein [23]. By imposing the Rose criterion, a rule of thumb stating that SNR above 5 is the limit for distinguishing features, an estimate of the beam current necessary to distinguish features from noise in a BSE image is [23]:

$$I_B > \frac{4 \times 10^{-12}}{C\tau(DQE)}, \quad (2.7)$$

where (DQE) is the detector quantum efficiency, τ is the dwell time and C is the material contrast.

Everhart-Thornley Detector (ETD)

The Everhart-Thornley detector (ETD) is a commonly used electron detector, usually mounted in the side of the SEM chamber. It is illustrated in Figure 8. Protruding into the chamber is a wire mesh with an applied bias with respect to the sample. Electrons passing through the grid are accelerated toward a scintillator. Electrons striking the scintillator generate photons, which are lead through a light guide to a photocathode, where they generate photoelectrons. These are accelerated through a series of dynodes, a series of electrodes positively biased with respect to each other. As electrons are attracted to and strike the first dynode, they generate multiple SE, which are in turn attracted to the second dynode, and so on. Finally, the electrons are collected by an anode. The current through the anode is taken as the signal strength. By this process, each incoming electron is multiplied manyfold, amplifying the signal [16].

The bias on the detector mesh with respect to the sample determines which electrons to collect. With a negative bias applied, only high-energy BSE can reach the detector, as low energy electrons are repelled. This gives pure BSE imaging. With a positive bias, low energy SE and BSE are attracted to the detector. High-energy BSE emitted within the angle of the detector are also collected. Hence, a positively biased ETD gives a combination of SE and BSE imaging [23].

Through-Lens Detector (TLD)

In immersion mode imaging, electrons emitted from the sample are captured by the magnetic field of the objective lens and travel up through the lens in spiraling trajectories [16]. Therefore, a detector must be mounted inside the electron column above the lens. The TLD is effective at attracting SE1 and SE2, but exclude a majority of BSE and SE3 [23].

2.2.4 Contrast Mechanisms

Contrast appears in SEM imaging when the number of electrons collected by the detector, the signal strength, varies with position of the spot scanned. This variation can be due to variation in the number of electrons emitted, or in the fraction of emitted electrons reaching the detector.

The contrast C between two scan spots can be quantified as

$$C = \frac{S_1 - S_2}{S_1}, \quad (2.8)$$

where S_1 and S_2 are the signal strengths from the two spots, and $S_1 > S_2$ [23].

Topographical Contrast

Topographical contrast appears due to variation in electron yield with the geometry of the sample surface, and gives an image of the surface topography. Several mechanisms contribute to topographical contrast, this follows the classification of Reimer [53].

The typical SE topographical contrast is due to the dependence of the SE yield δ on the surface angle, increasing for larger tilt of the surface. The reason for this is the limited escape depth of SE. As the surface is tilted, more of the interaction volume lies within the escape depth. The effect is illustrated in Figure 9a. This simple geometrical consideration gives $\delta(\theta) = \delta(0)/\cos(\theta)$ [16].

Diffusion contrast is the cause of the edge effect, *i.e.* edges of features appearing brighter in SEM. Scanning the beam close to an edge, more of the interaction volume is within the electron escape distance as electrons can escape through the sides of features [53].

Electrons emitted from the surface may hit features of the sample and be absorbed. This causes shadowing contrast, *i.e.* features of the sample appear to cast a shadow. This is particularly evident when using a side-mounted detector, giving images with a directional shadow [16].

Material Contrast

Typically associated with BSE imaging, material contrast is difference in signal strength from regions of different chemical composition. BSE material contrast arises because of the variation in η with the material properties as discussed in

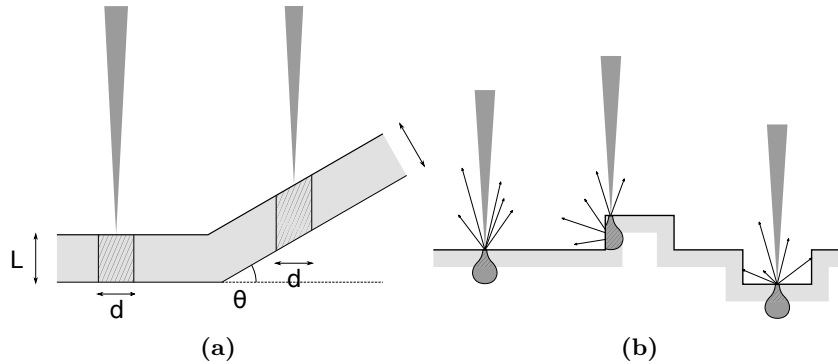


Figure 9: a) angle dependence of SE yield. L is the SE escape depth, d is the width of the interaction volume. Scanning at the flat surface, an area of Ld contributes to the signal. With a surface tilt of ϑ , an area of $\frac{Ld}{\cos\vartheta}$ contributes. b) shows effects of the sample geometry. The electron escape depth is marked in gray, the contributing volumes are hatched. Scanning close to the edge of a feature, electrons can escape through the sides, increasing the volume contributing (diffusion contrast). Scanning in a pore, emitted electrons can hit the sample and be absorbed, lowering the yield. Illustrations adapted from [16].

Section 2.2.2 and approximated by Equation 2.3. Assuming the detector efficiency is constant, BSE material contrast between two phases can be expressed in terms of their backscatter coefficients by Equation 2.8 as [23]:

$$C = \frac{\eta_1 - \eta_2}{\eta_1}.$$

The SE yield δ also varies with the material, but is highly dependent on the state of the sample surface due to the low penetration depth [53]. It is easily obscured by contamination, and not commonly seen in standard SEM [38], though it has been demonstrated for the 1-5kV range, where δ changes rapidly with E_0 [53]. For doped semiconductors material contrast has been demonstrated due to doping locally altering the electronic properties [50]. Some material contrast may also be observed in SE imaging due to SE2, generated by BSE. Differences in η may then be seen as differences in the SE image [53].

2.2.5 Sample Charging

Irradiating an insulating sample with the electron beam can cause the build-up of an electric surface charge. This causes artifacts in SEM images as the surface charge interferes with either the incident or the emitted electrons [38], typically showing up as spurious contrast.

Negative charging occurs if the sample absorbs electrons from the beam, without conducting them to ground. A sample may also be positively charged by the electron beam, as each incident electron can cause multiple SE to be emitted,

thus depleting the sample of electrons.

The currents into and out of the sample are illustrated in Figure 10. The electron beam current I_B enters the sample. A current I_{SC} goes from the sample to ground, while δI_B and ηI_B are the currents out of the sample due to emission of SE and BSE, respectively.

For an insulating sample, I_{SC} can be assumed negligible. The beam current must therefore be balanced by the emitted electron currents to maintain neutrality:

$$I_B = \delta I_B + \eta I_B.$$

Hence, $\delta + \eta$ must equal 1 to avoid charging. η varies with E_0 as discussed above, but less so than δ [38], so the BSE contribution is here ignored. A typical $\delta(E_0)$ for a material is illustrated in Figure 5. The criterion for charge neutrality is then held approximately at the two energies E_1 and E_2 where $\delta = 1$. For $E < E_1$ and $E > E_2$, $\delta < 1$, and the sample charges negatively. For $E_1 < E < E_2$, $\delta > 1$ and the sample charges positively.

Negative charging typically shows up as brighter in the SEM image [38]. First, because the negative surface charge repels electrons from the surface, thus increasing δ . Secondly, the charge sets up a potential retarding incident electrons. PE do not hit the surface with kinetic energy E_0 , but a reduced landing energy E_L . For $E_0 > E_2$, this increases δ . Additionally, a negative charge can deflect incoming PE, causing distortions or drift in the image. Mirror images of the SEM chamber can appear on the sample surface if incident electrons are repelled sufficiently. Electric discharges can occur off of the sample, showing *e.g.* as white scan lines in the image [53].

Factors Affecting Charging

It is of note that charging is not a phenomenon depending on the sample material alone. To maintain neutrality, $\delta + \eta = 1$, and as discussed in 2.2.4, δ and η may vary over the sample through several mechanisms. Therefore the charging behavior of the sample may also vary. A sample can of course be composed of several phases, each with different composition, and therefore with different E_2 points. Further, the sample topography influences δ , and therefore E_2 . As an example, electrons emitted in pores in the sample may be captured and reabsorbed, effectively lowering the yield and promoting negative charging.

Charging is also seen to vary with the instrument parameters used. Increasing beam current and dwell time increase the effects of charging, as more electrons per time strike the same spot on the sample. Higher magnification is also observed to cause charging [38].

A common technique to avoid sample charging when imaging insulating samples is to deposit a conducting layer on the sample surface [16], typically metal or amorphous carbon. Sputter coating or evaporation are typically used. Deposition of a surface coating may, however, have adverse effects on imaging. Due

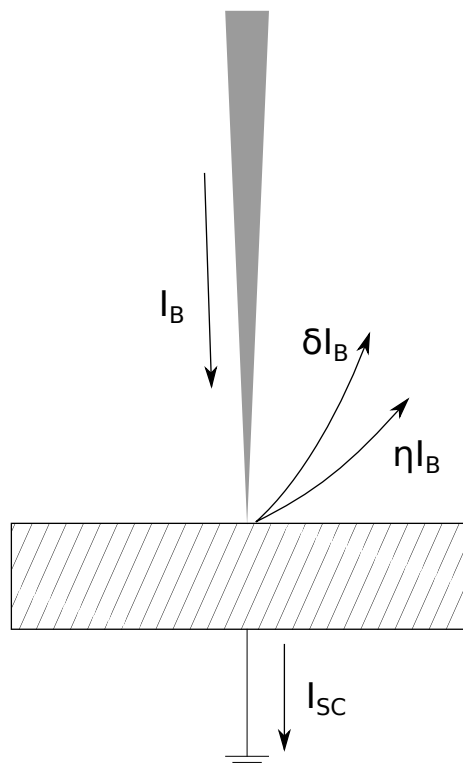


Figure 10: Currents into and out of the sample. I_B is the beam current, I_{SC} is the current from the sample to the grounded stage. δI_B and ηI_B are the currents due to emitted SE and BSE, respectively.

to the short SE escape depth, much or all of the SE signal will originate in the coating, and it is thus primarily the topography of the coating that is imaged, not that of the sample.

BSE imaging will also be affected, the signal strength changing from that of the pure substrate approximately linearly with the coating layer thickness [53], reaching that of the coating material when the coating thickness equals or exceeds the backscattering range. Material contrast will therefore decrease with an applied coating, disappearing entirely for a sufficiently thick layer.

Increasing the pressure in the SEM chamber (called environmental scanning electron microscope (ESEM)) can eliminate charging by ionizing gas molecules that attract to and neutralize the surface charge [16].

2.2.6 Low Voltage SEM

Low-voltage scanning electron microscope (LVSEM) refers to SEM using V_0 below 5 keV, down to a few hundred eV [38]. This is typically performed in order to reduce charging effects, but lowering E_0 has several consequences.

The optics of the SEM are affected. For one, the gun brightness is lowered and I_B decreases. Chromatic aberration becomes dominant, which together with the Boersch effect increases the size of the electron probe, reducing the resolution [23]. However, lower E_0 does also decrease the size of the interaction volume, reducing the area from which the signal originates.

The smaller interaction volume also means more of the signal is generated near the surface of the sample. While this allows the imaging of smaller, surface-specific features, it also means the imaging is more sensitive to surface contamination. This is of particular importance for BSE imaging. While the SE escape distance is independent of E_0 , the contributing volume for BSE decreases sharply with lower E_0 , and may indeed become smaller than that of SE [38].

Several contrast mechanisms are also affected by a lower acceleration voltage. SE topographical contrast is typically weakened because the angle dependence of δ becomes smaller. This is again due to the fixed SE escape distance. As E_0 becomes smaller, more of the interaction volume lies within the escape distance, regardless of the angle. For sufficiently small E_0 , the entire interaction volume is within the escape distance, and the angle dependence disappears entirely. Diffusion contrast becomes weaker for the same reason [38]. Material contrast becomes less pronounced for $1 \text{ keV} < E_0 < 5 \text{ keV}$ due to the dependence of η on E_0 mentioned in 2.2.2. Below 1 keV, the material contrast may reverse [53].

2.3 FIB

The FIB is a microscope similar in principle to a SEM, but using a focused beam of ions, typically Ga^+ . The ion beam can be used to image the sample,

but in addition, the heavy ions can mill the sample surface by ablation. The beam can be precisely scanned, and the FIB can therefore be used for highly precise alteration of a sample. Modern FIBs are combined with SEMs in one instrument, allowing *in situ* ion milling and imaging with either beam. This combined instrument is called a FIB-SEM or *dual beam* FIB.

In addition to imaging and milling, the FIB can be used for gas assisted etching (GAE) and deposition by introducing a gas and inducing chemical reactions with either beam. The FIB-SEM thus allows imaging with either beam while modifying the sample by material removal or deposition [65].

2.3.1 Instrument

The FIB-SEM is similar in construction to a SEM, with the addition of an ion column mounted in the chamber, at an angle to the electron column. The ion and electron beams coincide at a shared focal point. The sample, mounted on a stage, is moved to this point, in order to focus both beams on the sample. The stage can be tilted such that either beam is perpendicularly incident on the sample.

When the sample surface is precisely at the coincidence point of the beams, it is said to be at *eucentric* height [29]. The center of rotation for the stage tilt is the coincidence point. Thus, when the stage is at eucentric height, the same area of the sample remains in view and focus when the stage is tilted.

The FIB chamber must be kept in a vacuum of at least 1×10^{-4} Torr, as the ion beam will interact with gas molecules at higher pressures [62].

2.3.2 Ion Column

At the top of the column, gallium ions are generated by a liquid metal ion source (LMIS) consisting of a reservoir of liquid gallium connected to a tungsten tip. A negatively biased annular extractor electrode is placed below the tip. Molten gallium wets the tungsten tip, and a combination of the applied field and surface tension forms a Taylor cone. At the tip of this cone, the field is strong enough to ionize the metal and extract ions to the vacuum [65].

The beam passes through an aperture and a series of electrostatic lenses, focusing the beam onto the sample [48]. Stigmator and scanning coils correct for astigmatism and deflect the beam with high precision.

2.3.3 Ion-Sample Interactions

Ions striking a sample produce many of the same effects as electrons. The ions can interact elastically with sample nuclei or inelastically with electrons [35]. While FIB uses comparable acceleration voltages to SEM, the high mass of the Ga^+ ion compared to that of an electron causes more dramatic interaction effects. Comparing a Ga^+ ion with 30 keV kinetic energy to an electron with the

same energy, the ion will have a velocity $\sqrt{m_{Ga}/m_e} \approx 0.0028$ times that of the electron, but momentum $\sqrt{m_e/m_{Ga}} \approx 356.5$ times higher. As the mass of the incident ion is comparable to that of a sample atom, elastic collisions will entail a significant energy transfer. This makes the impact of ions with the sample more complex than the case for electrons. An overview of the physics is given by Imanishi [35].

Elastic collisions can cause a target atom to recoil, *i.e.* receive sufficient energy to be knocked out of position. This may also ionize atoms, creating secondary ions (SI). SE may also be generated in this process [22]. These particles will in turn undergo scattering events of their own, setting up a collision cascade. During this process, any of the particles may escape the sample - SE, backscattered primary ions, and atoms or ions from the sample. This ejection of atoms from the target is the physical basis for sputtering, material removal by ablation of atoms.

Ion Milling

The speed of ion beam milling is given by a sputtering rate, the number of atoms sputtered per time. This can be approximated as a product of the beam current (the number of ions hitting the sample per time) and the sputtering yield (the number of atoms sputtered per incident ion) [22]. The milling speed therefore increases linearly with the beam current.

The sputtering yield depends on the target material, and is shown in Figure 11 as function of atomic number for 30 keV gallium ions. It is also influenced by the incidence angle, as the interaction volume is closer to the surface for shallower angles (similar to topographic contrast in SEM). A maximum is obtained around 60-80° [35].

As material is sputtered from the surface, it may strike the sample and be re-deposited. For this reason, trenches milled into a surface will typically have sloping walls. As the trench is milled deeper, less material can escape, and more redeposition occurs [22]. A further cause of sloping walls is that the ion beam does not have a uniform intensity profile, but approximately a Gaussian distribution [65]. Milling depth is therefore not uniform within a sharply defined spot, but with some distribution around the beam centre. Simulated wall profiles caused by a milling with a Gaussian beam are shown by Ishitani, *et al.* [37], who also note that lower beam current gives straighter walls.

Because of redeposition and the angle dependence of the sputter yield, the result obtained when milling a volume depends on the milling pattern. For smooth sectioning, a pattern of milling line by line (milling sequential xz -planes) to the whole depth is preferred, rather than milling away sequential xy -planes [44]. In this work, this pattern is referred to as a cleaning cross section.

'Curtaining', streaks forming on milled surfaces parallel to the ion beam, is a well-known milling artifact. It can be caused by insufficient milling dose (ions per area), or different milling rates caused by inhomogeneities in the material or

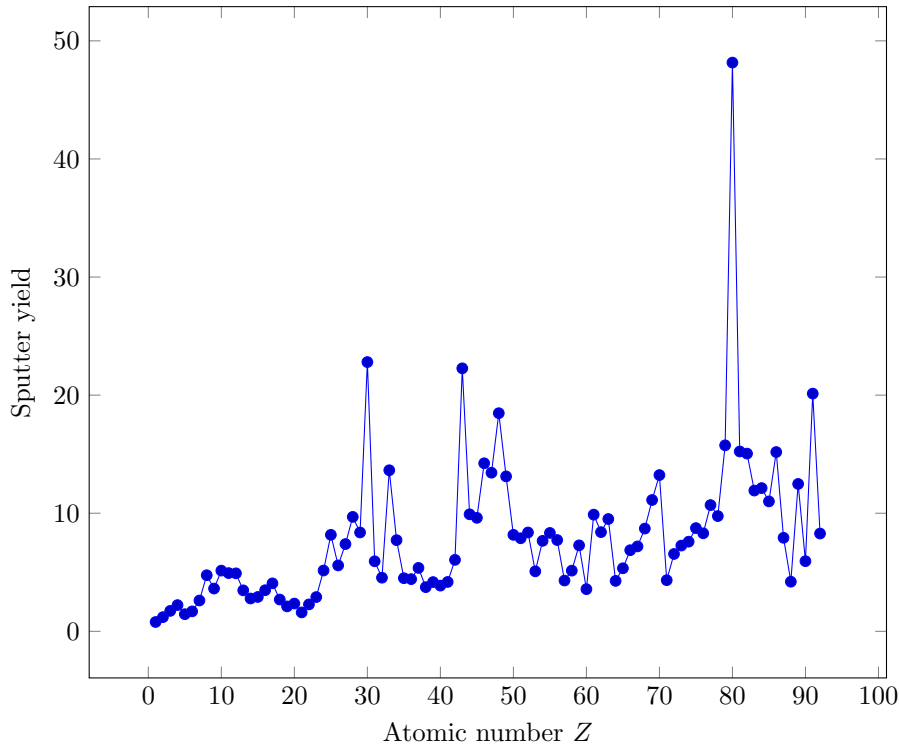


Figure 11: Sputter yield of the elements for milling with 30 keV Ga^+ ions, *i.e.* the number of atoms ejected per incident ion. Data from Gianuzzi *et al.* [21].

surface topography [51, 37]. The latter can *e.g.* be regions with differing sputter yield being milled at different rates. Deposition of a metal surface coating is advised in the literature to reduce this effect. Further, lower milling current can be used to mill a smoother surface, as this reduces the beam diameter [44, 18].

Scanning Ion Microscopy

The FIB can be used for imaging by collecting the emitted SE during scanning. Scanning ion microscopy (SIM) is similar to SEM, but with some differences in signal generation due to the use of heavy ions. SIM typically has lower resolution, but shows stronger contrast than SEM [48]. To limit the damage to the sample surface during imaging, low beam currents are typically used.

Topographic contrast is seen in scanning ion microscope (SIM), with the same mechanism as in SEM. Material contrast is reversed compared to SEM, with heavier target atoms giving less signal. For crystalline materials, contrast can be observed between grains in different orientations. This is called channeling contrast, and caused by the ions penetrating deeper for certain crystal orientations [48].

2.4 3D Methods

An overview of 3D imaging techniques are given below with examples of applications for paper materials. With the exception of X-ray methods, they are based on electron microscopy of sequential two-dimensional slices. In this work, a coordinate system is used where x and y refer to the horizontal and vertical axes of the image plane, xy . The z axis is then the direction into the image plane as illustrated in Figure 12.

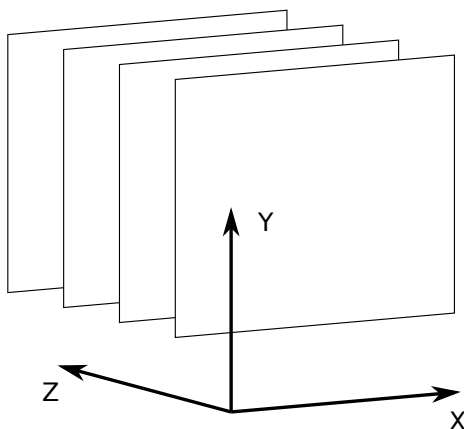


Figure 12: Coordinate system used in this work. For 3D imaging based on sequential slice imaging, the xy -plane is the imaging plane, the z direction into the plane.

2.4.1 FIB Tomography

3D microscopy by use of a single beam FIB was shown by Inkson *et al.* in 2001 [36]. The technique, here referred to as single beam FIB tomography entails milling a slice off the material using the ion beam, thus exposing a cross section. The sample is then tilted to bring the cross section into view, and it is imaged by SIM, *i.e.* also using the ion beam. However, the mechanical tilting of the sample introduces inaccuracies, and the slice thicknesses obtained were uneven and in the 100 nm range.

The introduction of the dual-beam FIB with ion and electron columns mounted at an angle to each other allowed FIB tomography using the SEM for imaging. This is the technique referred to in this work as FIB tomography. With the sample surface normal to the ion beam, the process consists of repeatedly milling a slice, then imaging the exposed cross section with the electron beam. The sample is not moved, and the beams are shifted by deflection. The method was first demonstrated by Holzer *et al.* in 2004 [33] for visualization of the microstructure of a BaTiO_3 sample. A slice thickness of 17 nm was achieved.

FIB has gained attention for use with 'soft' samples, such as biological samples [60, 19] and polymers [20, 63]. Low-voltage BSE imaging for FIB tomography is discussed in a 2008 article by Winter, *et al.* [11] for use with insulating

samples, achieving xy -resolution in the 5-10 nm range for epoxy-embedded biological samples. An overview of the development of FIB tomography is given by Holzer and Cantoni [32]. In the same review, a $10 \times 8 \times 8 \mu\text{m}^3$ tomogram of a biological sample with $5 \times 5 \times 5 \text{ nm}^3$ resolution is presented, with an acquisition time of 40 hours. This demonstrates the possible resolution, but also the long time necessary for high resolution imaging.

The resolution attainable in FIB tomography can be divided into two: in the xy -plane, it is determined by the SEM imaging, and thus subject to the same limitations as normal SEM. The z resolution, *i.e.* the thickness of the milled slices, is limited by the diameter of the ion beam and the precision of the beam control. Drift, apparent movement of the sample relative to the ion or electron beams is a major problem for FIB tomography. This can be caused by mechanical drift (movement) of the stage, or electrostatically by charging [32, 52]

No publication has been found using dual-beam FIB-SEM tomography for paper materials, though use of single-beam FIB has been demonstrated. The technique is discussed briefly in a 2009 review of characterization methods by Chinga-Carrasco, and a visualization of a reconstructed volume created by Heard is presented [10]. Papers by Heard, *et al.* [26] and Koivula, *et al.* [42] demonstrate the use of single beam FIB for milling and imaging of cross sections for studies of ink penetration in paper. The former also makes use of the FIB for secondary ion mass spectrometry (SIMS) imaging and TEM sample preparation. A 2010 paper by Domenges *et al.* [14] demonstrate a single beam FIB used successfully to prepare and image cross section images of flax fibers. The fiber is not embedded, but a $2 \mu\text{m}$ thick platinum pad is deposited on the surface. The cross section is milled using a beam current of 1 nA, then tilted to 45° and imaged with 4 pA.

Mechanical Sectioning Electron Microscopy Methods

Manual serial sectioning of a sample for electron microscopy was demonstrated already in 1955 by Birch-Andersen [3]. Very thin slices of a sample can be prepared by microtome, but handling and mounting of the slices is time-consuming. Blumer *et al.* [4] describe a method of sectioning a sample for optical microscopy to form a connected ribbon of sequential slices. This has been demonstrated for electron microscopy with slice thickness of 35-50 nm for biological samples [24]. Such a series of thin sections can be imaged with either SEM or TEM, then referred to as serial section scanning electron microscopy (SSSEM) and serial section transmission electron microscopy (SSTEM). The latter has the superior xy -resolution of TEM. These methods are non-destructive, as the slices are not necessarily destroyed during imaging.

For SEM-imaging, only the sample surface is imaged. It is therefore not necessary to create thin, electron-transparent samples. It is possible to image the surface of the whole sample and then remove a slice to expose a new cross section. Different techniques for slice removal with different z -resolutions have been demonstrated. The xy -resolution is determined by the SEM used, and subject to broadly the same limitations for all methods. These slice-removal methods

are generally destructive.

Serial block face scanning electron microscopy (SBFSEM) is a technique using imaging with SEM and in-situ mechanical sectioning with an ultramicrotome. It is similar to FIB tomography, but with a different cutting method. SBFSEM was demonstrated in 2004 by Denk and Horstmann [13] with a custom-built instrument. SBFSEMs are now commercially available. For each cycle of SBFSEM, the sample is sliced by the microtome, imaged and the stage is then moved upwards to position the sample for the next slice. Compared to FIB tomography, the method has lower z-resolution. Hughes *et al.* mention 25 - 30 nm as a lower limit, but 50-100 nm as typical, and note that this is dependent on the mechanical properties of the sample [34]. SBFSEM can be performed under variable pressure to avoid charging issues.

Zankel *et al.* demonstrate the use of automated SBFSEM for paper materials in a 2009 paper [66]. 100 slices of 200 nm thickness were imaged by BSE imaging at 10 kV under 65 Pa water vapour atmosphere.

Slice removal by mechanical grinding and SEM has been demonstrated for 3D reconstruction of paper materials with z-resolution of around 1.5 μm by Chinga, *et al.* in a 2003 paper [8]. Spherical polymer beads of known size were embedded with the sample, and their cross sections used to estimate the slice thickness.

X-ray Methods

X-ray tomography has been successfully applied to paper materials. The working principle is discussed in a 2001 paper by Samuelson, *et al.* [57], and applications are discussed by Holmstad in a 2003 paper [31]. An effective resolution of around 1 μm (voxel side length) for a volume of approximately 0.5 mm by 0.2 mm by the paper thickness is achieved. The method is non-destructive, but requires synchrotron radiation.

Recently, ptychographic X-ray methods have been developed with superior resolution to conventional X-ray tomography. Ptychographic X-ray imaging was first demonstrated by Rodenburg, *et al.* in 2007 [54] and an overview is given in a review by Chapman and Nugent [7]. In 2014, ptychographic X-ray tomography with resolution of 16 nm was achieved [30]. The technique has been used for tomography of silk fibers in a humid atmosphere, showing the potential for the method for in-situ use with biological materials [17]. A volume of 27.1 μm by 13.3 μm by the fiber thickness was recorded with resolution of 20 nm (though features of less than 50 nm were reportedly not resolved clearly) in 7 hours.

2.5 Monte Carlo Simulation

The Monte Carlo method is an approach to simulation. In brief, instead of attempting to fully simulate a process from physical principles, Monte Carlo methods use random draws from probability distributions to simulate the behavior of a system. Monte Carlo is well suited to simulation of electron trajec-

ries for SEM, because the physical interactions are complex but the individual trajectories are unimportant, what is of interest is the aggregate behavior of many electrons [39].

The CASINO program [12] is used for Monte Carlo simulation in this work. Supplied with the target material composition (atomic weight fraction) and density, it simulates an electron trajectory as a series of elastic collisions and a continuous energy loss due to inelastic interactions. The distance between collisions and the scattering angle is determined randomly from probability distributions determined by the material properties. This is repeated for each electron until it either escapes the material or its energy is reduced to below 50 eV [15].

2.6 Image Processing

Two image types are used in this work: 8-bit and binary images. 8-bit grayscale images are stored as an array of pixel intensity values each of 8 bits, *i.e.* a number between 0 and 255. The histogram of a grayscale image refers to the distribution of pixel counts per intensity value. In a binary image, each pixel can only take two intensity values: 0 or 1. The image operations used in this work are listed and briefly explained below. A thorough treatment is given by Russ [55].

Grayscale Image Operations

Median filtering: for each pixel in turn, the intensity value is replaced by the median of the intensity values of the neighboring pixels within the radius. Median filtering removes single pixels with extreme value compared to their neighborhood, and is thus done for removal of random noise.

A Gaussian blur is similarly a neighborhood operation, replacing the value of a pixel with an averaging of the pixel values within a given radius. The pixel values are weighted according to a two-dimensional Gaussian distribution centered on the original pixel. This blurs or smooths out an image.

Background removal (or leveling) an image refers to correcting for systematic uneven brightness values in an image, caused *e.g.* by uneven illumination. This is done by subtracting a background image for the original image (*i.e.* subtracting each pixel intensity value from the corresponding value in the original image). The background image can be recorded directly, or generated, *e.g.* by fitting of a polynomial function.

Segmentation

Segmentation refers to dividing an image into regions corresponding to features, assigning each pixel to a region. This separates features from the background or from each other, and is necessary for quantitative image analysis. Segmentation can be done manually (*e.g.* marking the image by 'painting'), but a range of algorithms and routines exist.

Thresholding is a segmentation routine based on assigning pixels to either foreground or background, based only on the pixel intensity value. A threshold range is set (manually or by some algorithm). Pixels with intensity within the range are taken as foreground. Thresholding a grayscale image yields a binary image.

Binary Image Operations

In a binary image pixels intensities are either 1 or 0, for simplicity here referred to as on or off. For examples, a binary image segmented into foreground (on) and background (off) pixels is assumed.

Erosion refers turning off pixels that are on and have neighboring pixels that are off. For a binary image consisting of features and background, this removes a layer of pixels from the edges of all features. Erosion can be done with a numerical threshold, removing a pixel only if the number of neighbors turned off exceed the threshold.

Dilation is the opposite of erosion, turning on a pixel if it is touching pixels that are on. It can also be used with a threshold. Dilation pads features with a layer of pixels, and can also be used with a threshold

Opening refers to an erosion followed by a dilation. *Closing* is a dilation followed by an erosion. Altering the order of operations produces a different result.

3

Materials and Methods

3.1 Monte Carlo Simulations

Monte Carlo simulations were performed using CASINO v.3.2.0.4 [12]. In the software, the sample geometry and composition are defined, the latter by density and chemical formula. As the precise composition of the Epofix resin used in this work is not available from the manufacturer, it can not be simulated accurately. Simulations are therefore performed for cellulose and calcium carbonate.

For all simulations here, 1×10^6 electron trajectories were simulated. A 1 nm beam diameter was used, with no simulated shot noise. SE generation was not simulated. The default physical models were used. For each simulation, 200 electron trajectories were saved for visualization of the interaction volume.

A list of the simulations performed:

- flat surfaces of cellulose and calcium carbonate at 2 and 5 keV, simulating the backscatter coefficient η . Distributions were collected of the maximum penetration depth of all electrons, the maximum depth of BSE and the radial distribution of BSE (distance from the beam centre where BSE are emitted).
- flat cellulose surface covered with 20 nm layer of Pt/Pd at 5 kV, simulating the backscatter coefficient.
- surfaces of cellulose and calcium carbonate angled at 52° to the beam, collecting the angular distribution of BSE

3.2 Instruments

FIB

A FEI Helios Nanolab dual-beam FIB was used. The instrument has a 5-axis stage (translation, rotation and tilt) with the ion column mounted at 52° to the electron column.

The electron column has a range of acceleration voltages from 0.5 to 30 kV. It uses a FEG, and has two detectors: a side-mounted ETD and an in-column through-lens detector (TLD) for operation in immersion mode. The apertures available range from 8 to 64 μm (Ken Roger Ervik, NTNU NanoLab, 2016[pers.comm.]). The instrument has a nominal maximum resolution of 1.2 nm.

The coincidence point of the two beams is at 4.1 mm WD for the electron beam, 16.5 mm for the ion beam. A gas injection system is available for deposition of platinum.

FEI Slice & View G2

The software used for performing tomography in the FIB. The order of operations has relevance for the experiments, and is therefore described here. Starting the software, the experiment is set up by:

- The milling current and SIM imaging parameters (image resolution and dwell time) are set, as is SEM image resolution (in pixels) and dwell time.
- A SIM image is captured using the milling current.
- On this image, a rectangle is drawn by the user, marking out the surface of the volume to be imaged (*i.e.* xz -surface of the volume). The depth (y) is set, as is the number of slices. A fiducial mark is placed automatically. It can be placed on the left or right of the area, but its precise position can not be altered.
- The fiducial mark is made automatically by depositing a pad of platinum and then milling
- Optionally, a pad of platinum is deposited on the whole area to be imaged
- Optionally, a rough cut with arbitrary current can be made. The xz -dimensions are then marked as a rectangle on the SIM image, connected to the area marked for imaging.

The automated procedure is then started, consisting of repeated cycles of:

- A SIM image is captured using the milling current, with the chosen SIM imaging parameters. The software recognizes the fiducial mark, and from its position determines the alignment.
- A slice is milled
- The SEM is dynamically refocused and deflected to be centered on the new cross section
- A SEM image is captured

This process is repeated until the whole volume is imaged. At any point, the procedure can be paused and the microscope can be manually controlled. This is used to set the electron beam current and magnification. Note that the milling depth set during setup is calibrated for silicon, and is therefore not accurate for milling in other samples. It is hereafter termed the nominal milling depth, and used only for ease of comparison. The milling depth and current together determine the ion dose (incident ions per area).

SEM

A Hitachi SU3500 filament SEM was used for low magnification imaging.

Ion Mill

A Hitachi IM4000 ion mill was used for polishing cut cross sections. The instrument produces a broad beam of Ar^+ ions. The sample is mounted on a stage in the beam path. A tungsten mask is mounted over the sample, so that only the protruding part of the sample is milled. The sample can be oscillated in the beam at variable speed. The ion beam acceleration voltage and milling time can be set.

3.3 Sample Preparation

Paper Samples

Paper handsheets of 60 g m^{-2} were prepared by Vegar Ottesen using thermo-mechanical pulp and varying dosages of GCC filler and CNF prepared by Clafin grinding and homogenization. The preparation is described in more detail in [49]. Kemira Fennopol 3500P (cationic polyacrylamide) and Kemira Altonit SF (bentonite) were used as retention chemicals. Samples of two paper qualities were used in this work, composed of 35%_{wt} GCC and a) 3%_{wt} CNF added to the furnish (here referred to as 35-3 furnish), b) 3%_{wt} CNF added to the filler fraction (here referred to as 35-3 filler).

3.3.1 Sample Preparation for FIB

Different methods of sample preparation were tried. The methods used are described here, and which methods were applied are mentioned in the descriptions of the experiments.

Staining

Paper samples were stained with uranyl acetate by Nan Tostrup Skogaker at St. Olav hospital according to the following protocol: 200 μL of 4% uranyl acetate in 50% ethanol were diluted with 600 μL 100% ethanol, giving a solution of 1% uranyl acetate in 90% ethanol. This was centrifuged for 10 minutes at 10000 rpm. Drops of the solution were deposited in a beaker, and the paper samples were immersed in the drop for 20 minutes. Thereafter, the samples were dried and left to air dry for five minutes. Thereafter, the samples were washed in excess ethanol.

Embedding

Samples are embedded in EpofixTM two-part epoxy resin (Electron Microscopy Sciences, catalog no. 1232). Epoxy and hardener are mixed in the mass ratio 25:3 and stirred for two minutes.

Two approaches were tried for embedding samples. The first is here termed cylinder embedding, where multiple paper samples were placed in a plastic clip

and put in a cylindrical mold which was filled with epoxy. The mold was set in a vacuum chamber at 200 mbar for 30 minutes, and kept overnight at 40 °C. They were then left to cure overnight. The face of the cylinder was mechanically ground and polished using ethanol as lubricant. The cylinder was sectioned, cutting of the top 5 mm to fit the FIB sample chamber.

The other method is here termed block embedding. The preparation was as follows: Single paper samples were put individually in small molds. Each was filled with mixed epoxy and put in a vacuum chamber at 200 mbar for 30 minutes. The paper samples were then taken out of the epoxy and placed between glass cover slides. These sandwiches were placed between large glass slides covered with plastic film and an approximately 20 g weight were placed on top. The samples were then left to cure overnight.

Ion Milling

Samples were cross sectioned with a scalpel, and the cut surface was polished using the ion mill. Approximately 100 μm of the sample was protruding past the mask. Samples were milled for 6 hours with 3.8 kV acceleration voltage.

Mounting and Coating

Using carbon tape, samples were mounted on sample stubs. Copper tape was added to hold the sample securely and ensure conductivity. A coating of Pt/Pd (80/20 by weight) was deposited on the samples using a Cressington 208 HR B sputter coater with an MTM-20 thickness controller. The samples were tilted during deposition to achieve a continuous layer from the face of the sample to the copper tape on the sides.

3.4 FIB-SEM Experiments

Measurement of Electron Beam Current

The electron beam current in the FIB-SEM is set from a list of predetermined values. The precise beam current was measured by use of a Faraday cup, *i.e.* a deep hole in a conductive substrate. The electron beam was pointed at the bottom of the hole and spot scanned, kept still at one spot while running. The sample current I_{SC} from the substrate to ground is measured. Assuming no electrons are emitted from the hole, the sample current is equal to the beam current. This was performed for acceleration voltages of 2 and 5 kV and the nominal beam current ranges 0.34 nA – 2.7 nA and 43 pA – 0.69 nA respectively.

Estimation of Detector Efficiency

Following the approach of Joy [1], the BSE quantum efficiency of the TLD was calculated by estimating theoretical and experimental SNR and using Equation 2.6.

In brief, BSE micrographs were taken at different beam currents (0.17 nA and 0.34 nA nominal beam current) from a surface with as little intensity variation

as possible, in this case areas of an ion milled epoxy block coated with 20 nm Pt/Pd. The brightness and contrast settings were not altered between acquiring the images, and the intensity level of the images was then assumed to be linear with the beam current with an offset for the brightness setting used. This offset was determined, and the experimental SNR estimated by dividing the signal level (minus the offset) by the signal standard deviation.

3.4.1 Imaging Parameters

To establish a range of usable imaging parameters, a FIB-milled cross section was imaged in SE and BSE modes using 2 and 5 kV acceleration voltages. A range of currents from 86 pA to 2.8 nA were used.

3.4.2 FIB Tomography

For all tomography experiments, the same general procedure was used, with variation of parameters, samples and order of operations where noted. The experiments consist of aligning the beams and setting the sample height, preparing the area for tomography and then performing tomography.

For all experiments, the following routine was used for alignment: first, a region of interest was found. With the sample at 0° tilt (*i.e.* normal to the electron beam), the stage height was then set to the eucentric height. This was done by centering the SEM field of view on a recognizable feature and tilting the stage to 7°. The stage height was adjusted until the feature was centered again. The tilt was then increased to 52°, normal to the ion beam.

The electron and ion beams were aligned by moving the stage so that a recognizable feature was centered in the SEM image at low magnification. Using the same magnification, the same feature was found in the SIM image. Using beam deflection, the SIM image was centered on the feature. To reduce damage to the sample, a low ion beam current of 0.28 nA was used.

The area was then prepared by milling a front trench with high ion beam current (6.5-21 nA), before the S&V software was used as described above. A summary of the tomography experiments performed are shown in Table 3.1 and described in more detail below. Experiments are referred to by ASV (Auto Slice and View) and a number. The ion dose given here is as supplied from the instrument.

ASV1

Non-stained 35-3 furnish sample. 2048x1768 pixel BSE images with a horizontal field of view of 15.95 μm were captured at 2 kV using an electron beam current of 0.69 nA with a dwell time of 10 μs . An xz area of 8.71 μm by 3.86 μm was used, with a nominal milling depth of 3 μm , corresponding to an ion dose of 8.5 nC μm^{-2} . 100 slices were milled at 0.46 nA ion beam current, giving a z -resolution of 38.6 nm.

Table 3.1: List of FIB tomography experiments with main parameters.

Experiment	ASV1	ASV2	ASV3	ASV4	ASV5	ASV6
Sample	Non-stained 35-3 furnish	35-3 furnish	35-3 furnish	35-3 furnish	35-3 filler	35-3 filler
I_B (nA)	0.69	1.4	1.4	1.4	0.69	1.4
τ (μs)	10	30	30	30	30	30
Milling current (nA)	0.46	0.28	0.28	0.093	0.093	0.093
Slice thickness (nm)	38.6	16	16	15	20	20
Slices	100	113	217	242	248	36
xz -area (μm^2)	8.71 x3.86	11.71 x1.8	22 x3.47	24 x3.63	19.73 x4.96	15 x0.72
Nominal depth (μm)	3	4	5	5	4	5
Ion dose ($\text{nC } \mu\text{m}^{-2}$)	8.5	8.12	10.15	7.53	6.02	7.53
Milling time (s)	621.3	611.3	2768.9	7053.9	6334.6	874.5
Image resolution (px)	2048 x 1768	1024 x884	1024 x884	1024 x884	1024 x884	1024 x884
Image time (s)	36.2	27.1	27.1	27.1	27.1	27.1

ASV2

UA-stained 35-3 furnish sample with 5 nm Pt/Pd coating. 1024x884 pixel images with horizontal field of view $12.80 \mu\text{m}$ were taken at 2 kV with 1.4 nA electron beam current and a dwell time of 30 μs . The xz -area was $11.71 \mu\text{m}$ by $1.8 \mu\text{m}$, with a nominal milling depth of $4 \mu\text{m}$, corresponding to an ion dose of $8.12 \text{ nC } \mu\text{m}^{-2}$. 113 slices of 16 nm thickness were milled using 0.28 nA ion beam current.

ASV3

UA-stained 35-3 furnish sample with 15 nm Pt/Pd coating. The same milling and imaging parameters were used as in ASV2, with xz area of approximately $22 \mu\text{m}$ by $3.47 \mu\text{m}$ and $5 \mu\text{m}$ nominal milling depth, corresponding to an ion dose of $10.15 \text{ nC } \mu\text{m}^{-2}$.

ASV4

UA-stained 35-3 furnish sample with 15 nm coating of Pt/Pd. 1024x884 pixel images with horizontal field of view $12.80 \mu\text{m}$ were captured at 2 kV, using 1.4 nA electron beam current and dwell time of 30 μs . The xz -area was $24 \mu\text{m}$ by $3.63 \mu\text{m}$ with a $0.5 \mu\text{m}$ thick Pt pad deposited. 242 15 nm thick slices were milled to a nominal depth of $5 \mu\text{m}$ using ion beam current of 93 pA, corresponding to an ion dose of $7.53 \text{ nC } \mu\text{m}^{-2}$.

ASV5

UA-stained 35-3 filler sample with 20 nm coating of Pt/Pd. 1024x884 pixel images with horizontal field of view 12.80 μm were captured at 2 kV, using 0.69 nA electron beam current and dwell time of 30 μs . The xz -area was 19.73 μm by 4.96 μm with a 0.5 μm thick Pt pad deposited. 248 20 nm thick slices were milled to a nominal depth of 4 μm using ion beam current of 93 pA, corresponding to an ion dose of 6.02 nC μm^{-2} .

ASV6

UA-stained 35-3 filler sample with 20 nm coating of Pt/Pd. 1024x884 pixel images with horizontal field of view 12.80 μm were captured at 2 kV, using 1.4 nA electron beam current and dwell time of 30 μs . The xz -area was 15 μm by 0.72 μm with a 0.5 μm thick Pt pad deposited. 36 20 nm thick slices were milled to a nominal depth of 5 μm using ion beam current of 93 pA, corresponding to an ion dose of 7.53 nC μm^{-2} .

3.5 Image Processing

The goal in image processing was to obtain binary images of each of the material phases, in order to perform 3D visualization.

3.5.1 Preprocessing

The 8-bit image stacks from the instrument were preprocessed for segmentation using Fiji [59, 58]. First, the contrast was automatically adjusted, *i.e.* clipping the histograms to fill the whole dynamic range. The histogram of the entire stack was used, and the same adjustment applied to all images. The images were aligned using the SIFT algorithm in Fiji. The stack was then cropped manually trying to maintain the biggest possible volume but removing any visible block edges.

Where noted, uneven illumination was corrected by a pseudo-flat-field background removal step. First, a false background image was composed by extracting regions of the background and assembling a mosaic image. This was adjusted in size to match the images and evened using a Gaussian blur with radius of 50 pixels. The false background image was then subtracted from the image stack.

3.5.2 Segmentation

The preprocessed image stacks were segmented using MIPAR [61]. The full segmentation recipe consists of two main processes. First, a high threshold was applied, selecting only the GCC particles. Thereafter, a mid-range range based thresholding selected all foreground features. From this mask, the GCC image was subtracted, leaving the cellulose. These two segmented images then contain only the GCC and cellulose, respectively.

3.5.3 Reconstruction

The binary image stacks were visualized using the Amira software (Visage Imaging GmbH, Berlin and the Zuse Institute, Berlin). After importing the image stacks, the volume is visualized by volume rendering.

4

Results

4.1 Monte Carlo Simulations

The raw data results from the simulations are included in the attachments. The simulated backscattering coefficients from flat surfaces are displayed in Table 4.1. 200 electron trajectories are visualized in Figure 13, with BSE trajectories in red. The coordinates are given in nm. Figure 14 show the collected distributions. a) and b) show show the maximum depth reached by all electrons and backscattered electrons, respectively. The 95th percentile of the latter is shown in Table 4.2. Figure 14 c) shows a semilogarithmic plot of the distribution of BSE surface radius, *i.e.* the distance from the beam center where BSE are emitted. Note that the distribution gives count per area as a function of radius, *i.e.* it is normalized for count and area. This is integrated to get total count as function of radius. The cumulative sum as function of radius is plotted in Figure 14 d). The 95th percentile of this distribution is shown in Table 4.3. These are then the radii within which 95% of BSE are emitted.

Table 4.1: Simulated backscattering coefficients and contrast with cellulose, assuming constant detector efficiency

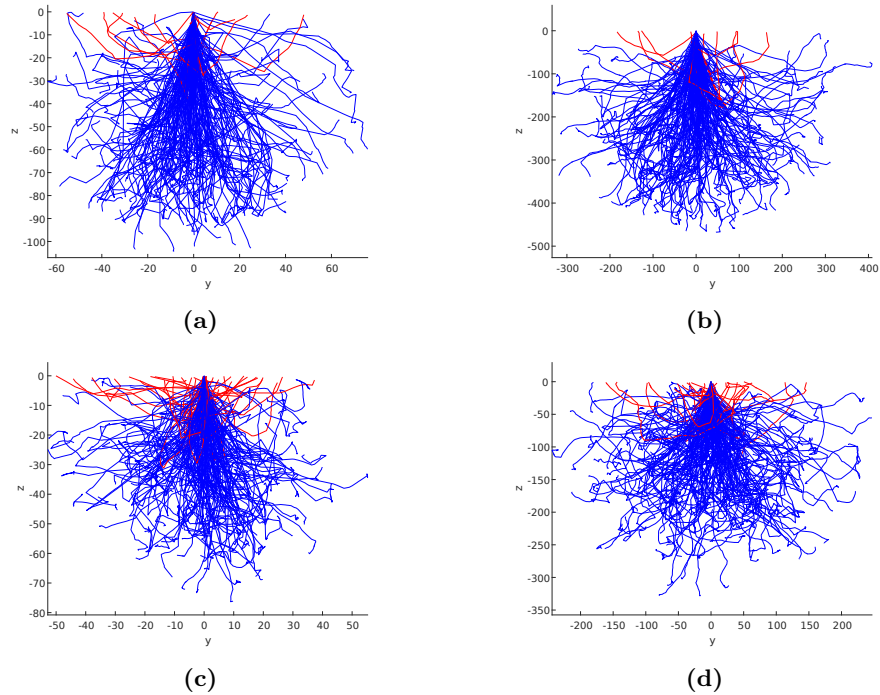
Material	E_0 (keV)	η	Contrast with cellulose
Cellulose	2	0.066	0
GCC		0.141	0.53
Pt/Pd		0.406	0.84
Cellulose	5	0.058	0
GCC		0.135	0.58
Pt/Pd		0.421	0.86

Table 4.2: 95th percentile for simulated BSE maximum depth distributions

Material	E_0 (keV)	Weighted arithmetic mean (nm)	95th percentile (nm)
Cellulose	2	18.3	36.3
GCC		12.1	24.8
Cellulose	5	88.0	169.4
GCC		55.5	108.0

Table 4.3: 95th percentile for BSE radius distribution

Material	E_0 (keV)	95th percentile (nm)
Cellulose	2	66.2
GCC		43.7
Cellulose	5	319.5
GCC		199.8

**Figure 13:** Simulated interaction volumes from flat surfaces with coordinates in nm. Blue trajectories are absorbed electrons, red are backscattered. a) cellulose at 2 keV, b) cellulose at 5 keV, c) calcium carbonate at 2 keV, d) calcium carbonate at 5 keV. Note the differences in scale.

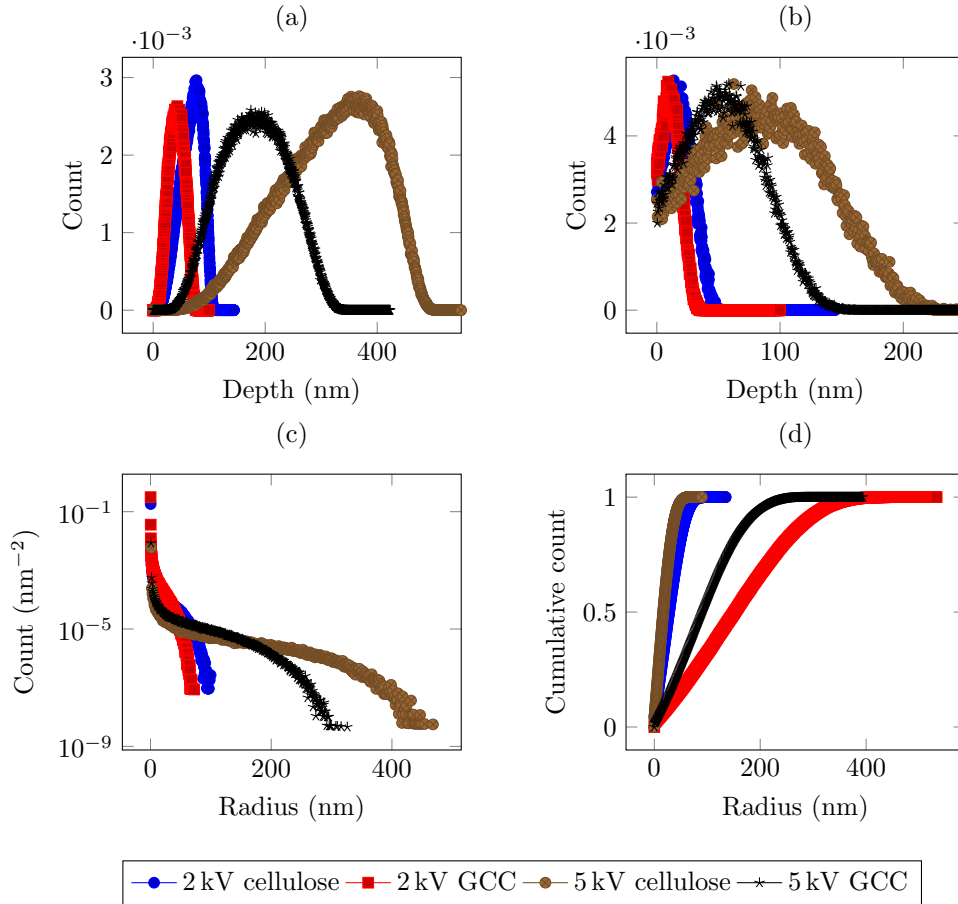


Figure 14: Collected distributions from simulation, flat surfaces. a) maximum depth reached by all electrons, b) maximum depth reached by BSE, c) radial distribution of BSE (distance from beam center where BSE are emitted), semilogarithmic to display the distribution tail. d) cumulative sum of radial distribution as function of radius, *i.e.* total fraction of electrons emitted within the radius.

The simulated interaction volume for a cellulose surface coated with 20 nm is shown in Figure 15. The simulated backscattering coefficient obtained was 0.396.

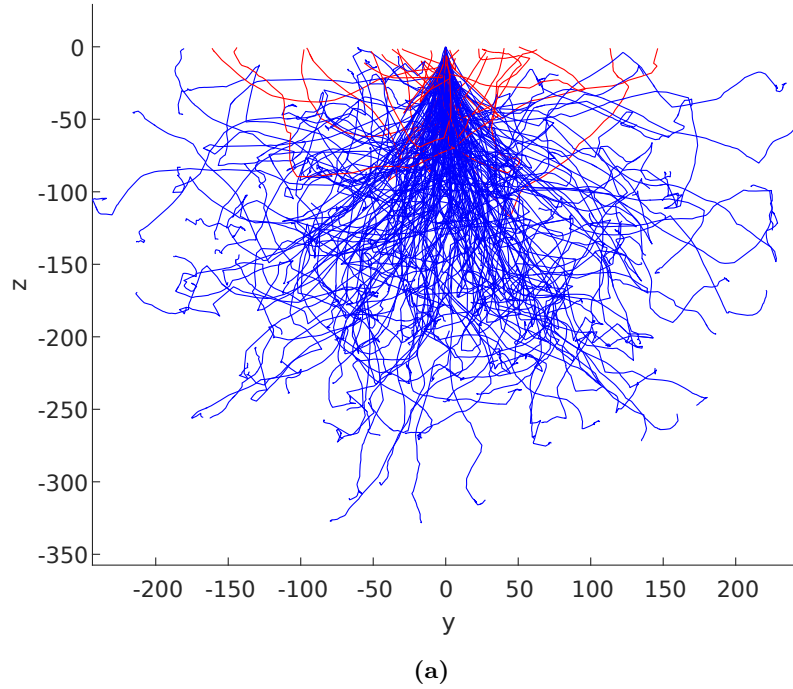


Figure 15: Simulated interaction volumes from cellulose surface coated with 20 nm Pt/Pd with coordinates in nm. Blue trajectories are absorbed electrons, red are backscattered.

Tilted Surfaces

The interaction volumes for surfaces tilted to 52° are shown in Figure 16, with backscattering coefficients shown in Table.

Table 4.4: Simulation of surfaces tilted to 52° , backscattering coefficients and contrast with cellulose, assuming constant detector efficiency

Material	E_0 (keV)	η	Contrast with cellulose
Cellulose	2	0.103	0
GCC		0.180	0.43
Cellulose	5	0.101	0
GCC		0.181	0.44

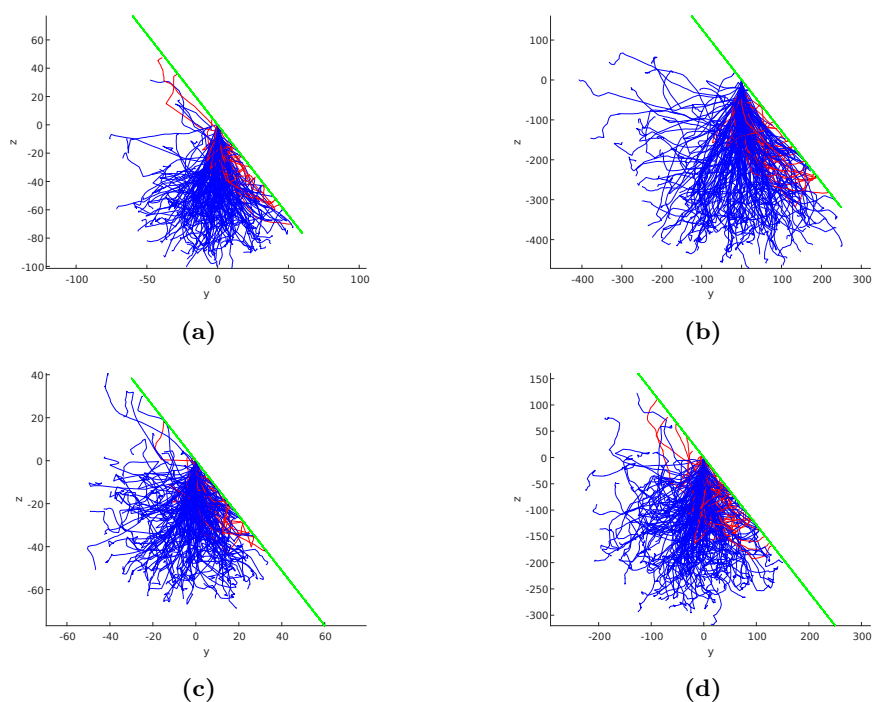


Figure 16: Simulated interaction volumes from surfaces tilted to 52° . Coordinates in nm. Blue trajectories are absorbed electrons, red are backscattered. The surface is marked by the green line. a) cellulose at 2 keV, b) cellulose at 5 keV, c) calcium carbonate at 2 keV, d) calcium carbonate at 5 keV. Note the difference in scale.

4.2 Sample Preparation

Figure 17 illustrates the embedding methods tried. 17a shows cylinder embedded samples after the epoxy disk is mounted, while 17b shows a block embedded paper sample sandwiched between glass cover slides. Figure 18 shows SEM images of the surface of the cylinder embedded sample. Cracks can be seen running through the sample (18a), and voids are apparent around features in 18b and 18c.

Figure 19 shows a cross section of the block embedded sample cut with a scalpel. Cracks are seen in the epoxy, and the paper is not cleanly cut. The SEM images in 20 show a cross sections that are ion milled after cutting. 20a is an overview of a block coated with 20 nm Pt/Pd, showing a smooth cross section in the middle and rough or incomplete milling on the right side. The lumens of two fibers can be seen as voids in the surface. The paper sample is barely visible. Figure 20b shows an ion milled surface coated with 5 nm Pt/Pd at 52° tilt. The paper sample is clearly visible. The image is taken near the edge of the milling area, and some roughness is observed on the surface, especially toward the upper right of the image. A void in the epoxy is visible in the lumen of a fiber.

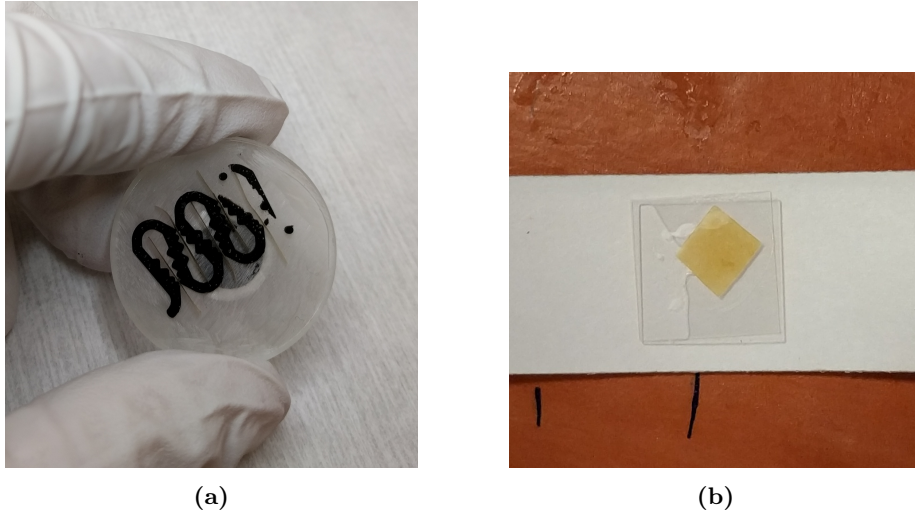


Figure 17: Paper samples embedded in epoxy. a) cylinder geometry, with several paper samples held in plastic clip. The top surface is mechanically ground and polished using ethanol as lubricant. b) block embedded paper sample sandwiched between glass cover slides.

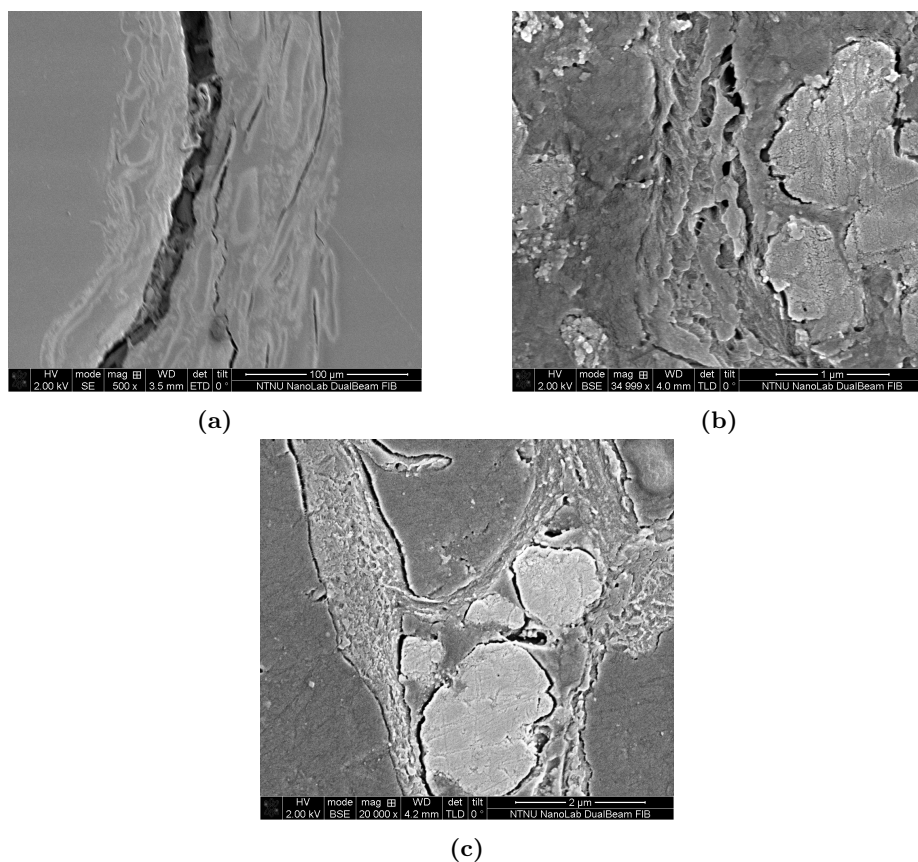


Figure 18: 2 kV images of embedded samples mechanically ground and polished with ethanol as lubricant. a) SE overview showing a paper sample running vertically, with several cracks running through the structure. b) and c) are closeup BSE micrographs of cellulose and GCC components. Voids are visible around the features.

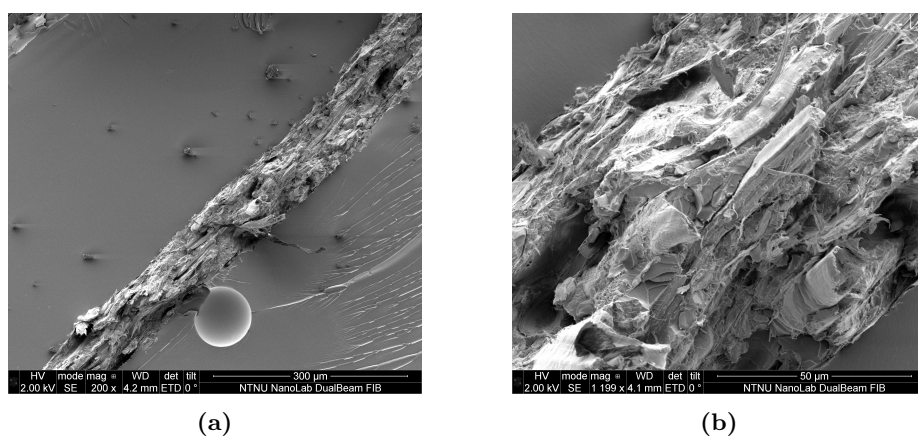


Figure 19: 2 kV SE images showing cross section of epoxy block cut with scalpel. a) overview showing the paper running diagonally, b) closeup of the paper sample.

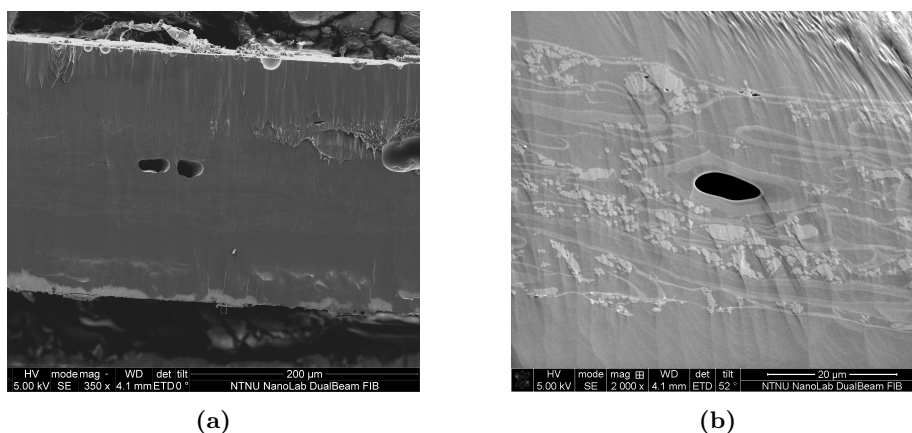


Figure 20: 5 kV SE images showing cross section of epoxy block polished by ion milling. a) overview at 0° tilt with 20 nm Pt/Pd coating. Milling artifacts are seen near the face of the block and at the edge of the milled area. The paper is faint, but discernable in the middle of the block. Two pores not filled by epoxy are visible. b) closeup of surface topography at 52° tilt with 5 nm Pt/Pd coating. A large pore is visible in the lumen of a fiber and small near GCC clusters.

SEM of UA-Stained Samples

Comparison BSE micrographs of stained and unstained samples (uncoated) recorded using the same imaging parameters are shown in figures 21 (at 5 kV) and 22 (at 2 kV). The WD is altered as the samples were not mounted at the exact same height, and refocusing was necessary. The stained sample shows better contrast between cellulose and epoxy. Charging artifacts are apparent in the images of the unstained samples, but not in the stained. The 5 kV images show improved contrast between cellulose and epoxy with staining. The difference is also seen at the lower voltage, where cellulose and epoxy are apparently indistinguishable for the unstained sample.

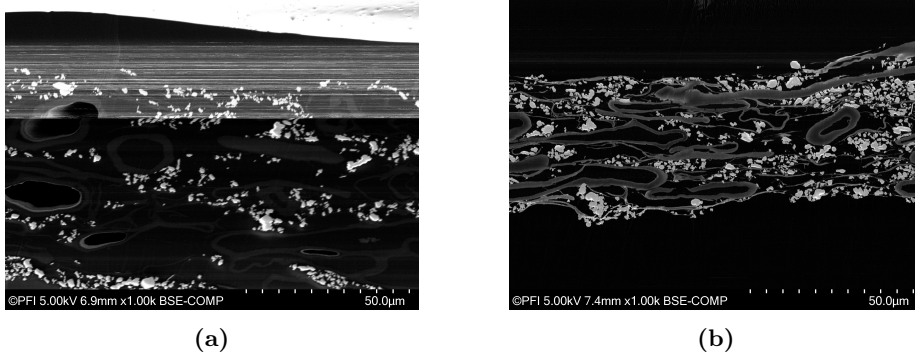


Figure 21: 5 kV BSE images of 35-3 (furnish) a) unstained b) UA-stained recorded using the same instrument parameters. The bright scan lines in a) are a charging artifact. The stained sample shows improved contrast between cellulose and epoxy. In b), the edges of massive cellulose structures appear brighter than the interior.

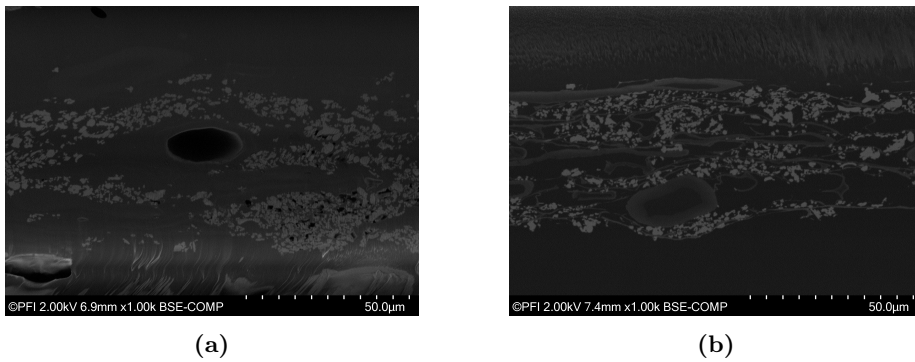


Figure 22: 2 kV BSE images of 35-3 (furnish) a) unstained b) UA-stained recorded using the same instrument parameters. Distortion is visible in the lower region of a). In a), cellulose is indistinguishable from the epoxy background. In b), the distinct phases are apparent.

4.3 FIB/SEM

FIB Electron Beam Current

Measurements of the electron beam current in the FIB by use of a Faraday cup are shown in Table 4.5. The nominal beam current I_{nom} is the current set in the instrument, while I_B is the measured beam current. For ease of repeatability, the nominal beam setting is used throughout the results unless otherwise noted. In calculations, the measured values are used for the beam current.

Detector Efficiency Estimation

BSE images of the epoxy surface coated with 20 nm of Pt/Pd are shown in Figure 23, taken at a) 0.17 nA, b) 0.34 nA with dwell time $\tau = 10 \mu\text{s}$. The marked rectangles are chosen as relatively featureless areas with little variation

Table 4.5: Measured electron beam current I_B compared to the nominal beam current I_{nom} in the FIB at 2 and 5 kV acceleration voltage. The nominal beam current is the current displayed by the instrument.

V_0	I_{nom} (nA)	I_B (nA)
2 kV	0.34 nA	0.232
	0.69	0.305
	1.4	0.635
	2.7	3.13
5 kV	43	0.0517
	86	0.101
	0.17	0.204
	0.34	0.405
	0.69	0.786
	2.7	3.170

Table 4.6: Mean intensity S and standard deviation SD for DQE estimation

I_{nom}	0.17 nA	0.34 nA
S	81.406	118.507
SD	18.746	17.758

in intensity, and their histograms are shown in c) and d). The mean and standard deviation of these histograms is shown in Table 4.6. The intensity mean is plotted against the measured beam current (Table 4.5) to find the offset intensity value of 43.8440. Using the values for 0.34 nA, the experimental SNR is calculated to be 4.2045. The theoretical SNR is calculated from Equation 2.5 using the simulated η of 0.39565 for Pt/Pd on cellulose to be 98.0404, giving a detector quantum efficiency of 0.0018.

Calculations of Current and Beam Diameter

Using the estimated DQE and the simulated backscattering coefficients, the minimum beam current necessary to fulfill the Rose criterion is calculated from 2.7. The result is shown in table 4.7 for dwell times of 10, 30 and 100 μ s.

From Equation 2.2, the known WD of 4.1 mm and range of aperture diameters, the minimum diameter d_0 of the FIB-SEM electron beam can be estimated for the measured beam currents. The brightness of the FEG is unknown, so the value of 1×10^8 A cm⁻² sr given by Goldstein [23] is used.

Table 4.7: Minimum beam current as function of dwell time to fulfill the Rose criterion for 2 kV BSE imaging of cellulose/GCC

τ (μ s)	I_B (nA)
10	11.8
30	3.9
100	1.18

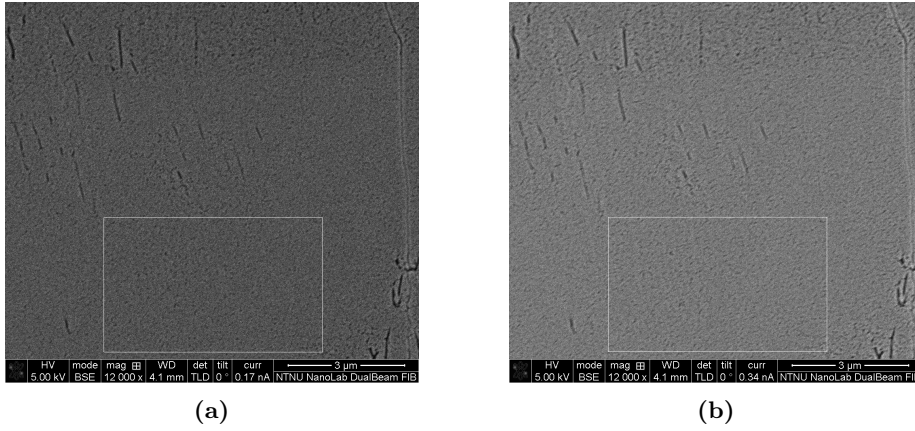


Figure 23: 5 kV BSE micrographs of Pt/Pd coated epoxy surface at a) 0.17 nA, b) 0.34 nA. The brightness and contrast has not been altered between images. The marked rectangles are used for the analysis.

Table 4.8: Estimated beam diameter d_0 at 2 kV ignoring aberrations

I_{nom} (nA)	d_0 (nm)
0.34	1.3
0.69	1.5
1.4	2.2
2.7	4.8

Imaging Parameter Variation

Figures 24-27 show images taken in the FIB-SEM of the same surface, varying the voltage and current. The dwell time is constant at 10 μ s. 24 shows 2 kV BSE images taken at beam currents from 0.34 nA to 2.8 nA. Figure 25 shows 5 kV images taken at beam currents from 86 pA to 0.69 nA. White artifacts in GCC particles are visible for all currents. The raw images are included with the attachments.

Figure 26 shows 2 kV SE images taken at 21 pA to 1.4 nA, and 27 shows 5 kV images at currents from 21 pA to 0.34 nA. White artifacts are visible in GCC particles.

Figure 28 shows a comparison of the variations in phase contrast for BSE and SE imaging modes. The raw images are manually segmented into the separate phases as shown by the white outline in the images. The histograms of the separate phases are shown below, where the blue plot is from the raw image, the red after application of a 2 pixel Gaussian blur. For the BSE image, the peaks are sharper after filtering, whereas the SE image is less affected.

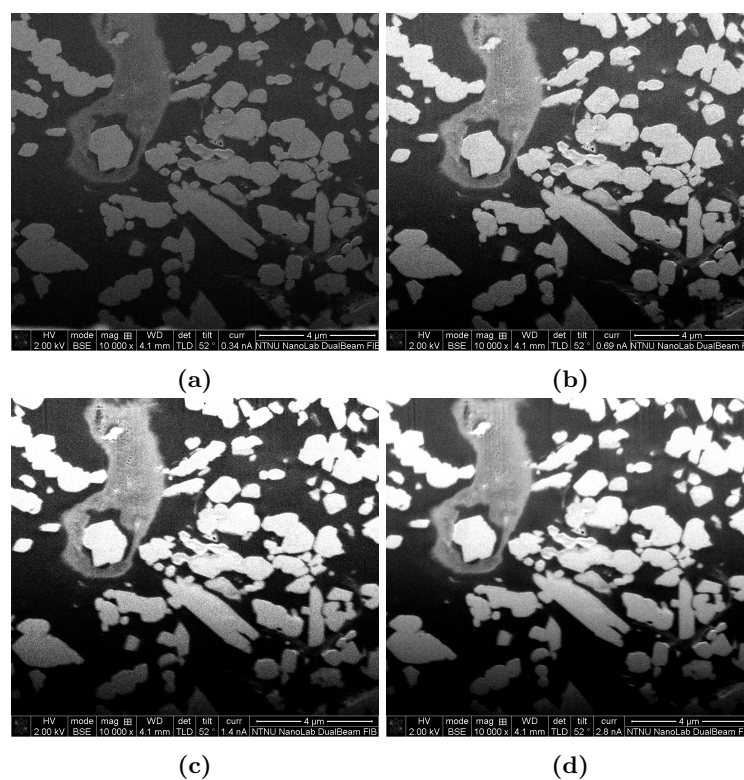


Figure 24: BSE imaging at 2 kV with 10 μ s dwell time, a) 0.34 nA, b) 0.69 nA, c) 1.4 nA, d) 2.8 nA

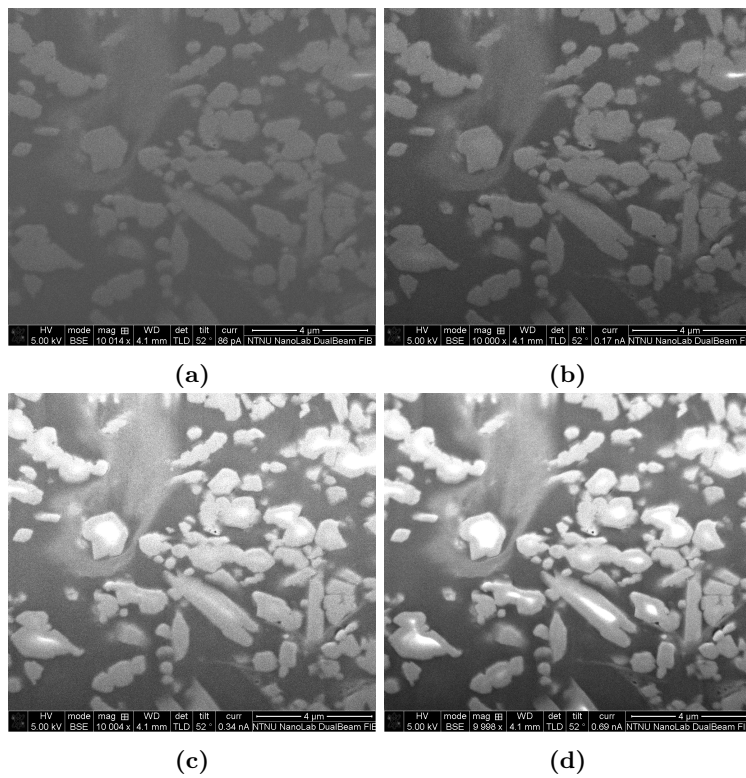


Figure 25: BSE imaging at 5 kV with 10 μ s dwell time, a) 86 pA, b) 0.17 nA, c) 0.34 nA, d) 0.69 nA

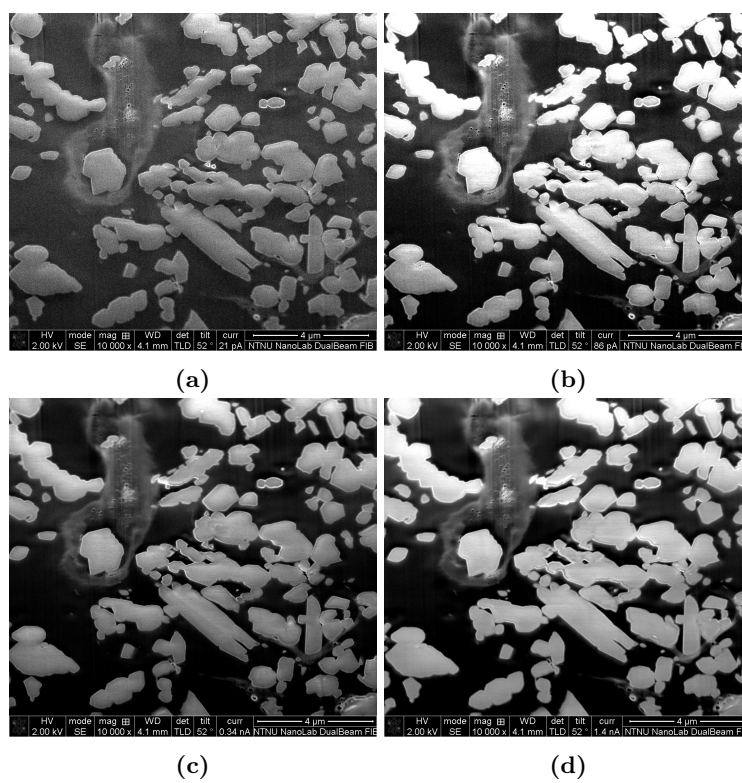


Figure 26: SE imaging at 2 kV with 10 μs dwell time, a) 21 pA, b) 86 pA, c) 0.34 nA, d) 1.4 nA

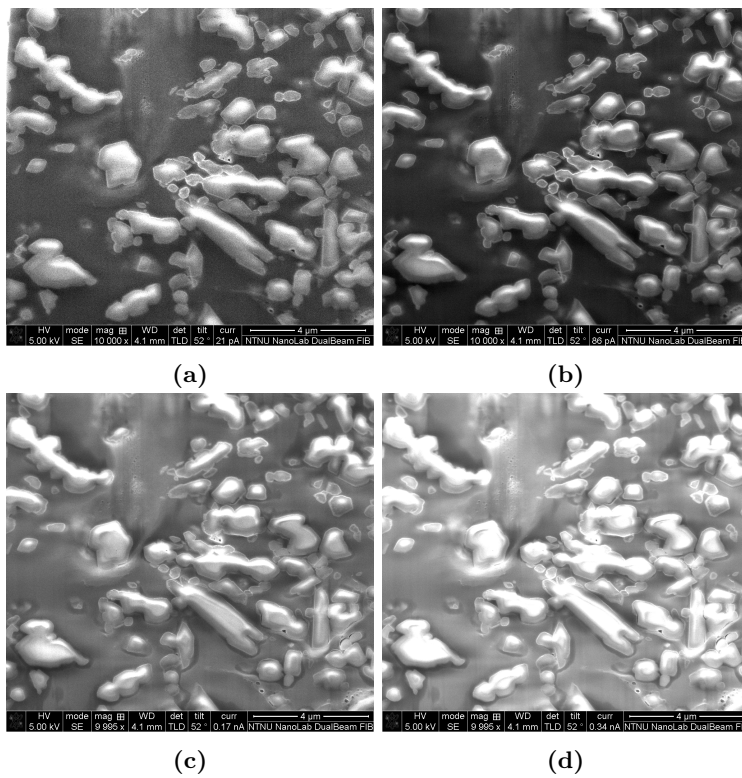


Figure 27: SE imaging at 5 kV with 10 μs dwell time, a) 21 pA, b) 86 pA, c) 0.17 nA, d) 0.34 nA

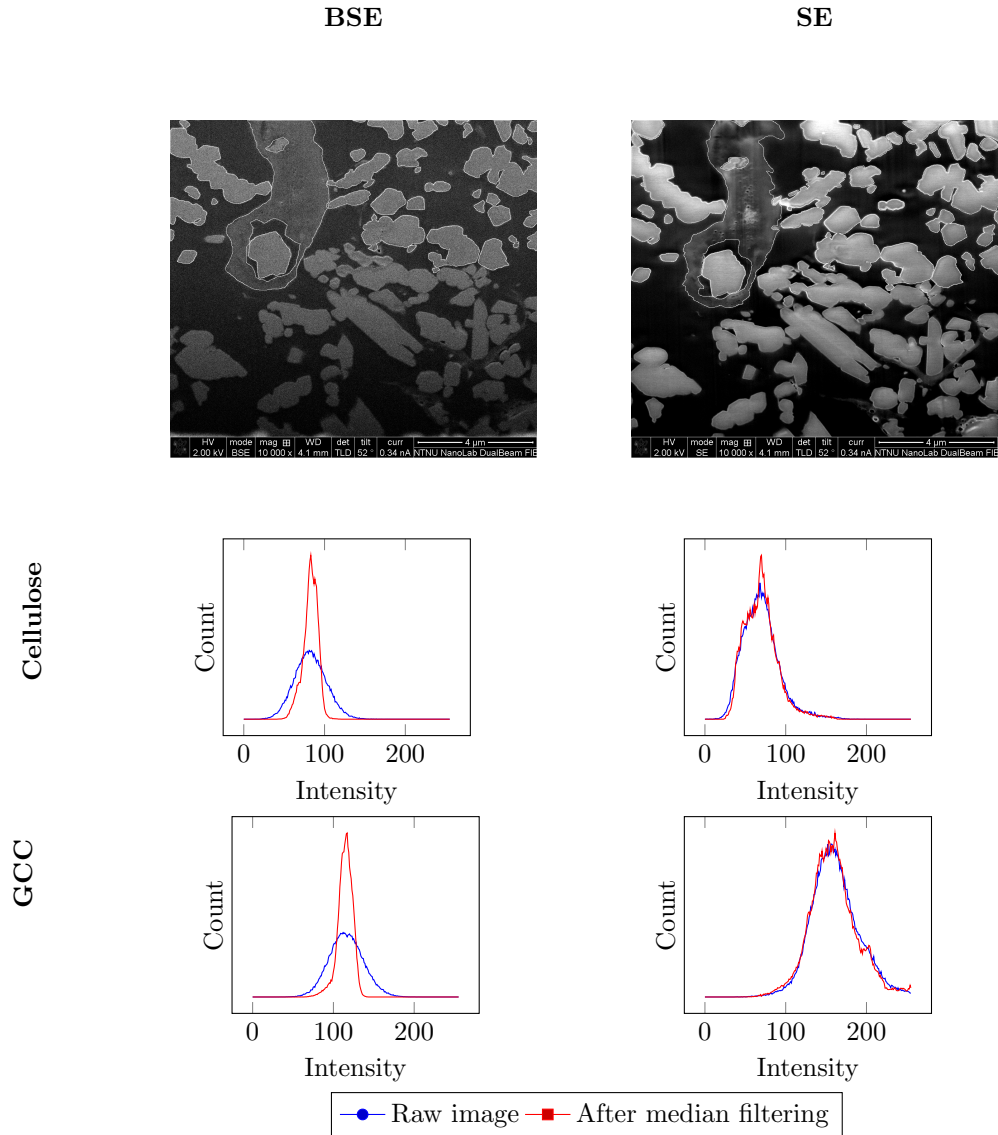


Figure 28: Histograms from separate phases in SE/BSE, showing variation of intensity within a phase. The histograms show count (in arbitrary units) as function of intensity, and are taken from the separate phases based on the manual segmentation marked in white on the images in the top row. Blue line is the histogram in the raw image, red is after application of a 2px median filter. For BSE, the variance is reduced significantly by filtering, while it is relatively unaffected for SE.

4.3.1 FIB Tomography

The raw and processed image stacks are included in the attachments. The acquisition times of the 6 tomography experiments performed are calculated and listed in Table 4.9. The time for area preparation and experiment set-up is not included, but ranged from around three to eight hours, depending on the size of the area. Several times, the set-up had to be restarted due to failure of the software to recognize the fiducial mark. The results of the experiments follow in more detail. Note that the SEM images are taken with the sample tilted to 52° , and are therefore subject to foreshortening in the y direction. The raw images shown here must be stretched by $1/\sin(52)$ to correct for this.

Table 4.9: List of FIB tomography experiments with main parameters and results. Total acquisition time is longer than milling+imaging time due to 15 seconds added per image to turn immersion mode on and off.

Experiment	ASV1	ASV2	ASV3	ASV4	ASV5	ASV6
τ (μs)	10	30	30	30	30	30
Milling current (nA)	0.46	0.28	0.28	0.093	0.093	0.093
Slice thickness (nm)	38.6	16	16	15	20	20
xz -area (μm^2)	8.71 x3.86	11.71 x1.8	22 x3.47	24 x3.63	19.73 x4.96	15 x0.72
Nominal depth (μm)	3	4	5	5	4	5
Ion dose ($\text{nC } \mu\text{m}^{-2}$)	8.5	8.12	10.15	7.53	6.02	7.53
Milling time (s)	621.3	611.3	2768.9	7053.9	6334.6	874.5
Image resolution (px)	2048 x 1768	1024 x884	1024 x884	1024 x884	1024 x884	1024 x884
Total imaging time (s)	3620	3068	5893	6572	6735	978
Total acquisition time (s)	5741	5374	11916	17256	16790	2393
Acquisition rate (10^4px/second)	6.3	1.9	1.6	1.3	1.3	1.4

Figures 29a-29c show slices 14, 45 and 100 of experiment ASV1. The field of view is wider than the block, the dark middle section is the block cross section. No cellulose can be discerned in the images. Vertical striations are visible toward the lower edge of the images. In 29b and 29c, enclosed pores in the GCC are seen to saturate in intensity, which is likely a charging artifact. Figures 29d and 29e are SIM alignment images showing the area from above before and after tomography. After alignment and cropping, a 789x1557 pixel image stack of 89 slices was preserved. A slice of the image stack after alignment and cropping is illustrated in Figure 30a with the segmentation marked as a red outline. Volume renderings of reconstructed volume based on this segmentation are shown in figures 30b and 30c. From the original horizontal field of view of 15.95 μm and resolution of 2048x1768 pixels, the voxel resolution is 7.8x7.8x38.6 nm^3 . The reconstructed volume is thus approximately 6x12x3 μm^3 .

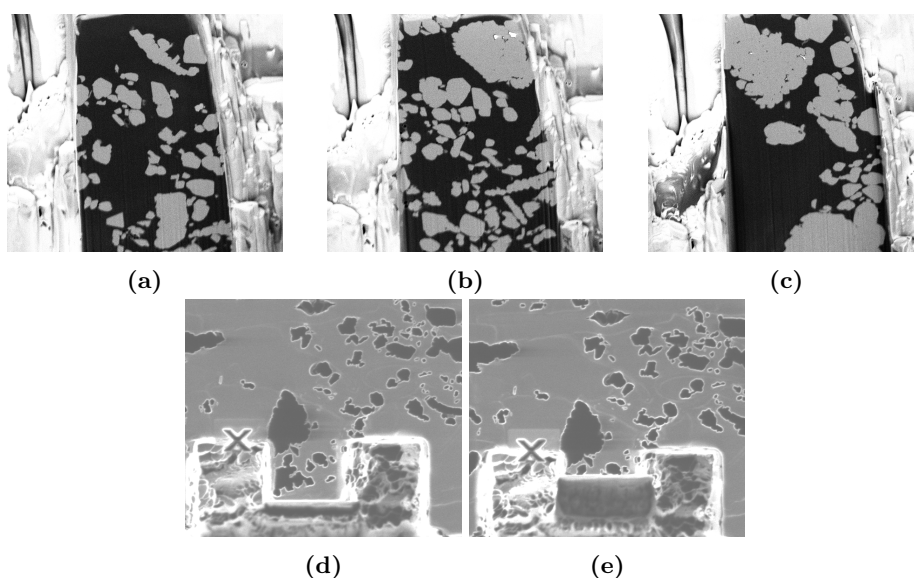
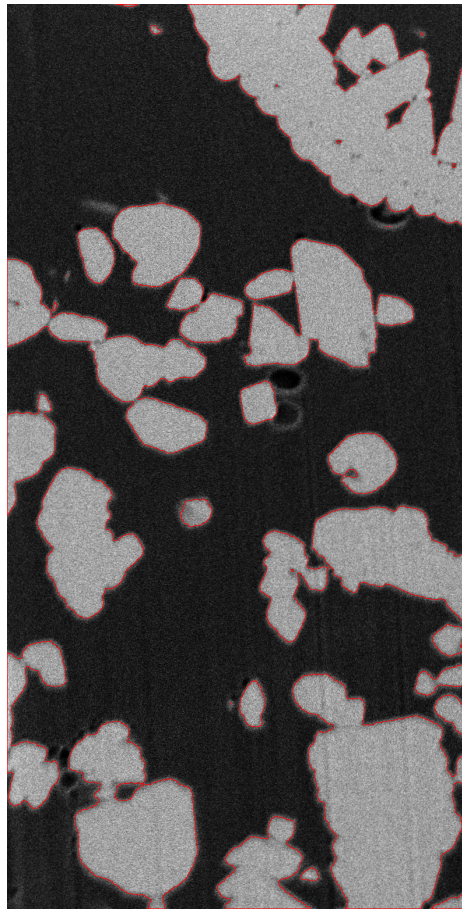
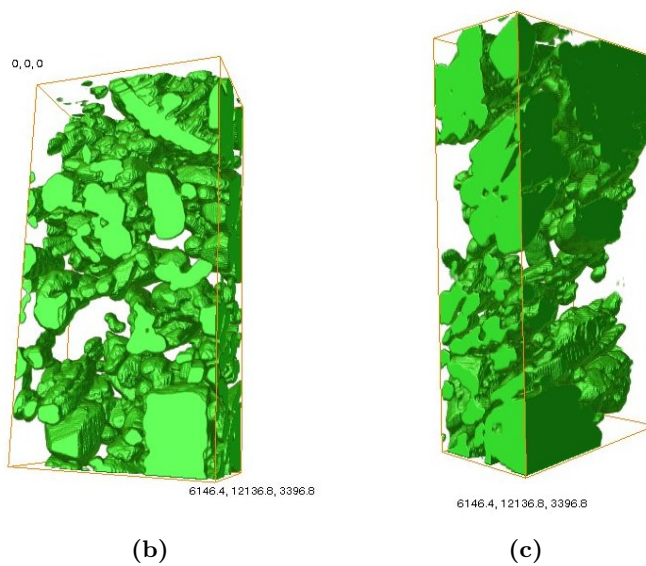


Figure 29: ASV1 - frames a) 14, b) 45 and c) 100 of FIB tomography of unstained 35-3 furnish sample. 2 kV BSE images, 0.69 nA with 10 μs dwell time. Horizontal field of view is 15.95 μm . Only GCC is visible. In b), pores in GCC are seen to saturate in intensity. Faint vertical streaking is apparent on the cross sections. d) and e) show the SIM alignment images from the d) 14th e) 100th slice.



(a)



(b)

(c)

Figure 30: ASV1: a) alignment and cropping of the stack. The red outline shows the result of segmentation. b) and c) show the reconstructed volume with coordinates in nanometres. The voxel resolution is $7.8 \times 7.8 \times 38.6 \text{ nm}^3$.

Experiment ASV2 ran successfully, and slices 1, 23 and 95 are shown in figures 31a-31c. Each $11.71\ \mu\text{m}$ by $16\ \text{nm}$ slice was milled to a nominal depth $4\ \mu\text{m}$ at $0.28\ \text{nA}$ ion beam current. The sample is stained with uranyl acetate, and the three phases can be distinguished. The overhead SIM alignment images in 31d-31e show the area before and after tomography. A milled rectangle can be seen in the bottom of the front trench, caused by the software initially not recognizing the fiducial mark. Two volume renderings of the reconstructed volume are shown in Figure 32 with coordinates in nanometres. The voxel size is $13 \times 13 \times 16\ \text{nm}^3$, and the total volume approximately $10.2 \times 13.4 \times 1.7\ \mu\text{m}^3$. Some striations are visible in the lower part of the SEM images, and vertical streaks with large intensity variations are seen in 31a and 31b. These are erroneously segmented as cellulose, and can be recognized in the reconstructed volume.

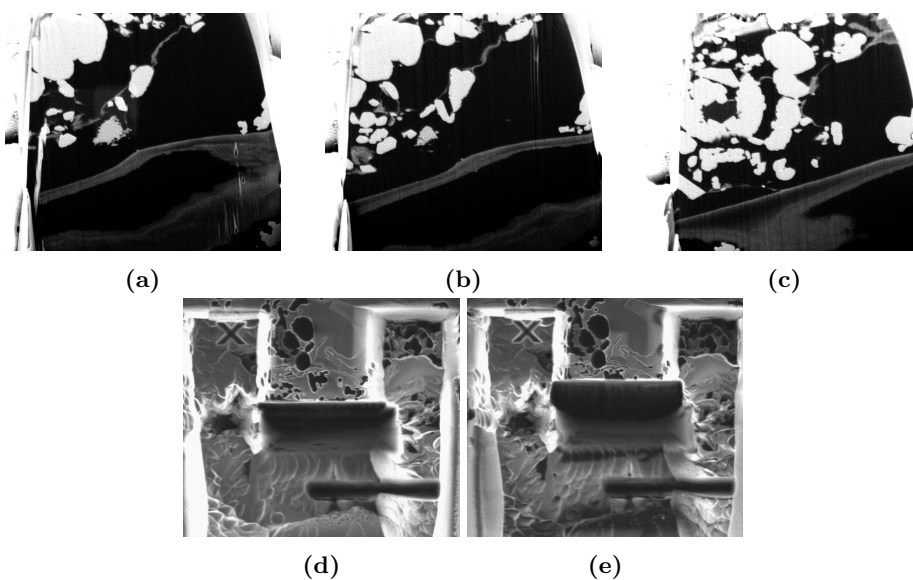


Figure 31: ASV2 - frames a) 1, b) 23 and c) 95 of FIB tomography of stained 35-3 furnish sample. $2\ \text{kV}$ BSE imaging at $1.4\ \text{nA}$ with $30\ \mu\text{s}$ dwell time. Horizontal field of view is $12.80\ \mu\text{m}$. $16\ \text{nm}$ slices were milled with $0.28\ \text{nA}$ ion beam current. d) and e) show the SIM alignment images from the d) first e) 114th slice.

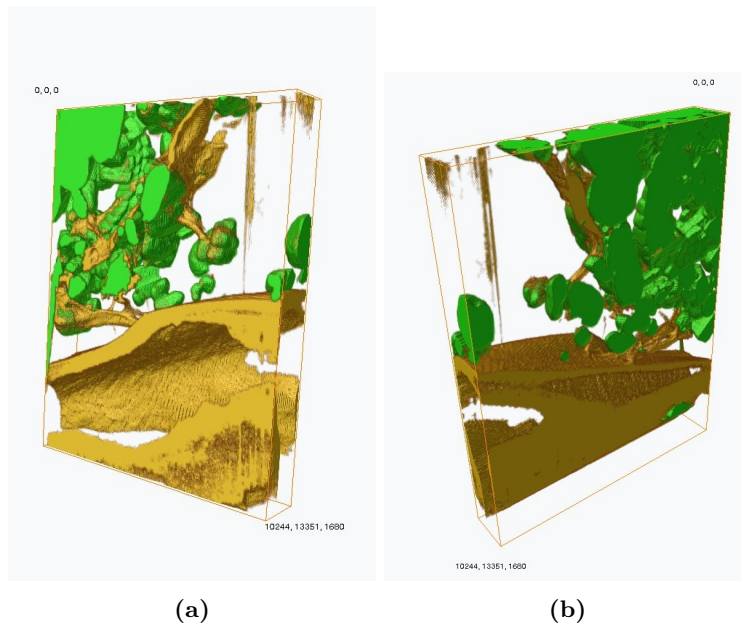


Figure 32: ASV2 - volume rendering of reconstructed volume. Coordinates in nanometers. Voxel size is $13 \times 13 \times 16 \text{ nm}^3$. Vertical streaks are milling artifacts erroneously identified as cellulose

Experiment ASV3 failed due to the software not aligning the slices correctly in the x direction. This was not recognized during set-up, and the experiment was left to run unattended to completion. The SIM alignment image in Figure 33d shows that the milled area is not rectangular, and that the milling position shifts toward the left for each slice. In addition, the slicing started behind the face of the block, leaving it standing as a wall. Redeposited material can be seen on the rear face. The SEM images in figures 33a-33c show the same drift in the x -direction, and the milling starting behind the block face, which then obscures the further imaging. The apparent drift in y direction is caused by the automatic readjustment to track the milled section. The front face of the block has severe striations after rough milling with 6.5 nA ion beam current. The SIM image shows two milled fiducial marks. This was done because the software failed to recognize the first. Both fiducial marks are placed on the edges of milled trenches.

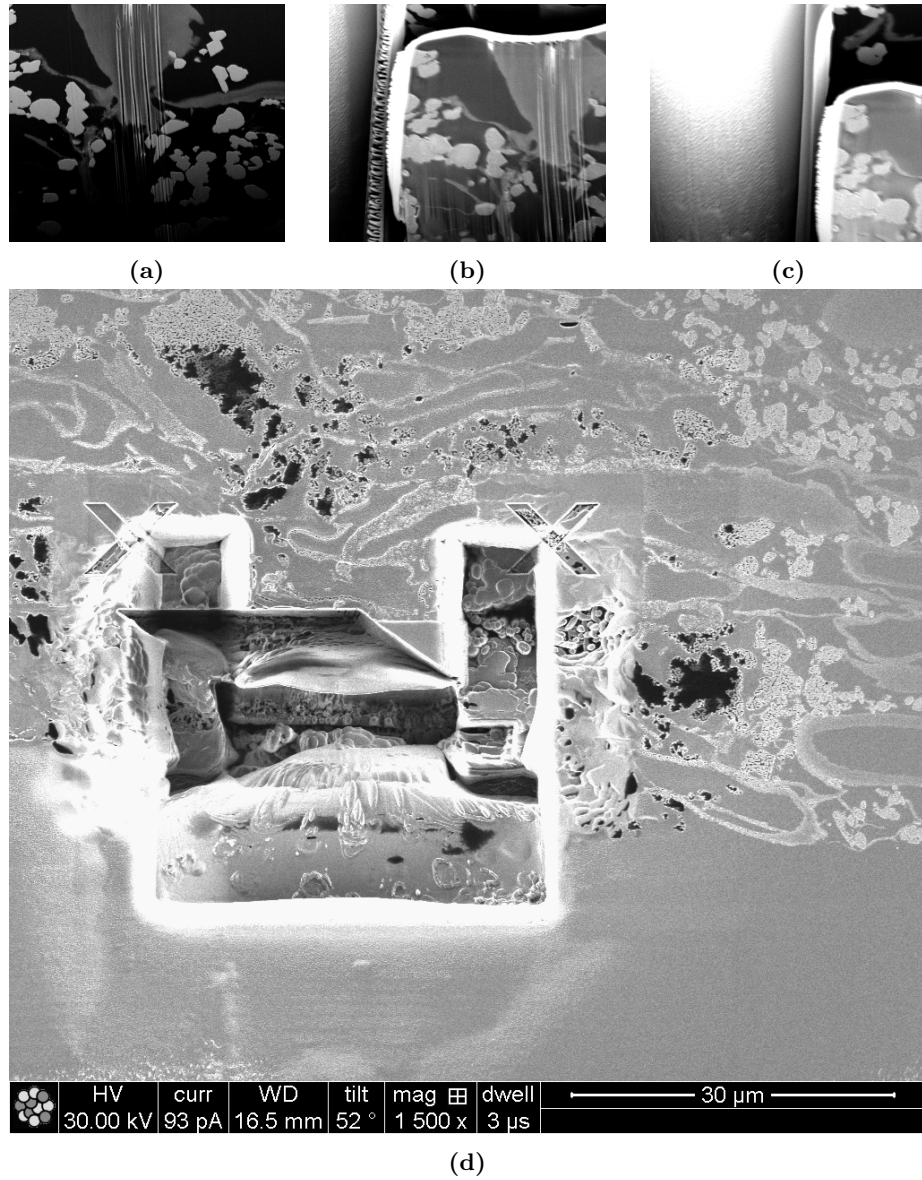


Figure 33: ASV3 - frames a) 1, b) 73 and c) 217 of failed FIB tomography. Horizontal field of view is $12.80\ \mu\text{m}$. The region of interest disappears from view because of drift in the x direction, and the face of the block is not milled, obscuring the milled sections. d) shows a SIM image of the area after tomography, showing how the milling position has drifted in the x direction. Redeposited material can be seen piled on the rear of the front face. Two fiducial marks were milled, as the first was not recognized by the software. Both are placed on milled trench edges.

Experiment ASV4 ran successfully, but the first part of the image stack is obscured by redeposited material on the block face (figures 35a and 35b). The front face is not milled away entirely before approximately frame 120. In part, this may be due to poor alignment of the milling area with the block face, but the gradual milling of the front face indicates that it was not parallel to the ion beam, but at an angle. Slices 120 to 240 show entire cross sections (figures 35c-35e), though apparent drift in the x and y directions is visible as the block edges coming into the field of view. The SIM images in Figure 36a show corresponding drift in the x and y directions. Degradation of the reference mark and surrounding surface can be seen by comparing the first and last alignment images.

After alignment and cropping, a 777 by 744 pixel stack with 127 slices was left, with voxel resolution of $13 \times 13 \times 15 \text{ nm}^3$. The SEM images appear darker near the bottom, and were treated by the background subtraction routine described in 3.5, illustrated in Figure 37. Volume renderings of the approximately $10 \times 9.6 \times 1.9 \mu\text{m}^3$ volume are shown in Figure 38.

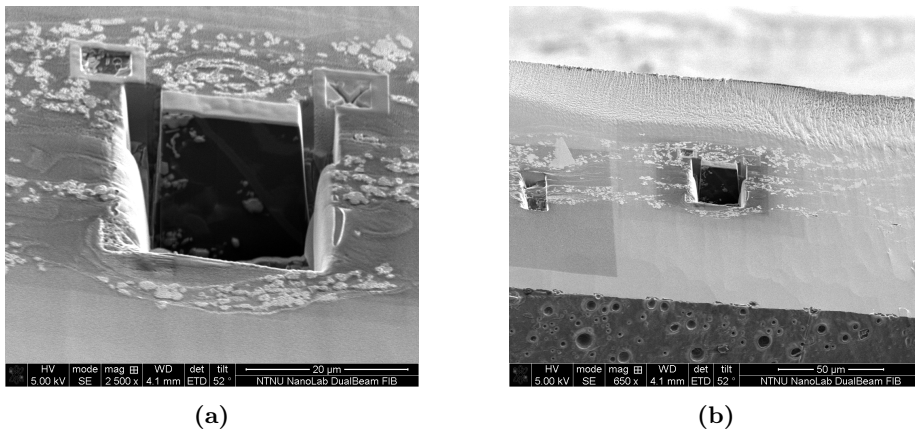


Figure 34: ASV4. a) 5 kV SE image showing the prepared area after tomography. On the block to be imaged, a 500 nm pad of Pt has been deposited. Front and side trenches have been milled, as was a fiducial mark on a deposited Pt pad. b) 55 kV SE image showing the tomography area on the whole epoxy block. The block is tilted from the horizontal, *i.e.* not mounted level

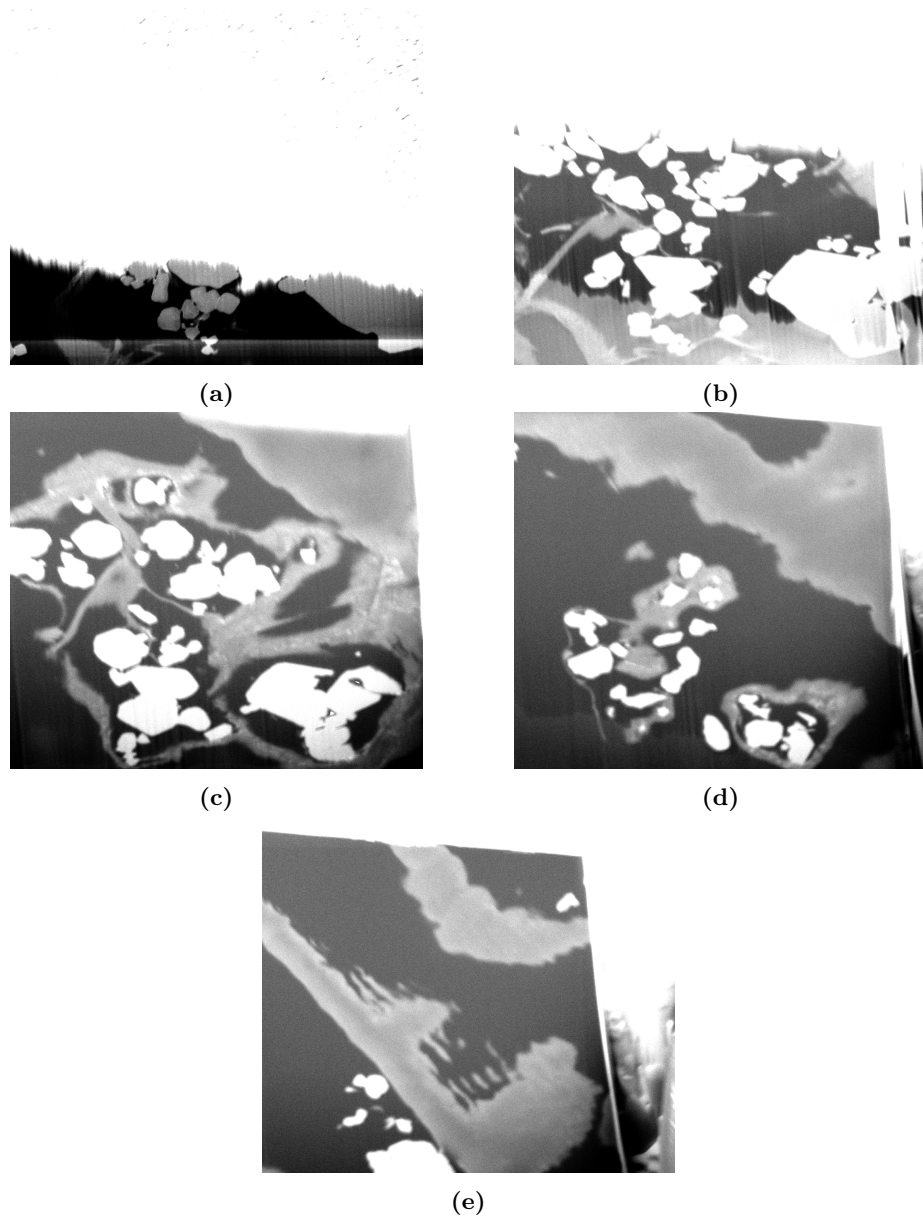


Figure 35: ASV4. a) - e) frames 64,88,117,159,240 from tomography. 2 kV, 1.4 nA BSE images taken with $30\ \mu\text{s}$ dwell time. 240 15 nmslices were milled using 93 pA ion beam current. The first two images are obscured by redeposited material on the block face, saturating in intensity. c)-e) are frames after the milling area has reached the block proper. Apparent drift in the x and y direction can be seen as the edges of the block coming into view.

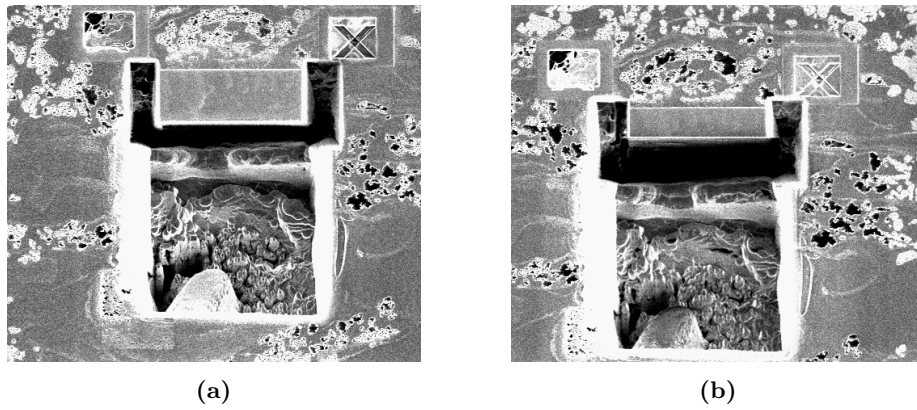


Figure 36: ASV4. SIM alignment images of a) slice 1 and b) 234. Drift in the y direction is apparent. The reference mark and surrounding area is seen to be damaged after the repeated imaging with milling current.

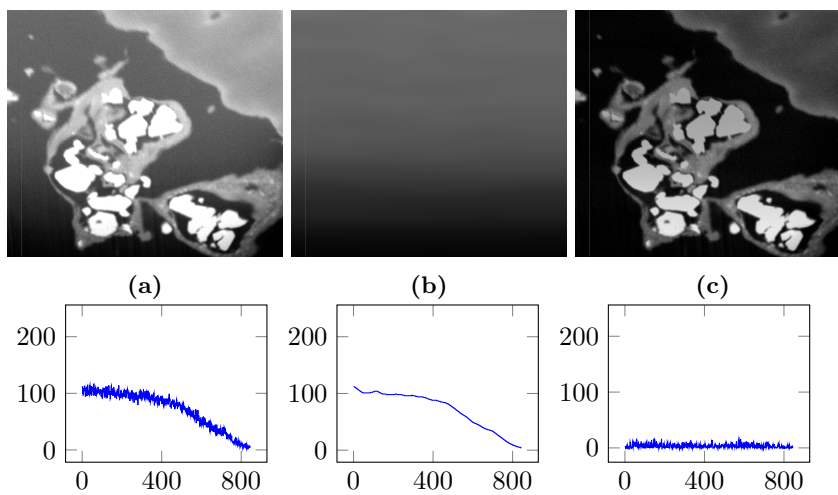


Figure 37: Background levelling of the image stack. a) is the raw image, b) the false background, c) the result of subtracting the background. Below the images are intensity profiles along the red line in the images (containing only background), showing intensity as function of y position.

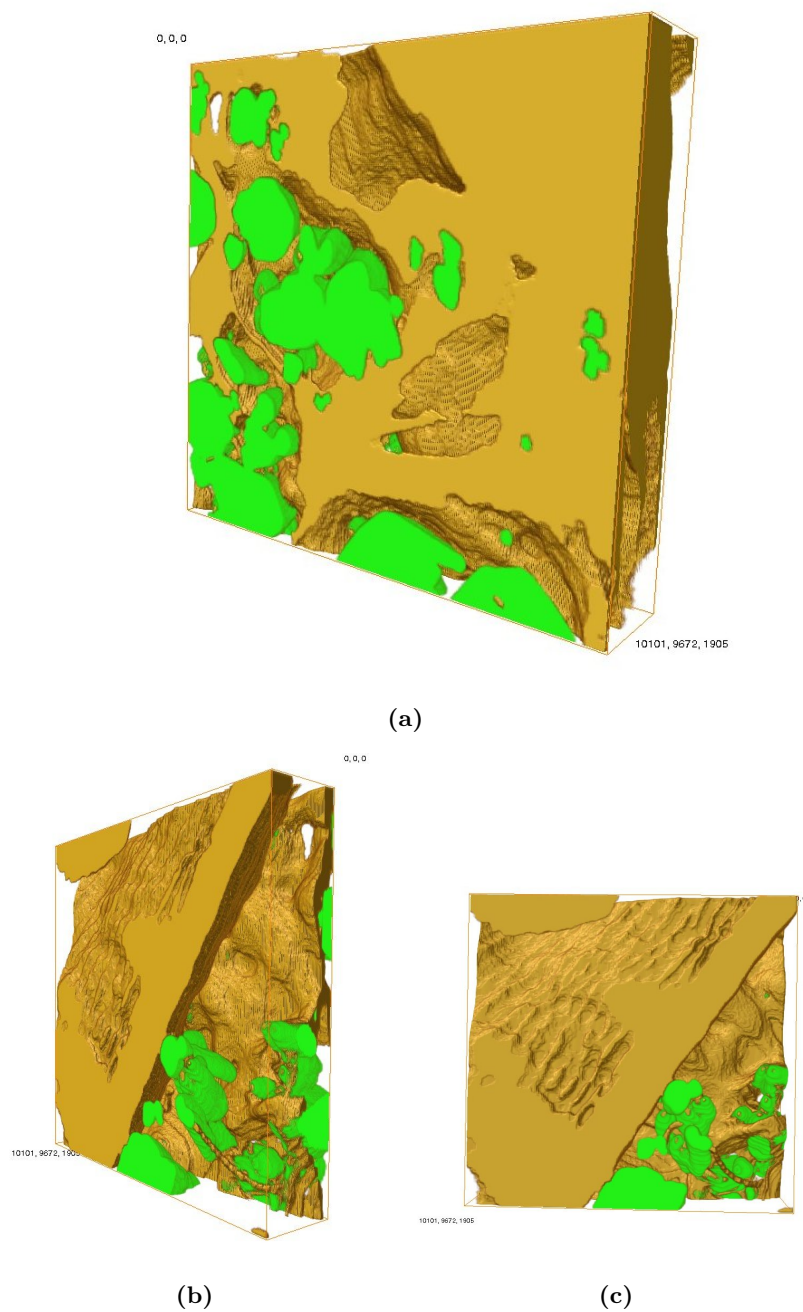


Figure 38: ASV4-reconstruction volume renderings with coordinates in nanometers. Voxel size is $13 \times 13 \times 15 \text{ nm}^3$.

Figure 39 shows SEM (39a-39f) and SIM (39g and 39h) images of experiment ASV5. 39a shows a SEM image during milling of the front face of the block. 39b-39f are tomography slices. The imaged region is composed almost entirely of massive cellulose, and was therefore not processed further as little structure was imaged. The images show severe artifacts: vertical striations are prevalent, and vertical rows of pores can be seen in the cellulose phase. Some drift in the x -direction is visible in the SEM images and SIM images.

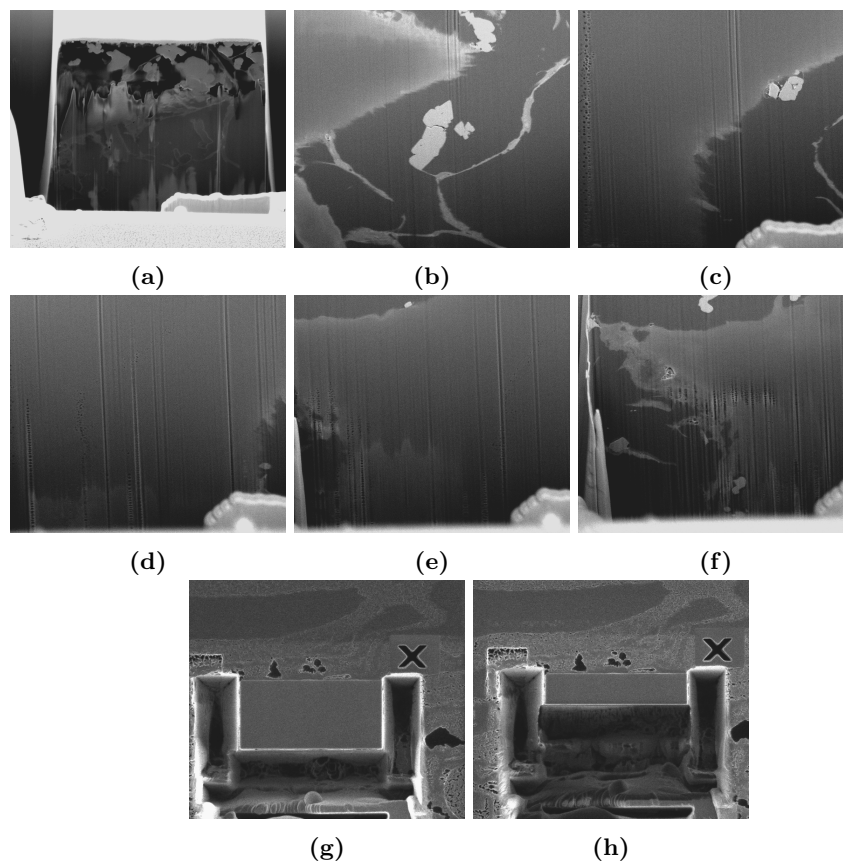


Figure 39: ASV5. a) Milling of the front block face. b) - f) frames 48, 98, 148, 198 and 248 of tomography, 2 kV images taken at 0.69 nA beam current and 30 μ s dwell time. 248 20 nm slices were milled with 93 pA ion beam current. The imaged region is almost entirely composed of massive cellulose, and little structure was imaged. Severe milling artifacts are visible in all images.

Experiment ASV6 failed after 36 slices because the reference mark was not entirely within the SIM image. This is shown in the SIM images (figures 40e and 40f). The SE images in figures 40a-40c are frames 6,10 and 12 from the tomography procedure, recorded before the final magnification and imaging parameters were set. They demonstrate the milling of the front face of the block. The face, covered in redeposited material, is uncovered from the bottom as the milling area is moved, indicating that the face is at an angle to the beam. However, milling can be observed along the top of the block. Figure 40d is a BSE image from the procedure with the chosen imaging parameters of 2 kV, 1.4 nA with 30 μ s dwell time.

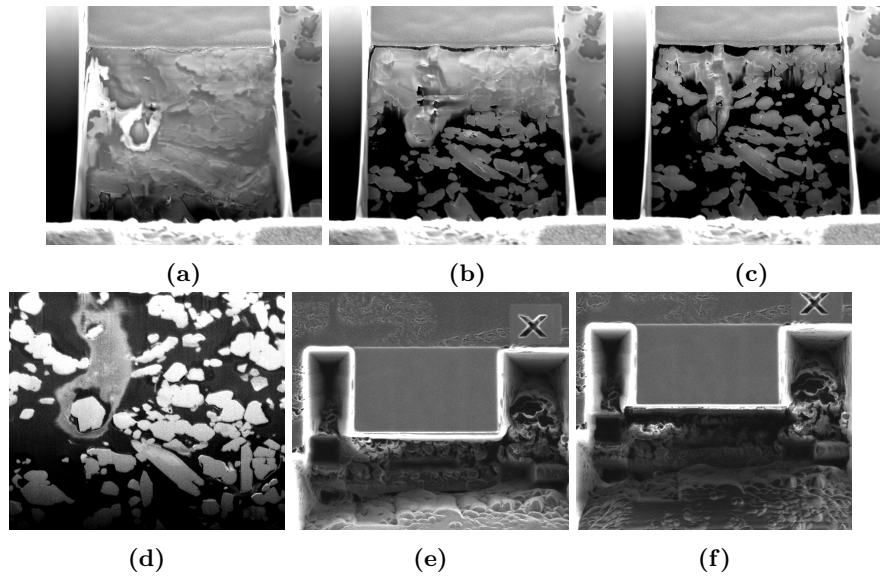


Figure 40: ASV6. a) - c) SE images, frames 6, 10,12 showing milling at the front face of the block. In a), the face is covered by redeposited material, and milling of sequential slices removes the deposited layer from the bottom, though milling can also be seen along the top of the block. d) is a BSE image from the tomography procedure. e) and f) are SIM images of frames 1 and 36, where the procedure stopped as the reference mark came out of the ion beam field of view

5

Discussion

5.1 Monte Carlo Simulations

The simulated backscattering coefficients in Table 4.1 follow the trend described in the literature of lower material contrast for lower acceleration voltage in the 1-5 keV range. The simulated interaction volumes shown in Figure 13 and the depth distributions in Figure 14 give an indication of the penetration depth in the different materials. Calcium carbonate has higher stopping power than cellulose, and electrons penetrate a shorter distance.

The spatial extent of the interaction volume is one of the fundamental limits on the resolution achievable in SEM. For materials with low mean atomic number, such as cellulose, the beam spreads out considerably. Figure 14 and Table 4.3 show that for cellulose, a 1 nm beam of 2 keV electrons gives contributing volume is tens of nm in depth and radius. Though the distributions show that the majority of BSE are emitted from a smaller volume, the tails of the distributions do contribute significantly as demonstrated by the cumulative sum. The emitted signal will then carry information about a weighted average from the contributing region, larger than the scanned spot. Increasing the energy to 5 keV increases the contributing volume, to hundreds of nanometres in depth and diameter in this case.

5.2 FIB/SEM

Several factors makes paper challenging to image with the electron microscope, which must necessarily be done without a conductive coating for FIB tomography. Paper is a composite of insulating materials and highly prone to charging. Furthermore, it consists of multiple phases and has a highly irregular and porous structure causing local variations in the E_2 neutrality point.

Taking FIB tomography as a whole, a wide range of settings and processes can be altered, from the sample preparation to the instrument settings and image processing. Because of this, the discussion is here divided into sections before the method as a whole is discussed.

Estimated Instrument Parameters

The calculated beam diameter, current and detector efficiency are rough estimates, performed in order to give a starting point for determining appropriate imaging parameters. The estimate of the DQE of the TLD is subject to several limitations. First, it is performed using Pt/Pd on epoxy, but the value for η used stems from a simulation of Pt/Pd on cellulose. This is because the precise composition of the epoxy is unknown, and it can not be simulated accurately as a result. However, the contributing volume is mostly within the metal layer (Figure 15), and the value of η is not far off from that of Pt/Pd alone (Table 4.1). More problematic is that intensity variation seemingly corresponding to surface topography is visible, which increases the intensity variation and thus lowers the estimated SNR. Furthermore, the same area is imaged multiple times, which can cause changes to the surface by beam damage or deposition of hydrocarbons. This can alter the intensity of the second image, thus giving a wrong brightness offset value.

The images in Figure 23, while noisy, do have clear topographical features. From the calculated SNR of 4, just above the Rose criterion, they should be just distinguishable from the noise. It is therefore likely that the SNR obtained is too low. Joy gives some typical DQE values for BSE detectors [1], ranging from 0.001 for an ETD to 0.3 for a dedicated BSE detector at 30 kV. The obtained value of 0.0018 is then at least in a reasonable range. That the TLD is on the lower end of this scale is probably correct, as it is known to have poor BSE collection efficiency [23]. The experiment is performed at 5 kV, and this can affect the detection efficiency obtained, as detectors may be less sensitive to low energy electrons [1]. The detection efficiency may therefore be lower for operation at 2 kV.

To determine the DQE more precisely, the brightness offset can be determined by acquiring an image with the beam blanked. The mean intensity of this image is then the offset accounting for the instrument brightness setting. Ideally, the experiment should be performed for flat surfaces of the pure phases to be studied, to account for any variation in detector efficiency due to the energy distribution of BSE varying with the material.

The minimum necessary beam current calculated in Table 4.7 depends on the DQE, and the calculation is therefore subject to the same sources of inaccuracy, thus overestimating the current needed. Note that the contrast used in this calculation is for unstained cellulose, and is therefore not comparable with the results using stained samples as these have higher material contrast.

The beam diameter as function of current (Table 4.8) is calculated without taking aberration effects into account. Thus, the largest aperture is used for the calculation, giving the largest possible divergence angle α . This also maximizes the aberrations, and so the real beam diameter is certainly bigger. A further source of inaccuracy is the unknown value of the FEG brightness, which is known to vary linearly with the acceleration voltage [53]. The calculated values do demonstrate the effect of increasing the beam current, and are comparable to the given maximum resolution of the instrument (1.2 nm).

Imaging Parameters

The objective in choosing imaging parameters is to achieve sufficient resolution to see the structure of the material, with sufficient contrast to separate the phases. Noise should be kept to a minimum for both reasons. Furthermore, the acquisition time should be kept as low as possible due to the number of images recorded in one tomography experiment.

With the working distance in the FIB fixed, the acceleration voltage V_0 , current I_B , dwell time τ and imaging mode (*i.e.* choice of detector and settings) remain to be adjusted. The choice of V_0 is the most fundamental, as it affects most aspects of the SEM. Note that immersion mode and the TLD was used for all experiments here as this was thought to eliminate shadowing due to the side-mounted position of the ETD while increasing resolution. However, the low BSE collection efficiency may make the ETD a better choice, though it may require milling wider side trenches to allow emitted electrons to escape.

Figures 24-27 show BSE and SE images taken for 2 and 5 kV at a range of currents with constant dwell time of 10 μ s. It is important to note that for this experiment, the brightness and contrast were manually altered between images by tuning the instrument brightness and contrast to fill the whole dynamic range, or as close as possible. This is therefore a subjective approach, but gives an impression of what contrast the chosen parameters are capable of. The aperture had to be manually realigned between each image, and focus and stigmators set. This introduces a further source of subjectivity in this comparison, and in particular influence the observed resolution.

Note also that these images show the same surface imaged multiple times, starting with low voltage and current. The current was then sequentially increased, before increasing the voltage and setting the current to low again. This repeated scanning may affect the surface. For one, charge may build up if not given time to dissipate between acquiring each image. In addition, the surface can be damaged by the electron beam, or contaminants may be deposited. This may in particular influence SE imaging where the contributing volume is confined to a region close to the surface, independently of acceleration voltage because the escape depth is independent of V_0 .

Charging artifacts can be observed in the 5 kV images for all currents above 21 pA, appearing as bright spots in GCC particles. 2 kV seems to be sufficiently low to avoid charging on flat surfaces, though small pores are seen to saturate in intensity, demonstrated in Figure 29b. This is likely a charging effect due to the geometry trapping emitted electrons.

The effect on the resolution of altering the voltage can not be judged entirely accurately from these comparisons due to the subjectivity in alignment and focusing. However, the resolution obtained is certainly better in the 2 kV case for BSE imaging. Increasing the voltage has two counteracting effects: reducing the beam diameter by decreasing optical aberration effects, but increasing

the size of the interaction volume. In these images 1024x943 pixel images with field of view 12.80 μm , each pixel corresponds to 12.5 nm^2 on the sample. The volume from which BSE can escape is seen from the simulations to be on this scale for 2 keV electrons. Increasing the voltage to 5 kV, the contributing volume corresponds to sampling an area dozens of pixels in radius. The increased penetration depth at 5 kV is immediately visible, the contours of features are seemingly smudged out (in particular the cellulose) and sub-surface features are visible.

In total, for this material the voltage should certainly be kept below 5 kV to avoid charging and reduce oversampling. It is possible that higher voltages than 2 kV may be used, however, and this may improve the image quality (and/or allow reduced acquisition time), in particular for BSE imaging due to the improved detector response at higher energies [1]. Determining the maximum acceptable voltage may therefore be worthwhile. On the other hand, there is a case to be made for choosing the lowest acceptable voltage for tomography. For one, charging may not be immediately visible as artifacts, but rather cause drift [32]. In addition, lower voltage will reduce the sampling depth, thus ensuring the images do not contain sub-surface information. This reduces overestimation of feature sizes and gives sharper boundaries between phases.

Increasing the beam current is seen to improve contrast and reduce noise. However, the resolution is lowered and charging effects are increased. The dwell time can be increased to compensate for lower current at the cost of longer acquisition time (Equation 2.5). For tomography, the total acquisition time becomes considerable, and it may be preferable to choose high current and low dwell time.

Comparing SE to BSE imaging, the SE images show markedly better resolution and much lower noise level. The increase in resolution is explained by the reduction in volume contributing as SE1 are emitted essentially only within the diameter of the beam. This is a further indication that the BSE resolution is limited by the material response, and significantly larger than the beam diameter. This is in agreement with the simulated extension of the interaction volumes. Though BSE resolution is expected to approach (or even exceed) SE resolution for low acceleration voltage [38], the low stopping power of the materials means that this point is not reached at 2 kV. The reduction in noise is explained by the high detector efficiency of the TLD for SE [23].

Charging artifacts are more dramatic for SE than BSE imaging at 5 kV, even at the lowest current settings. This is expected due to the low energy SE being more easily repelled by a surface charge. Though material contrast is usually not associated with SE imaging, good contrast can be seen between phases in the SE images at 2 kV, and weaker at 5 kV. SE material contrast at low acceleration voltage is a documented effect as mentioned in 2.2.4. Milling of cross sections in vacuum (minimizing deposition of contaminants on the surface), and the flat surfaces imaged (minimizing the intensity variation due to topography) likely contribute to enhancing the material contrast as compared to standard SEM.

There is variation in intensity within the cellulose phase that is not evident in

the BSE images. This is demonstrated in Figure 28. The variances in the histograms are comparable in the raw images, but after applying a median filter the BSE image shows much sharper peaks than the SE image. This indicates that the variance in the BSE image is due to shot noise (random variations) and can be decreased by median filtering, but that this is not the case for SE. One reason for this may be that compared to BSE, SE imaging will enhance any contrast caused by topography in the cross section, *e.g.* milling artifacts or pores. The larger sampling volume of BSE may also even out small contrast differences.

For this work, BSE imaging was used because it is known to be less sensitive to charging, and because the material contrast mechanism is reliable and well-known (monotonic with mean atomic number Z of the sample). However, the increase in resolution and reduction of acquisition time because of the detector efficiency may make SE imaging the superior choice, though the segmentation may become more challenging. BSE imaging with a more sensitive detector would reduce the necessary dwell time, but likely not improve the resolution as these results indicate the resolution to be limited by the sampling volume.

Sample Preparation

Embedding the samples in epoxy fixes the structure and prevents deformation/collapse as the material is milled. It also ensures that the acquired images are close to true cross sections, containing information from only one plane of the material. While methods have been suggested to segment FIB tomography data from porous media, *e.g.* by Salzer *et al.* [56], embedding simplifies the data processing. Furthermore, embedding protects the background structure (*e.g.* the inside wall of pores) from being damaged by the electron beam and avoids geometry-induced charging by filling voids, ensuring flat surfaces are imaged.

Epoxy embedding does, however, introduce a new problem. As the milled cross sections are smooth, topographical contrast is weak and it is necessary to rely on material contrast. As demonstrated in Figure 29, the contrast between cellulose and epoxy is not sufficient to distinguish the phases with the low voltage that is necessary to limit charging at this magnification, though higher current and longer dwell time will help as discussed above. Heavy metal staining of the material prior to epoxy embedding is found to be necessary to improve the contrast.

The increase in BSE material contrast from the positive uranyl acetate (UA)-staining used can be seen from the direct comparison images in figures 21 and 22, where two samples, identical in composition and preparation except for the staining are imaged with the same parameters. The material contrast is weakened for lower acceleration voltage, but still improved enough by staining to show the cellulose. Charging artifacts are apparent in the images of the unstained sample, but the significance of this is questionable. While it could indicate an increase in conductivity of the sample due to the staining, it could equally well be caused by random variations in the samples. These images are taken in the PFI-SEM at low magnification, and are therefore not directly comparable to images from the FIB. However, they do show that the staining procedure increases BSE material contrast significantly. Figure 21b shows that

fibers and large cellulose structures have higher intensity near their surfaces, and higher intensity near the surface of the paper. This is consistent with a positive stain penetrating into the structure from the surroundings.

Figure 29 shows FIB-SEM images from an unstained sample, where no cellulose is distinguishable. It is however likely that it is present, as there would otherwise be unsupported GCC particles. Furthermore, the overhead SIM images show faint structures present between particles. Figure 24b shows an image from a stained sample acquired with the same parameters, where cellulose is clearly visible. The staining protocol used is therefore taken to be successful, giving three clearly separable phases.

Two epoxy embedding methods were tried: 'cylinder' geometry (Figure 17a) and 'block' (Figure 17b). The former refers to embedding multiple paper samples held in a plastic clip in one cylindrical mold, a standard preparation method for SEM. For the latter, single paper samples are immersed in epoxy and impregnated, then sandwiched between glass slides before curing, giving a single paper sample embedded in an epoxy block. The sample height in the FIB is limited to around 5 mm, and the cylinder sample had to be cut down to size. For FIB tomography, a level and smooth sample surface is desirable as any surface topography can cause curtaining in milled cross sections.

The cylinder sample was polished by mechanical grinding with ethanol as lubricant. The block samples were polished by ion milling. The surfaces thus obtained are shown in figures 18 and 20. The ground sample showed cracking through the middle of paper samples. This may be due to the polishing, cutting of the cylinder, or caused during mounting of the sample. After cutting, the sample is a 5 mm thick disk of epoxy with paper samples running through the whole height. It is therefore likely fragile and easily cracked. On the surface, voids are seen around features of the sample. This may be caused by the use of ethanol during polishing, causing the polymers to swell and subsequently shrink. From the combination of cracks through the volume and rough surface, this preparation method was judged unsuitable for FIB tomography without improvements.

Block embedding the paper samples gives rectangular epoxy blocks, but must be mounted as cross sections to make the paper sample accessible. A smooth cross section must therefore be cut through the whole epoxy block. As can be seen from Figure 19, cutting the block with a scalpel gives a highly distorted surface. The epoxy seems to have fractured, and the fibers are torn rather than sliced cleanly. For this reason, the samples are polished by ion milling after cutting. Figure 20 shows the surface of ion milled samples. 20a is an overview of the whole epoxy block surface, taken at the edge of the ion milled area. In the ion mill, the sample is rotated in the beam. The center of the sample is therefore milled more than the edges, hence the uneven milling on the right side of the image. There are also unmilled areas near the top edge of the sample, likely due to insufficient milling time. Figure 20b shows a closeup of an ion milled sample surface, taken at 52° tilt. While quite smooth, some topography is visible, the GCC and pores seemingly causing a masking effect.

Smother surfaces can probably be achieved by optimizing the ion milling, *e.g.* by using lower acceleration voltage and longer milling time, but this is likely not crucial. Smooth surfaces on the scale relevant for FIB tomography can be found on the samples, and ion milling is time consuming. It is possible that sectioning with a microtome would give a sufficiently flat surface, and this could save some time in sample preparation. This was not tried as ion milling was found to work well, and mechanical sectioning was thought to be more likely to cause deformation of the sample.

The epoxy seems to have penetrated the structure, though large air bubbles are present as demonstrated in Figure 19a and voids around features are visible in 21a. In several samples, voids are seen in the lumen of fibers (figures 21a,20) and in pores in GCC clusters (Figure 29b). This is likely unavoidable, as these are enclosed voids that the epoxy can not penetrate into. Despite these flaws, the tomograms show that regions of the samples are well-embedded with few flaws.

The epoxy block is coated with Pt/Pd to avoid or minimize charging. Obscuring the surface topography is no concern for FIB tomography (in contrast to conventional SEM), so a thick coating can be used to ensure good electrical contact. Furthermore, tomography necessarily involves repeated imaging around the ROI with the ion beam, potentially at milling current, which will erode the surrounding surface coating. However, being able to discern the paper sample through the coating helps with finding an area of interest. Figure 20b shows the paper clearly through a 5 nm Pt/Pd coating, while it is barely visible in 20a with 20 nm coating. This is therefore taken as a decent compromise thickness, though it is possible that an even thicker coating can help reduce charging effects.

Milling

The objective in selecting milling parameters is to obtain smooth cross sections milled to a sufficient depth. The milling current and total ion dose (number of incident ions per area) are main milling parameters to vary. The milling rate of the material is linear with the current, and therefore determines the milling time. The ion dose determines the depth of milling. Here, a nominal milling depth (calibrated for silicon) is also used for ease of repeatability with this instrument. High ion beam current and too low dose is known to increase the formation of milling artifacts [44, 18].

Here, milling currents from 0.093 to 0.46 nA have been used for slice milling. Vertical streaks are apparent for the whole range of currents (*e.g.* figures 29a, 31c and 35b), especially noticeable in the lower areas of the images. Experiment ASV2, performed at 0.28 nA, shows high intensity vertical artifacts (figures 31a and 31b). These are erroneously identified as cellulose in the segmentation, and can be seen in the reconstructed volume (Figure 32). Figure 33a shows heavy curtaining as a result of a rough cut milled at 6.5 nA ion beam current. Significant curtaining is seen in ASV5, Figure 39. Vertical rows of pores are visible in the cellulose phase, likely a fiber wall. This may partly be because of the

internal structure of the fiber, but the vertical orientation suggests a connection to the ion milling. This experiment used the lowest ion dose, and the milling may simply have been insufficient. If this is the case, the artifacts seen are simply milling in progress in the field of view. The effect is most visible near the bottom of the images, and may perhaps be caused by ions impacting the surface at an angle, as FIB milling is known to create angled surfaces [22].

For experiments ASV3,4,5 and 6, a 500 nm pad of Pt was deposited by the ion beam on the surface of the block to be imaged. An example is shown in Figure 34a. This is recommended in the literature to reduce milling artifacts, but artifacts are still observed, as in Figure 39. The cleanest cross sections were obtained at 93 pA with a deposited platinum pad in experiment ASV4. However, the same gave the most dramatic artifacts seen in experiment ASV5. In addition to the difference in dose, a reason for the difference may be seen by comparing figures 34a and 39a. The surface of the sample below the pad is rougher in the latter. This roughness gives areas where the platinum pad is thicker, and this may cause masking during the milling. The surface roughness may be ion beam damage caused during preparation of the area.

These results do indicate that increasing the ion dose gives smoother cross sections, and is perhaps more important than the beam current by itself, at least when set too low, as this may give insufficient milling depth. A range of doses and currents could be tried to confirm this. If higher currents can be used, it may be possible to increase the dose while reducing the milling time.

For experiments ASV2-6, the image resolution is 1024x884 pixels with 12.80 μm horizontal field of view. Corrected for the 52° tilt of the surface, this gives a height (y) of 14.02 μm for the volume imaged. If it is the ion dose that is the limiting factor for smooth milling, a dose of approximately 7.5 nC μm^{-2} is suggested as a minimum for milling of relatively smooth cross sections to this depth in the material.

Area Preparation and Set-Up

The set-up times of the tomography experiments were considerable, taking up to eight hours. As total experiment time is a limiting factor in practice, this reduces the number of slices imaged. Some practical issues with the set-up are therefore discussed here, with suggestions for reducing the set-up time.

For all the tomography experiments, a U-shaped trench was milled around the area of interest. This is done to allow emitted electrons to escape and thus avoid shadowing in the obtained images. However, experiments ASV5 and 6 show intensity variation along the y-direction, as do the images in figures 24-27, the bottom of the images appearing darker. This is likely caused by insufficient milling in the front trench. Figures 36a and 36b indicate that there is a wall-like structure in the front trench, which may cause shadowing. Such a structure may have been formed (or enlarged) by redeposition of material from polishing of the block face. In Figure 39, a foreground structure can be seen in images 39c-39f. While it is not evident in the first image, it comes into view because of drift. Increasing the area and depth of the milled trench may help with this,

and image processing can to a degree correct for shadowing effects.

A quirk of the FIB software used is that the position of the fiducial mark is set automatically in relation to the area chosen for milling, and can not be altered, though it can be placed on the left or right side of the area. For experiments ASV1, 2, 3 and 4, the trenches were milled before starting the S&V software, and the fiducial was then inadvertently placed on edges or at the bottom of milled trenches. For experiment 4, two fiducials were milled as the first was not recognized by the software. As can be seen from Figure 33d, this experiment failed due to misalignment of the slices. The two fiducial marks, interrupted by trench edges, may be the cause of this. For the further experiments, only the front trench was milled before starting the S&V program, and the fiducial marks were milled before the side trenches. In cases where the software failed to identify the fiducial mark, the fiducial mark was milled away. The procedure was then restarted, and a new fiducial mark made. The evidence of this can be seen in Figure 36.

The milling of the front face of the block is shown for ASV4 and 6 (figures 34 and 40). As the milling progresses further into the block, the rough cut face is seen to be milled from the bottom up. The milling pattern removes sequential xy -planes, so this indicates that the block face is tilted away. This increases the set-up time considerably, as the electron beam can not be focused accurately until the whole block face is being milled. FIB milling is known to give angled walls for two reasons: redeposition and milling by the beam tail [37, 22]. The latter can be observed in Figure 40 as milling along the top of the block. Redeposition is not likely to be the cause of the angled face, as the rough cut is made with a cleaning cross section milling pattern, and sputtered material should be ejected away from the face. The visible structure in the uncovered areas in figures 34 and 40 shows that this is not redeposited material.

To reduce the effect, a multi-step polishing process of the block face is suggested here, illustrated in Figure 41. The first cut (A) is the milling of the front trench, which can be done at very high ion beam current, and with a high dose giving a deep trench. Then, a thin rectangle (B) is milled into the block face with lower current. This should overlap with the previous cut to ensure sufficient milling on the face. The final polishing cut (C) can be performed as the automatically aligned rough cut in the S&V software, using a low current and overlapping the previous cut. This final polishing cut should be perfectly aligned with the final block face (D) by the software. Altering the ion beam current may alter the beam alignment, and for each milling step a SIM image should be captured using the milling current to position the milling area correctly. These images can be reduced area scans of the area periphery to avoid deterioration of the metal coating near the block by high-current imaging.

Image Processing

The automated image processing used was successfully able to segment image stacks and reconstruct the volume. Visual inspection and comparison to the SEM images indicate this was decent, but not perfect. Milling artifacts are

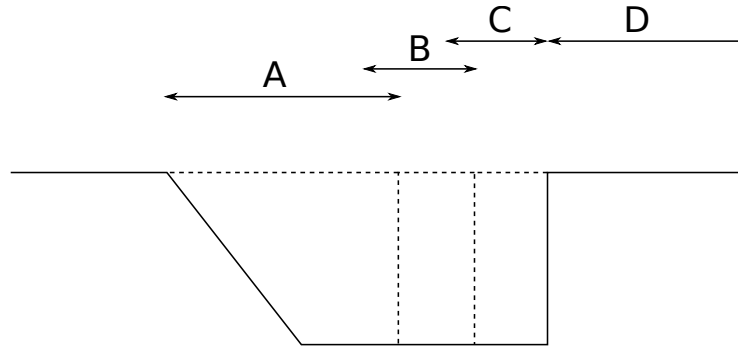


Figure 41: Suggested procedure for polishing block face, yz section. Arrows indicate the extent of milling steps. A is the initial front trench milled at high current. B is a cut with lower current, overlapping with A. C is the rough cut made by the S&V software, with current close to the final milling current. It should be automatically aligned to the final block face, indicated by region D.

seen to be identified as cellulose, and boundary regions of filler particles, with intensity in the same intermediate range as cellulose, are in places taken to be patches of cellulose. Cellulose features near the resolution limit are misidentified as epoxy.

Note that the choice of segmentation thresholds is here subjective. The thresholding introduces a significant possibility of errors, as the choice of threshold will determine how boundary regions between phases are classified, *i.e.* where to place the boundaries of features. When this is repeated for a stack hundreds of images, small errors can be magnified. For this reason, the limited volumes reconstructed are likely not well suited to precise quantitative analysis.

One of the reasons for the low precision is that the boundaries between features are not sharply defined, and small cellulose features (in particular) are difficult to separate from the background. They may be of similar size and intensity value as the boundary regions around GCC particles or milling artifacts, and therefore easily misidentified. The size of the BSE sampling volume may be one of the main reasons for these blurred boundaries and unclear small features. SE imaging should help giving better feature definition in the images, though perhaps at the cost of more variation within phases.

With SEM images from flat surfaces with clearly defined features, sharp borders and little variation in intensity within features, a more sophisticated segmentation routine based on edge-finding may be well suited. If borders around regions are established, the regions can be classified by their mean intensity into the three phases.

The flat field correction routine used here is a further source of subjectivity in the processing, as it uses a composed background image. This was done because of the difficulty of obtaining a pure background image (which would require milling an identical trench - with the same artifacts - in an area of only

epoxy). However, the routine did allow thresholding, which was not possible in the raw image as the intensity of the background phase overlapped with that of the cellulose phase.

FIB Tomography

One of the main problems encountered with FIB tomography in practice was drift. For the SEM imaging, this causes the area of interest to disappear out of the field of view, as can be seen in experiments ASV4, 5 and 6 (figures 33, 35 and 39) as the block edges coming into view. Post acquisition image alignment corrects for this, but means that the image stack is cropped. The already limited volume analyzed is therefore further reduced.

Note that apparent drift in the y -direction of the images can be caused by the sample not being mounted level, but tilted toward the rear. If the sample surface is not normal to the ion beam, this can cause part of the area tracked to lie outside the sample. This should not cause drift in the x -direction, however.

The origin of this drift can be mechanical or electrostatic in origin [32]. The samples were mounted with carbon tape, which is elastic. If stretched during application, this may cause the sample to move if not given time to settle. It is also possible that the tape is affected by the chamber vacuum or beam radiation. While carbon tape is commonly used for SEM samples without issue, the long acquisition time of FIB tomography means the technique is more sensitive to drift.

If electrostatic, the drift may be caused by charging of the sample surface. Though the sample surface is coated with metal, the uncoated cross section is subject to charging, as demonstrated by figures 25 and 27. The surface coating is removed in large areas by the milling, and eroded by the repeated SIM imaging at milling current. Figure 34b shows an overview of the area after tomography, where the dark rectangles on the surface are fields that have been scanned repeatedly by the ion beam. In their 2012 review of FIB tomography, Holzer and Cantoni specifically mention drift caused by charging as one of the main challenges to overcome for FIB tomography of insulating samples [32].

Drift also affects the ion beam, as can be seen from the position of the area changing in the SIM alignment images. Drift of the ion beam can cause the milling to be misaligned with the face of the block. The software used corrects for this by milling a reference mark and finding its position in drift correction SIM images taken before milling each slice. However, drift can bring the reference mark out of the ion field of view, as was the case in experiment ASV6. The automated procedure then fails.

A central obstacle for FIB tomography is finding an acceptable compromise between acquisition time, image quality and the volume analyzed. As can be seen from Table 4.9, the acquisition times can become considerable if larger volumes are to be analyzed. The acquisition rate (pixels recorded per second) can be used as a measure of the efficiency of the technique, and the effect of altering parameters on this rate can be estimated.

For each slice of the tomography procedure, an ion beam image is captured, a slice is milled, immersion mode is turned on, an electron beam image is captured and immersion mode is turned off again. The acquisition time for a complete tomography procedure of an area xz with image resolution $x_e y_e$ pixels and n slices can then be approximated as:

$$(x_e y_e \tau_e + t_{imm})n + x_i y_i \tau_i n + \frac{xzD}{I_{ion}}.$$

The first term is the total SEM imaging time, with $x_e y_e$ the electron image resolution in pixels and τ_e the electron beam dwell time. t_{imm} is the time to turn on and off the immersion lens (approximately 15 s) if used. The second term is the SIM imaging time, with corresponding variables for the ion beam. The third term is the total milling time with xz the area to be milled, D the ion dose and I_{ion} the ion beam current. The acquisition rate is then the total number of pixels $x_e y_e n$ divided by the total time. Assuming the time for ion beam imaging and turning on and off the immersion lens are negligible compared to milling and electron beam imaging, the rate (pixels per time) is approximately:

$$\frac{1}{\tau + \frac{xz\Delta z}{I_{ion}x_e y_e}},$$

with $\Delta z = z/n$ the slice thickness. This sums up the effect of altering the imaging and milling parameters. Note that drift in the xy -plane will effectively lower the rate because of cropping of the image stack.

In brief there is likely no optimal set of parameters, but a compromise must be found for each use case between the desired volume, resolution and the milling and imaging qualities. The effect of altering any parameter can be quantified by time and rate calculations as suggested above. It is almost certain that better compromises can be made than those found here. In particular, the use of SE imaging is promising due to the lower dwell time necessary. The results also indicate that the ion beam current can be increased somewhat without drastically reducing the milling quality.

A significant drawback of FIB tomography is that, because of the limited volume analyzed, it is uncertain whether the tomogram will contain features of interest. The volume to be imaged is defined from the sample surface, and what will be uncovered is not known beforehand. Furthermore, the method is destructive, not only to the volume analyzed, but to the surrounding area as well.

While FIB offers higher z -resolution, SBFSEM seems a comparable alternative technique. In principle, the xy -resolution possible is the same, as it is limited by the SEM for both methods. SBFSEM has a great advantage in that the time taken to cut each slice is independent of the slice thickness. The total acquisition time will then not scale with the volume, only the number of slices, *i.e.* the z -resolution. The method can then allow characterization on a much larger range of scales. Slice thickness of 200 nm is used for paper by Zankel, *et al.* [66], and down to 30 nm has been demonstrated for other materials. Furthermore, the literature mentions SBFSEM as more easily and quickly performed

in practice than FIB tomography.

The development of ptychographic X-ray tomography with comparable resolution to SEM methods (16 nm resolution has been achieved) may make the latter obsolete, in particular due to the large volumes that can practically be imaged. Furthermore, samples can be imaged with simple preparation and can be studied in atmosphere [17]. However, the method does require a synchrotron source. A potential advantage for SEM-based methods is multispectral imaging, as multiple types of detectors can be used. With both an electron and an ion beam available, SIMS and EDS/EDX can for instance be used for elemental mapping during tomography (though the resolution may more limited than the imaging resolution) [32].

Paper has structural features ranging from nanometres to hundreds of micrometres, and a compromise must be made between volume and resolution because of the practical limit imposed by the total acquisition time. For characterization on the scale of fibers, FIB will likely be inefficient, at least when compared to X-ray tomography, and probably also to mechanical sectioning SEM methods. FIB tomography can, however, fill a niche between high resolution, low volume TEM and the high volume, low resolution methods.

With resolution limit in the nanometre range, FIB tomography should be well suited to study CNF in paper materials, and can directly show how CNF, filler particles and fibers are interconnected in three dimensions. With the emphasis on developing the method, the volumes analyzed here are insufficient to answer these questions, though they do show that visualization of interconnected filler particles, fibers and nanoscale cellulose structures is possible.

Use of the method for studying the distribution of CNF in the whole sheet would likely require large analysis volumes to give representative results. With sufficient resolution to see CNF directly, this may be impracticable. Taking thicker z -slices (*e.g.* hundreds of nanometres), the method could however be used to obtain a series of interspersed cross sectional images with high xy -resolution from which the CNF distribution could be estimated.

6

Conclusion

The results obtained demonstrate that FIB tomography is possible as a characterization method for paper materials. Resolution of $13 \times 13 \times 15 \text{ nm}^3$ is achieved here, and this can likely be improved to the nanometre range. The volumes analyzed are around $10 \times 10 \times 2 \text{ }\mu\text{m}^3$, but this is limited by the acquisition time and thus extensible.

Paper materials pose several challenges to analysis by electron and ion beams. It is a composite of insulating phases, vulnerable to charging and beam damage. This severely limits the range of parameters that can be used, in particular for imaging. To analyze the material, epoxy embedding is necessary, but this in turn makes heavy metal staining necessary for contrast. Positive staining with uranyl acetate is demonstrated to give sufficient contrast to separate the phases.

Low voltage BSE imaging is used successfully, giving decent resolution and contrast, but the low efficiency of the detector used means that the imaging time is long and the images noisy. Even with the low voltages used, simulations show that the interaction volume is of considerable size and limits the BSE resolution. Use of SE imaging is suggested for better resolution and lower acquisition time, though the material contrast may be more confused.

FIB tomography of paper materials is shown to be *possible*, but whether it is *useful* is a question of what information can be gained from 3D microscopy on the nanoscale. Visualization of the structure in three dimensions is an obvious first step, and easily achieved when a segmented image stack is available, which is anyway a prerequisite for further analysis.

Visualization by FIB tomography can help determine how CNF is distributed and how it interacts with the other paper components. FIB tomography is a well suited characterization method for this purpose, giving the high resolution necessary for resolving CNF combined with the potential to image sufficient volumes. However, the results obtained here are insufficient to conclude in these areas, and larger volumes and more experiments are necessary to have a representative sampling. In particular, tomograms of control samples with no CNF added are important to have results of any significance. The main obstacle to use of the method for this purpose is balancing the necessary resolution and volume, as well as finding relevant regions in the sample.

In addition to visualization, quantitative methods can be applied to a reconstructed 3D volume, *e.g.* to measure porosity or quantify the clustering of filler particles. FIB tomography may be well suited to studies of coatings and inks on paper, as the region of interest is inherently limited to a smaller volume. Single beam FIB has already been used for this purpose [10, 42, 26], though with lower z -resolution than is possible with a dual-beam instrument.

The dual-beam FIB is well suited for milling cross sections, and this does not need to be automated, closely spaced slices as in tomography. The FIB can be used more generally for *in situ* sample preparation and imaging. The combined instrument can be used for all the same purposes and use cases as SEM, with the ion beam quite literally opening a new dimension for imaging.

6.1 Further Work

Optimization of the instrument parameters for the material is worthwhile in order to maximize the volumes that can be analyzed. Because of the low efficiency of the detector used for BSE, using SE imaging is an obvious first step to lowering the acquisition time, while improving the xy resolution.

Milling parameters can be optimized by testing milling with a range of currents and doses. The maximum current and minimum dose that gives acceptable cross sections of the desired depth will minimize the milling time. Due to the inhomogeneity of the material, this could be done for the pure phases separately. Taking the parameters for the slowest-milling phase as the worst-case parameters for the material as a whole can improve the reliability of the milling.

Reducing drift is also of importance, both to maximize the volume analyzed and to increase the reliability of the method. A first step is ascertaining whether the observed drift is actual mechanical movement of the sample, or caused by charging. For the first, a more stable sample mounting can be used, *e.g.* clamping the sample to the stub. Whether the problem is electrostatic in origin can be investigated by definitely grounding the sample, for instance by touching it with a microprobe introduced into the microscope or by deposition of a Pt wire to a grounded contact.

Image processing is a field of its own, and more sophisticated segmentation and analysis is of interest to improve the segmentation and obtain quantitative data. The use of 3D image processing routines is a possibility not investigated here that could help in this regard.

CNF distribution may perhaps be studied by marking the fibril fraction with some substance recognizable in microscopy before it is added to the furnish. This would allow identification and mapping of the CNF fraction alone. For SEM, this could be a heavy metal stain increasing the mean atomic number, though it would have to be chosen with care to give sufficient contrast to the other phases. Use of other detectors opens other possibilities in this direction. For instance, SIMS and EDS/EDX can be used with FIB for elemental map-

ping in 3D, and fibrils could then be marked with some distinguishable element. Whatever the method, selective marking of the CNF fraction would require the marker to survive the paper making process, without altering the structure of the resulting material too much.

Abbreviations

BNC bacterial nanocellulose.

BSE backscattered electron.

CNC cellulose nanocrystal.

CNF cellulose nanofibrils.

DQE detector quantum efficiency.

EDS/EDX energy-dispersive X-ray spectroscopy.

ESEM environmental scanning electron microscope.

ETD Everhart-Thornley detector.

FEG field emission gun.

FIB focused ion beam.

GAE gas assisted etching.

GCC ground calcium carbonate.

LMIS liquid metal ion source.

LVSEM low-voltage scanning electron microscope.

MFC microfibrillated cellulose.

NFC nanofibrillated cellulose.

PE primary electron.

SBFSEM serial block face scanning electron microscopy.

SE secondary electron.

SEM scanning electron microscope.

SI secondary ion.

SIM scanning ion microscope.

SIMS secondary ion mass spectrometry.

SNR signal-to-noise ratio.

SSSEM serial section scanning electron microscopy.

SSTEM serial section transmission electron microscopy.

TEM transmission electron microscope.

TLD through-lens detector.

UA uranyl acetate.

WD working distance.

Symbols

C_c Coefficient of chromatic aberration.

C_s Coefficient of spherical aberration.

d Probe diameter.

D Ion dose.

e Electron charge.

E_0 Kinetic energy of incident electron.

I_B Beam current.

V_0 Acceleration voltage.

Z Atomic number.

α Beam convergence angle.

β Source brightness.

τ Dwell time.

δ Secondary electron yield.

ΔE Energy spread.

η Backscattering coefficient.

λ Wavelength.

Figures

1	Molecular structure of glucose and cellulose.	5
2	Schematic illustration of SEM	8
3	Electron source cathode-vacuum junction	10
4	Beam path in the SEM	12
5	SE yield as function of E_0	15
6	Emitted electron energy spectrum	17
7	Interaction volume	18
8	Everhart-Thornley detector	19
9	Topographic contrast	21
10	Currents into and out of the sample	23
11	Sputter yield of the elements.	27
12	Coordinate system	28
13	Simulated interaction volume, 0° tilt	42
14	Simulation distributions	43
15	Simulated interaction volume, Pt/Pd on cellulose	44
16	Simulated interaction volume, 52° tilt	45
17	Epoxy embedded samples	46
18	Ground epoxy block	47
19	Epoxy block cut with scalpel	47
20	Ion milled epoxy block	48
21	SEM of stained and unstained samples	49
22	SEM of stained and unstained samples	49
23	Images for estimation of DQE	51
24	BSE parameter variation, 2kV	52
25	BSE parameter variation, 5kV	53
26	SE parameter variation, 2kV	54
27	SE parameter variation, 5kV	55
28	Variance in material contrast, SE/BSE	56
29	ASV1	58
30	ASV1 processed	59
31	ASV2	60
32	ASV2 processed	61
33	ASV3	62
34	ASV4	63
35	ASV4	64
36	ASV4	65
37	Background levelling	65

38	ASV4 reconstruction	66
39	ASV5	67
40	ASV6	68
41	Suggested block face polishing	78

Bibliography

- [1] D. C. Bell and N. Erdman. *Low Voltage Electron Microscopy: Principles and Applications*. John Wiley & Sons, 2013.
- [2] C. J. Biermann. *Handbook of Pulping and Papermaking (2nd Edition)*. Academic Press, 1996.
- [3] A. Birch-Andersen. “Reconstruction of the Nuclear Sites of *Salmonella typhimurium* from Electron Micrographs of Serial Sections”. In: *J. Gen. Microbiol.* 13 (1955), pp. 327–329.
- [4] M.J.F. Blumer et al. “Ribbons of semithin sections: an advanced method with a new type of diamond knife”. In: *Journal of Neuroscience Methods* 120 (2002), pp. 11–16.
- [5] F.W. Brodin, Ø. W. Gregersen, and K. Syverud. “Cellulose nanofibrils: Challenges and possibilities as a paper additive or coating material – A review”. In: *Nordic Pulp & Paper Research Journal* 29 (1 2014).
- [6] M. R. JR Brown. “Cellulose Structure and Biosynthesis: What is in Store for the 21st Century?” In: *Journal of Polymer Science: Part A: Polymer Chemistry* 42 (2004), pp. 487–495.
- [7] H. N. Chapman and K.A. Nugent. “Coherent lensless X-ray imaging”. In: *Nature Photonics* 30 (2010), pp. 833–839.
- [8] G. Chinga, P.O. Johnsen, and O. Diserud. “Controlled serial grinding for high-resolution three-dimensional reconstruction”. In: *Journal of Microscopy* 214 (2003), pp. 13–21.
- [9] G. Chinga-Carrasco. “Cellulose fibres, nanofibrils and microfibrils: The morphological sequence of MFC components from a plant physiology and fibre technology point of view”. In: *Nanoscale Research Letters* 6 (2011).
- [10] G. Chinga-Carrasco. “Exploring the multi-scale structure of printing paper - a review of modern technology”. In: *Journal of Microscopy* 234 (2009), pp. 211–242.
- [11] M. De Winter et al. “Tomography of insulating biological and geological materials using focused ion beam (FIB) sectioning and low-kV BSE imaging”. In: *Journal of Microscopy* 233 (2009), pp. 372–383.
- [12] H. Demers et al. “Three-Dimensional Electron Microscopy Simulation with the CASINO Monte Carlo Software”. In: *Scanning* 33 (3 2011), pp. 135–146.
- [13] W. Denk and H. Horstmann. “Serial Block-Face Scanning Electron Microscopy to Reconstruct Three-Dimensional Tissue Nanostructure”. In: *PLoS Biol* 2 (11 2004), e329.

- [14] B. Domenges and K. Charlet. “Direct Insights on Flax Fiber Structure by Focused Ion Beam Microscopy”. In: *Microscopy and Microanalysis* 16 (2010), pp. 175–182.
- [15] D. Drouin et al. “CASINO V2.42 - A Fast and Easy-to-use Modelling Tool for Scanning Electron Microscopy and Microanalysis Users”. In: *Scanning* 29 (2007), pp. 92–101.
- [16] R. F. Egerton. *Physical Principles of Electron Microscopy*. Springer, 2005.
- [17] M. Esmaeili et al. “Ptychographic X-ray Tomography of Silk Fiber Hydration”. In: *Macromolecules* 46 (2013), pp. 434–439.
- [18] A. Friedmann et al. “FIB section of cell-electrode interface: An approach for reducing curtaining effects”. In: *Microelectronic Engineering* 124 (2014), pp. 17–21.
- [19] A. Friedmann et al. “Investigation of cell-substrate interactions by focused ion beam preparation and scanning electron microscopy”. In: *Acta Biomaterialia* 7 (2011), pp. 2499–2507.
- [20] L. Fukuhara et al. “FIB processing for natural rubber with nanomatrix structure”. In: *Polymer* 57 (2015), pp. 143–149.
- [21] L. A. Giannuzzi and F. A. Stevie, eds. *Introduction to Focused Ion Beam Systems*. Springer, 2005.
- [22] L. A. Gianuzzi, B. I. Prentzer, and B. W. Kempshall. “Ion-solid interactions”. In: *Introduction to Focused Ion Beam Systems*. Ed. by L. A. Giannuzzi and F. A. Stevie. Springer, 2005.
- [23] I. J. Goldstein et al. *Scanning Electron Microscopy and X-Ray Microanalysis*. Springer, 2003.
- [24] K.M. Harris et al. “Uniform Serial Sectioning for Transmission Electron Microscopy”. In: *The Journal of Neuroscience* 26 (47 2006), pp. 12101–12103.
- [25] M. He, B. Cho, and M.J. Won. “Effect of precipitated calcium carbonate - Cellulose nanofibrils composite on paper properties”. In: *Carbohydrate Polymers* 136 (2016), pp. 820–825.
- [26] P.J. Heard et al. “Visualisation of the distribution of ink components in printed coated paper using focused ion beam techniques”. In: *Colloids and Surfaces A. Physicochem. Eng. Aspects* 244 (2004), pp. 67–71.
- [27] C. Hii et al. “The effect of MFC on the pressability and paper properties of TMP and GCC based sheets”. In: *Nordic Pulp & Paper Research Journal* 27 (2 2012), pp. 388–396.
- [28] J. Hjelen. *Scanning elektron-mikroskopi*. SINTEF, 1986.
- [29] B. Holdford. “The uses of dual beam FIB in microelectronic failure analysis”. In: *Introduction to Focused Ion Beam Systems*. Ed. by L. A. Giannuzzi and F. A. Stevie. Springer, 2005.
- [30] M. Holler et al. “X-ray ptychographic computed tomography at 16 nm isotropic 3D resolution”. In: *Scientific Reports* 4 (2014).
- [31] R. Holmstad et al. “Quantification of the three-dimensional paper structure: Methods and potential”. In: *Pulp Paper Canada* 104 (2003), pp. 47–49.

- [32] L. Holzer and M. Cantoni. “Review of FIB tomography”. In: *Nanofabrication Using Focused Ion and Electron Beams*. Ed. by Utke I., S. Moshkalev, and Russell P. Oxford University Press, 2012.
- [33] L. Holzer et al. “Three-dimensional analysis of porous BaTiO₃ ceramics using FIB nanotomography”. In: *Journal of Microscopy* 216 (2004), pp. 84–95.
- [34] L. Hughes et al. “Serial block face scanning electron microscopy - the future of cell ultrastructure imaging”. In: *Protoplasma* 251 (2014), pp. 395–401.
- [35] N. Imanishi. “Interactions of ions with matter”. In: *Focused Ion Beam Systems: Basics and Applications*. Ed. by N. Yao. Cambridge University Press, 2007.
- [36] B.J. Inkson, Mulvihill M., and G. Möbus. “3D determination of grain shape in a FeAl-based nanocomposite by 3D FIB tomography”. In: *Scripta materialia* 45 (2001), pp. 753–758.
- [37] T. Ishitani et al. “Improvements in performance of focused ion beam cross-sectioning: aspects of ion-sample interaction”. In: *Journal of Electron Microscopy* 53.5 (2004), pp. 443–449.
- [38] D. C. Joy and C. S. Joy. “Low Voltage Scanning Electron Microscopy”. In: *Micron* 27 (3-4 1996), pp. 247–263.
- [39] D.C. Joy. *Monte Carlo Modeling for Electron Microscopy and Microanalysis*. Oxford University Press, 1995.
- [40] D. Klemm et al. “Cellulose : Fascinating Biopolymer and Sustainable Raw Material”. In: *Angew. Chem . Int. Ed.* 44 (2005), pp. 3358–3393.
- [41] D. Klemm et al. “Nanocelluloses: A New Family of Nature-Based Materials”. In: *Angew. Chem . Int. Ed.* 50 (2011), pp. 5438–5466.
- [42] H. Koivula et al. “Visualisation of the distribution of offset ink components printed onto coated paper”. In: *Colloids and Surfaces A. Physicochem. Eng. Aspects* 317 (2008), pp. 557–567.
- [43] M.H.J. Korhonen and J. Laine. “Flocculation and retention of fillers with nanocelluloses”. In: *Nordic Pulp & Paper Research Journal* 29 (1 2014), pp. 119–128.
- [44] R. Langford. “Preparation for physico-chemical analysis”. In: *Focused Ion Beam Systems: Basics and Applications*. Ed. by N. Yao. Cambridge University Press, 2007.
- [45] N. Lavoine et al. “Microfibrillated cellulose - Its barrier properties and applications in cellulosic materials: A review”. In: *Carbohydrate Polymers* 90 (2012), pp. 735–764.
- [46] H. Meier. “Chemical and morphological aspects of the fine structure of wood”. In: *Pure and Applied Chemistry* 5 (1962), pp. 37–52.
- [47] R. J. Moon et al. “Cellulose nanomaterials review: structure, properties and nanocomposites”. In: *Chem. Soc. Rev.* 40 (2011), pp. 3941–3994.
- [48] K. Ohya and T. Ishitani. “Imaging using electrons and ion beams”. In: *Focused Ion Beam Systems: Basics and Applications*. Ed. by N. Yao. Cambridge University Press, 2007.

- [49] V. Ottesen, K. Syverud, and Ø.W. Gregersen. “Mixing of Cellulose Nanofibrils and Individual Furnish Components: Effects on Paper Properties and Structure”. In: *Nordic Pulp & Paper Research Journal* 31 (3 2016 in press).
- [50] D. Perovic et al. “Field-emission SEM imaging of compositional and doping layer semiconductor superlattices”. In: *Ultramicroscopy* 58 (1995), pp. 104–113.
- [51] M.W. Phaneuf. “FIB For Materials Science Applications - A Review”. In: *Introduction to Focused Ion Beam Systems*. Ed. by L. A. Giannuzzi and F. A. Stevie. Springer, 2005.
- [52] R. Phelan, J.D. Holmes, and N. Petkov. “Application of serial sectioning FIB/SEM tomography in the comprehensive analysis of arrays of metal nanotubes”. In: *Journal of Microscopy* 246 (2011), pp. 33–42.
- [53] L. Reimer. *Image Formation in Low-Voltage Scanning Electron Microscop.* SPIE - The International Society for Optical Engineering, 1993.
- [54] J.M. Rodenburg et al. “Hard-X-Ray Lensless Imaging of Extended Objects”. In: *Physical Review Letters* 98 (2007), pp. 50–53.
- [55] J.C. Russ and F.B. Neal. *The Image Processing Handbook*. 7th ed. CRC Press, 2015.
- [56] M. Salzer et al. “On the importance of FIB-SEM specific segmentation algorithms for porous media”. In: *Materials Characterization* 95 (2014), pp. 36–43.
- [57] E.J. Samuelsen et al. “Three-dimensional imaging of paper by use of synchrotron x-ray microtomography”. In: *Journal of Pulp and Paper Science* 27 (2 2001), pp. 50–53.
- [58] J. Schindelin, I. Arganda-Carreras, and E. Frise. “Fiji: an open-source platform for biological-image analysis”. In: *Nature methods* 9 (7 2012), pp. 676–682.
- [59] C.A. Schneider, W.S. Rasband, and K.W. Eliceiri. “NIH Image to ImageJ: 25 years of image analysis”. In: *Nature methods* 9 (7 2012), pp. 671–675.
- [60] E. Schroeder-Reiter et al. “Focused ion beam (FIB) combined with high resolution scanning electron microscopy: A promising tool for 3D analysis of chromosome architecture”. In: *Journal of Structural Biology* 165 (2009), pp. 97–106.
- [61] John M. Sosa et al. “Development and application of MIPARTM: a novel software package for two- and three-dimensional microstructural characterization”. In: *Integrating Materials and Manufacturing Innovation* 3.1 (2014), pp. 1–18.
- [62] F.A. Stevie, L.A. Giannuzzi, and B.I. Prenitzer. “The Focused Ion Beam Instrument”. In: *Introduction to Focused Ion Beam Systems*. Ed. by L. A. Giannuzzi and F. A. Stevie. Springer, 2005.
- [63] G. Sundaramoorthi et al. “3D Membrane Imaging and Porosity Visualization”. In: *Ind. Eng. Chem. Res.* 55 (2016), pp. 3689–3695.
- [64] A.F. Turbak, F.W. Snyder, and K.R. Sandberg. “Microfibrillated cellulose, a new cellulose product: properties, uses, and commercial potential”. In: *Journal of Applied Polymer Science: Applied Polymer Symposium* 37 (1983), pp. 815–827.

- [65] N. Yao. “Introduction to the focused ion beam system”. In: *Focused Ion Beam Systems: Basics and Applications*. Ed. by N. Yao. Cambridge University Press, 2007.
- [66] A. Zankel et al. “Ultramicrotomy in the ESEM, a versatile method for materials and life sciences”. In: *Journal of Microscopy* 233 (2008), pp. 140–148.